TÉCNICO LISBOA

Design and Construction of a Scanning Ion Conductance Microscope (SICM)

Samuel Mendes Leitão

Dissertation to obtain the Master degree in
Bioengineering and Nanosystems

Jury

Chairperson: Prof. Luís Joaquim Pina da Fonseca

Internal Supervisor: Dr. Carla da Conceição Caramujo Rocha de Carvalho

External Supervisor: Prof. Georg E. Fantner

Members of the committee: Prof. Telmo Jorge Gomes dos Santos

November 23, 2015

Acknowledgements

I wish to express my sincere gratitude to Prof. Georg E. Fantner for receiving me at the Laboratory of Bio- and Nano-Intrumentation (LBNI), in École Polytechnique Fédérale de Lausanne (EPFL). I am also very grateful to Adrian Nievergelt for his help and inputs during the whole project.

To all the members at LBNI, thank you for sharing your time and experience. Inparticular: Dr. Jonathan Adams for technical drawing in Solidwork; Hahid Hosseini and Mélanie Hannebelle for relevant matters in piezoelectric actuators and LabVIEW programming; Oliver Peric for image processing software; Dr. Alexander Eskandarian and Dr. Soma Biswas for perspectives in biological systems; Maja for Matlab data processing; Santiago Andany for some technical reviews on my thesis;

I am also grateful to Prof. Yuri Korshev, Prof. Andrew Shevchuk and Prof. Pavel Novak for receiving me as a guest at Imperial College London and also for sharing their knowledge and perspectives in SICM.

I also want to thank to the following people at Instituto Superior Técnico: Prof. Susana Freitas, Dr. Carla Caramujo and Prof. Luís Fonseca for their assistance during my master thesis and lectures.

Abstract

Scanning ion conductance microscopy (SICM) uses ionic currents for topography imaging to study surface details in living cells. This type of scanning probe microscopy has proven to be a powerful tool for the deeper understanding of biological systems, with a large branch of applications.

Here, we describe an innovative design and construction of a SICM from scratch. In this respect, the project involves all mechanical design and instrumentation, as well as the creation of an electrochemical system that generates the low current used in the measurements. A new control system, including the acquisition software and hardware communication, has been created. Complementary, a compact software that simulates SICM imaging modes and characterize pipettes was developed.

Towards the end, we evaluate the scanning performance for of an innovative sensitive backstep hopping mode. An accurate tracking of the setpoint during a measurement was reported for the scanning of complex and non-adherent structures, under the diffraction limit.

Key-words:

Scanning ion conductance microscopy (SICM), design and construction, SBH mode, performance.

Resumo

Microscopia de condutância iónica (SICM) usa correntes iónicas para gerar imagens topográficas e estudar a superfície de células vivas em detalhe. Este tipo de microscopia de sonda tem provado ser uma ferramenta bastante útil para na compreensão de sistemas biológicos, com uma vasta área de aplicações.

Este projeto descreve a conceção e construção inovadora de um SICM. Mais especificamente, o projeto envolve todo o design mecânico e instrumentação, assim como a criação de um sistema eletroquímico que gera a corrente usada nas medições. Um inovador sistema de controlo foi desenvolvido, incluindo o software de aquisição. Complementarmente, foi criada uma aplicação que simula modos operacionais em SICM e que caracteriza as nanopipetas.

No final, a performance do microscópio desenvolvido foi testada para um novo modo operacional- Sensitive Backstep Hopping Mode. Imagens topográficas de estruturas complexas não aderentes foram obtidas com sucesso assim como resoluções abaixo do limite da difração de luz.

Palavras-Cháve:

Microscopia de condutância iónica, design e construção, modo SBH, performance.

Index

Chapter 1 1

Introduction 1

Project structure 2

Chapter 2 3

2. Theory Overview and Framework 3

2.1. Scanning Probe Microscopy 3

2.2. Scanning Ion Conductance Microscopy 5

2.2.1. Principle and Theoretical Modeling 5

2.2.2. Imaging Modes 8

2.2.2a. Constant Z mode 8

2.2.2b. DC mode 8

2.2.2c. AC mode 9

2.2.2d. Hopping mode 9

2.2.3. Imaging Techniques and Applications 11

2.2.3a. High Resolution Topography 11

2.2.3b. Smart Patch-Clamp 12

2.2.3c. Mechanical Stimulation 12

2.2.3d. Localized Delivery and Sampling 12

2.2.3e. SICM-SECM with a ring electrode or double barrel probe 12

2.2.3f. Scanning Electrochemical Cell Microscopy (SECCM) 13

2.2.3g. Potentiometric SICM (P-SICM) 13

2.2.4. Advantages over Conventional Microscopies 14

Chapter 3 18

3. Modeling and Simulations 18

3.1. Pipette inner radius estimation 19

3.2. Approach curve estimation 20

3.3. SICM scanning mode simulation 21

Chapter 4 23

4. SICM Construction 23

4.1. SICM Design 24

4.1.1. Nanopipette holder design 24

4.1.2. SICM control support design 24

4.1.3. SICM platform design 25

4.2. SICM Manufacturing and Assembly 26

4.2.1. Nanopipette holder manufacture 26

4.2.2. SICM control support construction 27
4.2.3. SICM platform construction 29
4.2.4. SICM final setup assembly 31
Chapter 5 33
5. Electrochemical system 33
5.1. Electrodes 33
5.2. Nanopipettes manufacturing 36
5.3. Approach Curves characterization 39
Chapter 6 42
6. Control System 42
6.1. Main Control System 42
6.2. Piezoelectric stages 43
6.3. Acquisition Software 44
6.3.1. Real time interface 44
6.3.1a. Approach to the surface 44
6.3.1b. Approach curve characterization 45
6.3.1c. Scanning 45
6.3.1d. Data Processing 46
6.3.2. FPGA interface 47
Chapter 7 48
7. Imaging Performance 48
7.1. DC Mode 48
7.1.1. Implementation 48
7.1.2. DC Scanning 49
7.2. Sensitive Backstep hopping mode (SBH mode) 50
7.2.1. Implementation 50
7.2.2. Backstep Scanning 51
Chapter 8 54
Conclusion 54
Annexes 55
Bibliography 88

List of Figures

Figure 1 | Typical SICM images 1
Figure 2 | Schematic diagram of an SPM experimental setup 3
Figure 3 | Principle of the scanning ion conductance microscope 5
Figure 4 | Approach Curve in SICM 6
Figure 5 | Imaging modes in SICM 9
Figure 6 | Hopping mode in SICM 10
Figure 7 | Imaging techniques in SICM 11
Figure 8 | Different Microscopies in Biology 14
Figure 9 | Complex features on cell membrane 16
Figure 10 | Observable Force Range of SICM and AFM for Various Cell Types 16
Figure 11 | Comparing AFM scanning of Human embryonic stem cells scanning with SICM imaging..... 17
Figure 12 | *SICM prediction* Matlab based application 18
Figure 13 | Inner radius of pipettes by SEM 19
Figure 14 | Overlapping of approach curve measured with simulated curve 21
Figure 15 | SICM DC mode scanning simulation 22
Figure 16 | SICM adapted to an inverted optical microscope 23
Figure 17 | Nanopipette holder design 24
Figure 18 | SICM main head design 25
Figure 19 | SICM main platform design 25
Figure 20 | Nanopipette holder manufacturing 26
Figure 21 | SICM main head manufacturing 27
Figure 22 | Assembly of the pipette holder and the main head 28
Figure 23| SICM main platform manufacturing 28
Figure 24 | Assembly of the adapting table 29
Figure 25 | Assembly of the pipette holder, the main head and table 29
Figure 26 | Inverted optical microscope 30
Figure 27 | Combined SICM setup 30
Figure 28 | SICM isolation cage 31
Figure 29 | SICM electrodes 32
Figure 30 | SICM electrodes manufacturing 33
Figure 31 | Electrode-Electrolyte contact interface inside of the pipette 33
Figure 32 | Electrodes characterization 34
Figure 33 | Electrodes placed in nanopipette holder 34

Figure 34 | Storing Pipettes 35
Figure 35 | Pipette tip characterization 37
Figure 36 | Pipette setting-up 37
Figure 37 | Approach curves 38
Figure 38 | Approach curves characterization 39
Figure 39 | System Noise 39
Figure 40 | Z piezo displacement Vs Current 40
Figure 41 | Current Drift 40
Figure 42 | SICM control system 41
Figure 43 | XY stage controller 42
Figure 44 | XY stage displacement 42
Figure 45 | Labview Real-time user interface 43
Figure 46 | Scan traces 44
Figure 47 | Image reconstruction 45
Figure 48 | Labview FPGA interface 46
Figure 49 | Feedback controller 47
Figure 50 | PID response 47
Figure 51 | DC mode scanning of a flat surface 48
Figure 52 | Hoping mode scanning 49
Figure 53 | XY stage displacement 50
Figure 54 | PDMS Meander cooper line calibration sample 50
Figure 55 | Complex cut PMMA sample 51
Figure 56 | Stretched tape scanning 52
Figure 57 | Stretched tape scanning in higher resolution 52

List of Tables

Table 1 | SPM techniques and respective properties 4

Table 2 | Characteristics of classical imaging modes in SICM 8

Table 3 | Pipettes characterization for several batches 36

List of Abbreviations

SICM Scanning Ion Conductance Microscopy

SPM Scanning Probe Microscopy

STM Scanning Tunneling Microscopy

AFM Atomic Force Microscopy

DC Direct Current

AC Alternating Current

SECM Scanning Electrochemical Microscopy

SECCM Scanning Electrochemical Cell Microscopy

P-SICM Potentiometric Scanning Ion Conductance Microscopy

MRI Magnetic Resonance Imaging

PET Positron Emission Tomography

HMC Hoffman Modulated Contrast

DIC Differential Interference Contrast

TIRF Total Internal Reflection

SIM Structured Illumination Microscopy

PALM Photoactivated Localization Microscopy

STORM Stochastic Optical Reconstruction Microscopy

SEM Simulated Emission Microscopy

TEM Transmission Electron Microscopy

DNA Deoxyribonucleic acid

CNC Computer Numerical Control machining

FPGA Field Programmable Gated Array

ADC Analogic to Digital Converter

DAC Digital to Analogic Converter

PID proportional-integral-derivative controller

SBH Sensitive Backstep Hopping

Chapter 1

Introduction

Ionic current is a central process in transmembrane signaling and is crucial for cells in keeping their proper physiological equilibrium [1]. Measuring such ionic currents averaged over many channels per cell is well-established using patch-clamp techniques [2]. Resolving single ion channels however (with diameters of a few nanometers) and imaging their distribution on the surface of the cell is much more challenging.

Scanning ion conductance microscopy (SICM) is a new microscopy technique that is potentially capable of achieving this. SICM utilizes the ionic current through a micropipette as a mechanism to create nanometer-resolution surface maps of biological samples that are submerged in an electrolyte solution [3]. The advantages of SICM over other techniques are twofold: it can generate topographical surface maps without any physical contact with the surface and it can measure the local ionic current with high spatial resolution. This ability makes this technique especially useful for imaging cell surfaces and local imaging of ionic currents through ion channels on cellular membranes [4], with a remarkable impact on non-adherent cells imaging, as shown in the figure below.

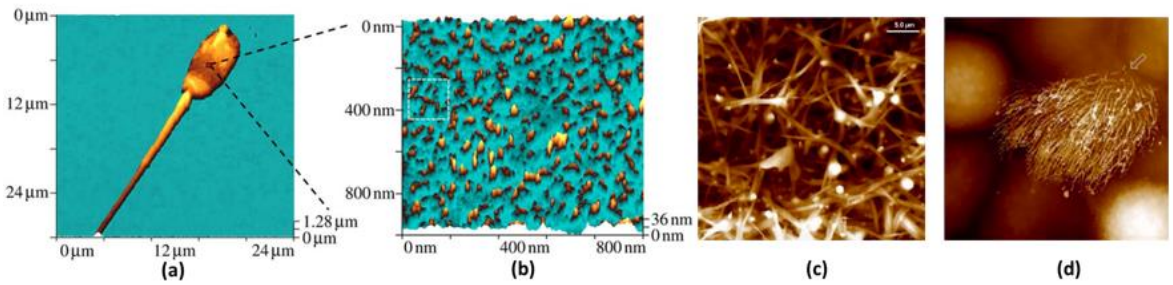

Figure 1 | Typical SICM images. SICM allows the scanning in high resolution of cell surfaces, such as a spermatozoid surface (a), where we can observe membrane proteins (b) by Klenerman et al. SICM also allows the imaging of suspended cells, such as a network of neurons (c) and rat trachea cell (d) obtained from Ushiki el al.

The proposed project entails all the relevant theory behind SICM, physic models applied to simulations and useful predictions, the design of microscope structure, manufacturing and assembly of all components. Followed by the implementation of all the electronics required and the programing of the acquisition software, to generate a final image.

In sum, this project comprises all the construction of a SICM from scratch to a functional form. Moreover, we aim a SICM that can adapt into an inverted fluorescence microscope system for further applications in cellular biology.

Project structure

The structure of this project, which covers the steps required to build a scanning ion conductance microscope, is organized as follows:

- **Fundamental concepts | Chapter 2** presents the relevant overview concerning the bases of SICM for the developing process.
- **Physical modeling and simulations | Chapter 3** presents mathematical models applied for the creation of a compact software that simulates SICM imaging modes and pipette characterization.
- **Design and construction | Chapter 4** describes the design of the microscope, technical drawings, manufacturing and assembly.
- **Electrodynamics system | Chapter 5** presents the electrochemical system, including the manufacturing process for the electrodes and pipettes; as well as characterization of the resultant approach curves.
- **Control system | Chapter 6** presents the control system, including the hardware communication, acquisition software and piezoelectric stage characteristics.
- **Scanning Performance | Chapter 7** shows the imaging performance for DC mode scanning and the implementation of sensitive backstep hopping mode.
- **Conclusion | Chapter 8** draws conclusions and presents outlook for future improvement and ideas for further work.

Chapter 2

2. Theory Overview and Framework

2.1. Scanning Probe Microscopy

Scanning Probe Microscopy (SPM) is a generic name given to a certain branch of microscopy technique characterized by the capability to scan and study surface details [5].

Typically, an SPM experimental setup is composed by a probe that moves through the sample, with a range in the XY direction in the nanometer range. The interaction between the probe and surface is measured by sensors. Then, the signal is processed by a controller that handles the data, controlling the piezo actuators movement and the probe's vertical position by means of a feedback system.

In this way, it is possible to build up a three dimensional image, displaying it on a screen. A schematic of an SPM setup can be seen *Figure 2*.

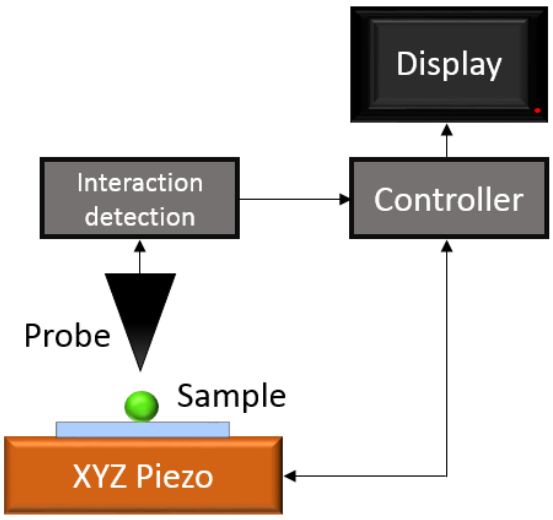

Figure 2 | Schematic diagram of an SPM experimental setup. In general SPMs are composed of a probe interacting with a sample. That interaction is detected and the parameters inherent to the scanning are managed by a controller, showing the image generated in a display screen [9].

The physical principles present in the probe-sample interaction form the basis of different SPM techniques. For example, Scanning tunneling microscopy (STM) uses tunneling electron

currents that flow between a sample and a sharp metal tip used as a probe [6], to scan conductive surfaces. On the other hand, atomic force microscopy (AFM) allows the imaging of both conducting and insulating surfaces by the use of a force sensitive cantilever. The force interacting between the sample surface and the tip causes the deflection of the cantilever, and can be detected by an optical system. Table 1 shows a list of some SPM techniques, all of which are variants of STM [7].

Table 1. SPM techniques and respective properties [7].

SPM technique	Acronym	Measuring interaction	Remarks
Ballistic electron emission microscopy	BEEM/STM	Electron current	Unfeasible for imaging biological samples
Chemical force microscopy	CFM/AFM	Van der Waals interactions	Complex tip preparation
Conductive atomic force microscopy	C-AFM/AFM	Current–voltage curves	Used on conductive and semiconducting surfaces
Electrochemical scanning tunneling microscopy	ECSTM/STM	Redox reactions	Used in electroplating and batteries
Electrostatic force microscopy	EFM/AFM	Electrostatic force	Sample can be immersed in solution
Magnetic force microscopy	MFM/AFM	Magnetic interactions	Used on magnetic samples
Photothermal microscopy	PTM/AFM	Infrared Fourier transform	Poor image resolution
Scanning electrochemical microscopy	SECM/AFM	Electrochemical activity	Poor image resolution
Scanning capacitance microscopy	SCM/AFM	Capacitance between probe and sample	Requires a conducting surface
Scanning ion conductance microscopy	SICM/AFM	Ion conductance just above sample	Feasible for imaging live cells in solution

2.2. Scanning Ion Conductance Microscopy

2.2.1. Principle and Theoretical Modeling

Scanning ion conductance microscopy (SICM) is a type of SPM, particularly useful in investigating biological samples [5]. It uses a micropipette, filled with ionic solution, as a probe. Two electrodes, one of them inside the micropipette and the other one in solution, are connected across a voltage supply so that a circuit is formed. The sample to be examined is also placed in the solution.

A schematic of a typical SICM setup is shown in *Figure 3a*, and the equivalent electric circuit is represented in *Figure 3b*, where the variable resistance *Rs* is represented as a potentiometer.

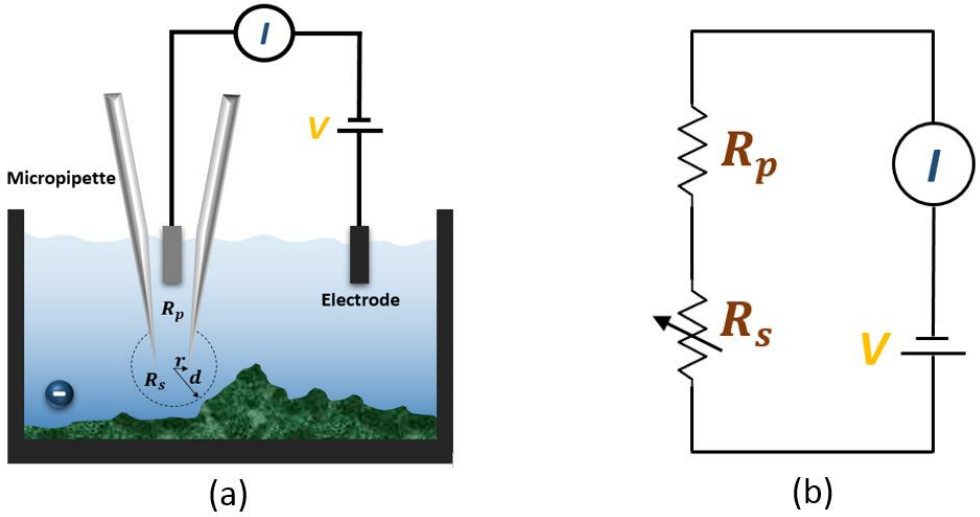

Figure 3 | Principle of the scanning ion conductance microscope. A typical SICM setup (a) shows two resistances when a voltage *V* is applied and a current generated, flowing through the solution between the electrodes. Here, we have a constant resistance *Rp* and a variable one *Rs*, which changes as a function of pipette position *d*. The equivalent electric circuit is drawn in (b). Adapted from [4].

Because the voltage applied V is known, the current I in the circuit is determined by its total resistance, through ohm's law, $V = IR$. The total Resistance in the circuit is comprised of two parts, *Rp* and R_s .The first resistance is determined by the geometry of the pipette while R_s is function of the distance, *d,* between the surface and the probe, the pipette radius and finally electrochemical properties of the sample surface [4].

The current *I* through the pipette is given by

$$I = \frac{V}{R_p + R_s(d)} \tag{1}$$

The distance d is the difference between the initial distance d_0 and the piezo deflection z:

$$d = d_0 - z \tag{2}$$

A normalized approach curve can be approximated as

$$\frac{I(d)}{I_{max}} = \frac{R_p + R_s(d)}{R_\infty} = 1 + \frac{D}{d} = 1 + \frac{D}{d_0 - z} \tag{3}$$

where R_∞ is the resistance when the pipette is far from the surface, $R_p + R_s(\infty)$, and the current is maximum I_{max}, D denotes the tip-sample's distance that doubles the resistance, determined by the geometric properties of the electrode and the electrolyte. The parameter d_0 and D can be determined by numerically fitting this equation to the data [8].

The position of the micropipette strongly influences the access resistance *Rs*, therefore the ionic flow decreases when the pipette approaches the surface, starting from the position where that distance, *d*, is equal to the pipette's inner radius *r*. A setpoint is defined as a control value to avoid contact with the sample and consequently avoiding micropipette crashing. The slope at the setpoint gives the probe's sensitivity, which is set in order to get a precise topographical information about a sample. *Equation 3* is used as model to fit and obtain accurate characterization of the approach curve, as shown in *Figure 4.*

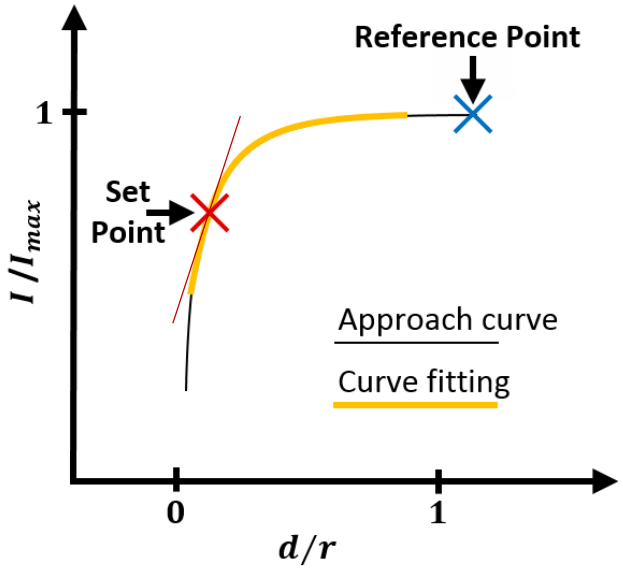

Figure 4 | Approach Curve in SICM. The physical principle of SICM is the drop in current that occurs when the probe approaches the surface and *Rs* increases. Then, a set point is defined from where the pipette position is recorded to generate an image, to a reference point. For further characterization, this curve is fitted and the slope at the setpoint corresponds to the pipette's sensitivity.

The resistance of the pipette itself can be approximated as

$$R_p \approx \frac{cot(\theta/2)}{\kappa\, \pi\, r_i}, \tag{4}$$

where θ is the cone angle between tip walls and the pipette's central axis, κ the conductivity of electrolyte solution, and r_i is the inner radius of the micropipette [7].

On the other hand, the resistance of the pipette opening can be approximated as

$$R_s \approx \frac{\frac{3}{2} ln\left(r_o/r_i\right)}{\kappa\, \pi\, d}, \tag{5}$$

where r_o is the outer radius of the pipette.

So, the current I as function of distance d, is given by

$$I = V\left(\frac{\kappa\, \pi\, r_i}{cot(\theta/2) + \frac{3r_i}{2d} ln\left(r_o/r_i\right)}\right) \tag{6}$$

This equation will be used to predict pipette sensibility in *Chapter 3*.

2.2.2. Imaging Modes

Since the invention of SICM, a wide range of imaging methods have been developed in order to determine the sample's topography. A brief overview of the imaging modes is provided in *Table 2*.

Table 2 | Characteristics of classical imaging modes in SICM [8].

Mode	Temporal Resolution	Topography	Remarks
Constant z	Good	Very flat	Barely used for imaging topography. Extremely flat surfaces
DC	Good	Flat	Fails to detect step differences in sample height, prone to electrode drifts, likely to contact the sample
AC	Good	Moderate	Detects intermediate differences in sample height, images at a larger distance.
hopping	Bad	Complex	Best for imaging entire cells and complex sample topography, very low temporal resolution, various enhancements available

First of all, in SICM the pipette is lowered towards the surface until a resistance change is detected. After that, an initial approach curve is done to establish a setpoint before scanning.

2.2.2a. Constant Z mode

In z-constant mode, *Figure 5a*, the pipette is moved laterally at a constant *z*-position and the resistance is monitored and the topography is calculated. The distance, *d,* between tip and sample can be calculated using *Equation 2*, defining a reference point, d_0, and assuming the conductivity of the electrolyte solution as constant. While this mode is characterized by a very good temporal resolution, only extremely flat surfaces with small changes in height can be scanned while avoiding pipette crashing.

2.2.2b. DC mode

Similarly to constant Z mode, once the probe is approached to the sample in DC mode, the pipette is moved laterally, *Figure 5b*. However, in this case, a predefined threshold resistance, defined as setpoint, is used as a feedback signal that modulates the *z*-position of the probe. Then, the topography is constructed by measuring the relative z-position of the piezo actuator that holds the pipette. The image resolution is highly dependent on the diameter of the nanopipette, providing resolutions under 200 nm [9].

DC mode scanning of samples with abrupt topological changes is problematic as it leads to lateral tip-sample collisions. Moreover, DC mode can suffer from loss of feedback control when the value of the measured current varies by 0.2–3% from its initial setpoint [9]. This usually occurs while scanning over long periods of time. In addition, this mode is highly susceptible to electrode drifts, like current instability and electronic noise at the surface potential of the Ag/AgCl-electrodes, further limiting the effectiveness of the technique.

2.2.2c. AC mode

In AC mode, *Figure 5c*, *z*-position is modulated by alternating current (AC), consequently the resulting resistance is sinusoidal while the pipette is moved laterally close to the sample. The amplitude of the sinusoidal resistance, in the range of 1kHz–2 kHz [10], is used as a feedback to modulate the *z*-position. Similarly to DC mode, the opening size of the pipette also determines the image resolution. A precision of 2 nm in position control can be achieved [11] using the right gain settings.

The main advantage of this mode is the sensing of the surface at larger distances when compared with DC mode, enabling the record of steeper slopes and more complex samples. Furthermore, AC modeling is less prone to DC drifts, offering a minimal electrode drift.

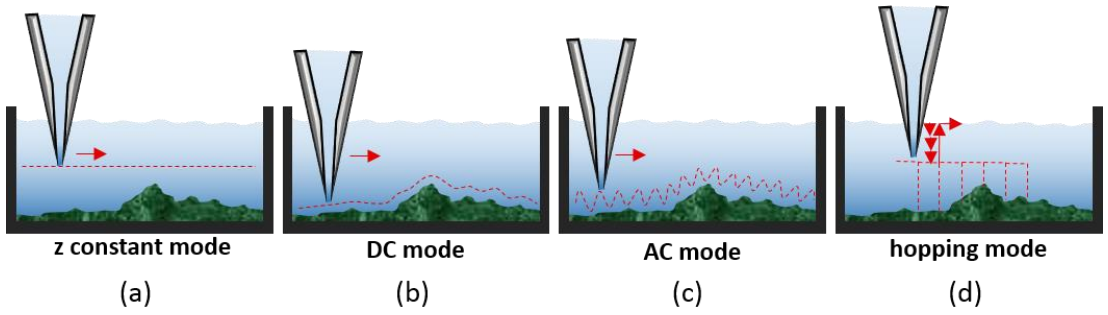

Figure 5 | Imaging modes in SICM [8]. Classical imaging modes in SICM are: Constant z mode (a) where the pipette maintains the same position during the measurement and the change in current is used to generate the image; DC mode (b) when the current is maintained constant during the measurement and the displacement in pipette position is used to generate the image based on feedback system; AC mode (c) is similar to DC, but in this case the pipette position is modulated alternately; and hopping mode (d) when an approach curve is generated for each point of the surface.

2.2.2d. Hopping mode

Usually, the AC mode enables better results than DC mode, providing stable recordings for samples with moderate sample topography. However, both operational modes are susceptible to collision with abrupt slopes as is frequently seen at the edge of cells. This limitation has been

overcome by introducing a non-continuous mode that retracts the scanning probe after the surface has been sensed.

Similarly to AFM tapping mode, in this hopping approach method, the pipette is lowered towards the sample from initial position, green ring in *Figure 6*, until a predefined resistance is reached, the setpoint, represented in figure bellow as red ring. The setpoint corresponds to the decay in percentage (%) of the maximum current represented as a blue ring in figure bellow. The pipette is then dragged back, moved laterally and the process repeats.

To construct the sample topography, the *z*-positions at which the approach has been stopped is compared with a reference point. Every single pixel point is refreshed against reference current value before approach to avoid thermal drift.

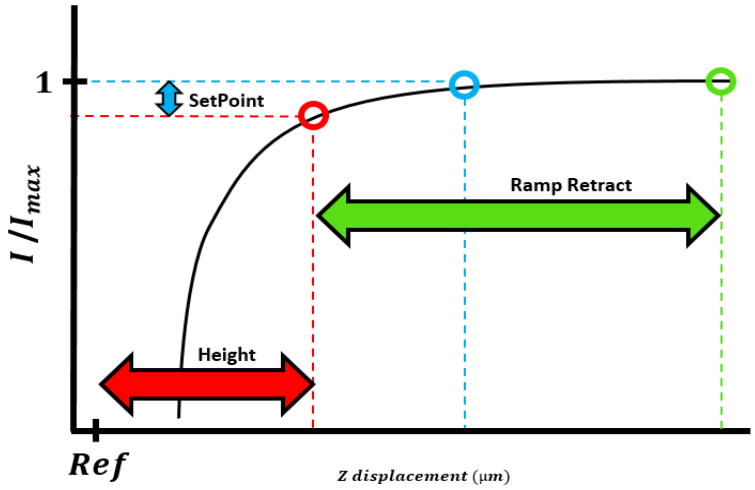

Figure 6 | hopping mode in SICM. SICM hopping mode is the preferable mode scanning, since it is possible to image complex samples without breaking the pipette. Here the probe approaches the surface from an initial position (green ring) until reach a setpoint (red ring), defined as a certain decreasing of the maximum current (blue ring), usually in percentage.

Since the recording of every pixel requires an entire approach curve over a relatively large distance, scanning speed is inevitably slow. To increase the temporal resolution the usage of a low resolution pre-scan of the sample has been introduced [12].

This mode will be implemented in this projected microscope using Labview code based programming.

2.2.3. Imaging Techniques and Applications

In recent times, SICM has become a powerful tool for the understanding of fundamental matters in several areas of cell biology. The usefulness and a unique characteristic of this type of microscopy, is that it allows high resolution imaging of live cells without affecting or damaging the sample [13, 14], and capturing cell activity by monitoring membrane dynamics in real time [15]. In addition, the probe can be used to stimulate cell activity and capture the various cell responses [16]. Moreover, the pipette is also capable of serving as a delivery vehicle for drug administration [17]. All of the above-mentioned techniques are covered in detail below, and represented in *Figure 7*.

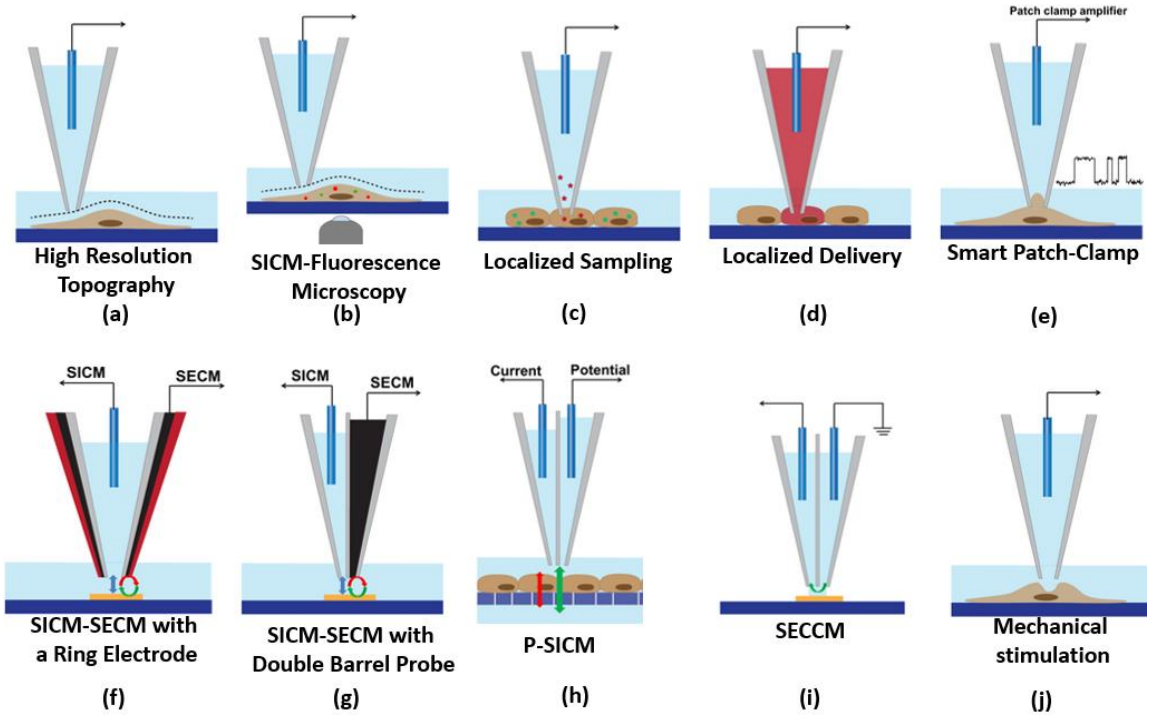

Figure 7 | Imaging techniques in SICM [18]. The most common technique in SICM is high resolution topography and its combination with Fluorescence microscopy (b), however this microscopy can also be adapted to specific techniques, like smart patch-clamp (e), mechanical stimulation (j), localized sampling (c) and delivery (d), where the pipette is moved to a particular point with precision. It is also possible to combine SICM with scanning electrochemical microscopy (f, g) and scanning electrochemical cell microscopy (i), as well as a potentiometric technique.

2.2.3a. High Resolution Topography

The primary technique in SICM, as mentioned in the figure above, is the high resolution imaging of the topography of live samples in electrolyte (*Figure 7a*). A characteristic of this type of microscopy is the relatively easy fabrication of pipettes used as probe and the fact that it is a non-invasive approach since there is no contact between the surface and the probe. This scanning

method allows imaging of living cell and delicate material morphology as well as long-term observation of cell growth [19].

2.2.3b. Smart Patch-Clamp

SICM can also be used as a smart patch-clamp tool, *Figure 7e*, where the probe can be used both for scanning and as a patch clamp. The main advantage of SICM smart patch-clamp is the positioning of pipette with high spatial resolution, with higher patch success rate, working on non-transparent samples. Major applications are the study of ion channels weather on samples difficult in conventional patch clamp or on small membrane features (~100nm) [20].

2.2.3c. Mechanical Stimulation

Another possible technique is mechanical stimulation, *Figure 7j*. This is achieved by applying a positive pressure on the pipette, with minimum or no damage, as there is no contact. This stimulation is limited in a very small region and applied to the mechanical sensitivity mapping of cells [21].

2.2.3d. Localized Delivery and Sampling

Localized delivery is also possible using SICM, *Figure 7d*. It allows fast delivery with minimum damage to the cell. It can be used for localized staining to facilitate optical imaging and nanowriting with controlled deposition trough the pipette [22]. In contrast with localized delivery, it is also possible to execute localized sampling, *Figure 7c*, by obtaining material for further analysis from a single cell with minimum damage to the cell. This is achieved by through the small size of the nanopipette. This leads to application is nanobiopsy and single cell analysis [23].

2.2.3e. SICM-SECM with a ring electrode or double barrel probe

SICM can also be conjugated with Scanning Electrochemical Microscopy (SECM) with a ring electrode, figure 7f, or with a double barrel probe, figure 7g. In the first case we have a multifunctional probe with coating of conductive material and insulation outer layer. A robust feedback SICM controls probe to sample distance, and ring shape SECM electrode measures local electrochemical property [24]. In the second case, SICM-SECM with double barrel probe is characterized by a barrel of carbon deposited in one side of the pipette, *Figure 7f*. Compared to

the ring electrode, this second method is easier to fabricate. Both are used for correlation of local topography and electrochemical property in both life and material science [25].

2.2.3f. Scanning Electrochemical Cell Microscopy (SECCM)

Scanning Electrochemical Cell Microscopy (SECCM) is another method based on SICM, *Figure 7i*, but in that case, the scanning is executed in air. This is possible by the fact that the current is flowing in the meniscus between the two barrels and the cell. It is applied to electrochemical mapping of materials [26].

2.2.3g. Potentiometric SICM (P-SICM)

Potentiometric technique is also possible combined with SICM, *Figure 7h*, using a double barrel pipette. One measures current for SICM distance control while the second barrel measures the potential at the tip of the pipette, allowing higher signal-to-noise ratio for potential measurement. It can be used for localized conductance measurement in syntactical porous membrane and cell monolayers, such as paracellular transport of tight junctions in epithelial cells [27].

2.2.4. Advantages over Conventional Microscopies

Microscopy in biology is an essential tool for the deeper understanding of live systems. It allows us to take a close look on biological features. These microscopies differ from each other, depending on the principle used, which determines the resolution achieved and the degree of interaction with the sample imaged. The characteristic of each type microscopy, in accordance with the specimen to be imaged, determines the best microscopy applied to a specific case.

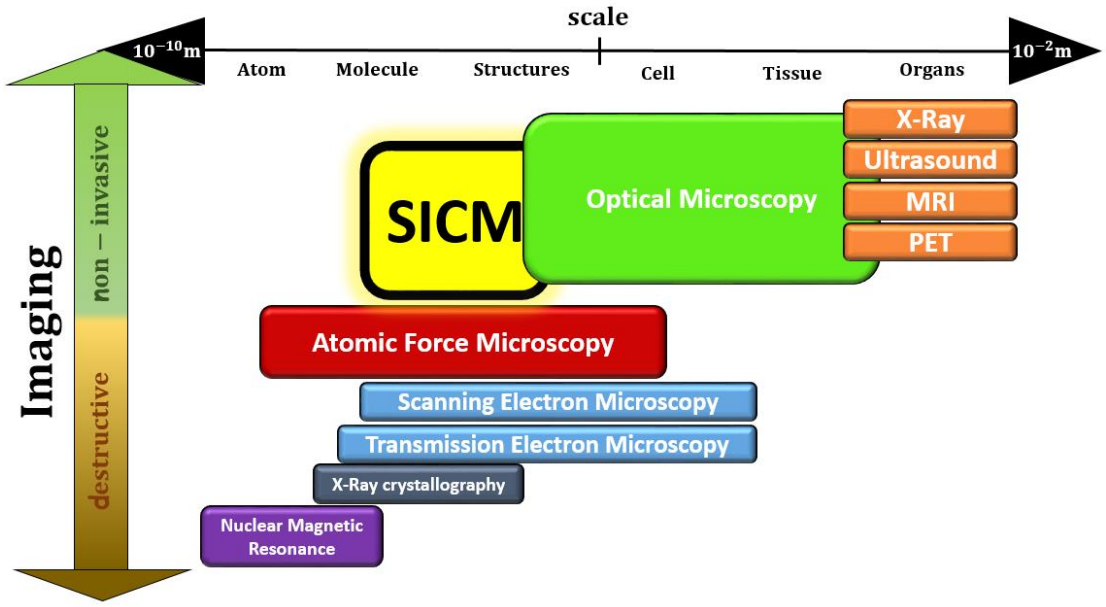

Figure 8 | Different Microscopies in Biology [18]. There are many kinds of microscopies applied to biology, each one with different characteristic, advantages and disadvantages. SICM is unique and a powerful tool in this field, because is a non-invasive technique that allows imaging in high resolution, becoming a perfect tool in cell research.

Non-invasive techniques, such as x-ray , ultrasound , magnetic resonance imaging (MRI), positron emission tomography (PET), have been used to obtain images of biological features without damaging the living components. Nevertheless, the resolution of such techniques are relatively poor [28, 29, and 30].

Conventional optical microscopy is the most widely used technique in scientific research to study cell dynamics over long periods of time and to monitor intracellular processes. These processes include cell migration, cell division, organelle dynamics, apoptosis, differentiation, neural process outgrowth, etc. Advanced contrast-enhancing techniques, like phase contrast, hoffman modulated contrast (HMC) and differential interference contrast (DIC), are often applied to cell dynamics and can be used in a wide range of samples over long time periods [31, 32, 33]. Furthermore, advanced fluorescence techniques such as laser scanning confocal, spinning disk, and total internal reflection (TIRF), microscopy are progressively being used to monitor intracellular processes over time. However, the resolution of this type of microscopy is above

300nm, and some of them can damage the sample such as in the case of dark field microscopy [34, 35, 36, and 37].

Some super resolution fluorescence techniques have been developed, namely structured illumination microscopy (SIM) with resolutions above 100 nm, stimulated emission depletion microscopy (SEDM) with resolutions under 100 nm and photoactivated localization microscopy/ stochastic optical (PALM/STORM) with resolutions under 50 nm. Disadvantages are a Post-Processing requirement and the fact that reconstruction bears risk of artifacts. Besides that, it is almost impossible to image live cells [38, 39, and 40].

In order to obtain high resolution images, scanning electron microscopy (SEM) and transmission electron microscopy (TEM) were developed, providing a resolution in the range of 0.5-10 nm [41, 42]. Yet, it is not possible to scan live samples and image artifact. Moreover, they are relatively costly and fairly time-consuming. x-ray crystallography and nuclear magnetic resonance (NMR) are other branches of microscopy characterized by extremely high resolution imaging. However, as for the previous ones, it is not possible to use for live samples [43, 44].

Atomic force microscopy (AFM), which belongs to the SPM family and whose technical principle was briefly described before, is characterized by a high resolution imaging above 0.1nm. AFM is used for quantitative 3D information and can be applied to non-conductors as well as conductors and semiconductors, operating in air, liquid, and vacuum. It can be used on soft samples and wet samples, to measure electrical, magnetic, optical, mechanical properties, and also atomic scale manipulations and lithography. AFM for biological applications is used to scan cells membrane, membrane proteins and DNA, and to measure protein-protein interaction, DNA-protein interaction, cell-cell interaction and single molecule force spectroscopy [45, 46, 47, 48, 49, 50, and 51]. Cell dynamics, vesicle dynamics, and phase transition of phospholipid membrane is also possible to study using AFM, as well as biomolecular nanolithography (protein, nucleotide) and bio-Manipulator [52, 53, 54].

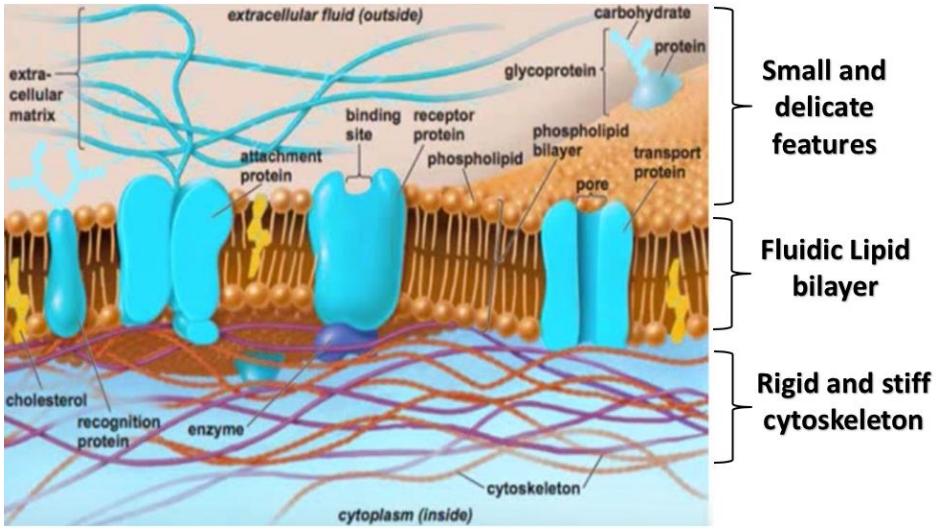

Figure 9 | Complex features on cell membrane [55]. The cellular membrane is very complex, composed by a rigid and stiff cytoskeleton, fluidic lipid bilayer, and small and delicate features. The biggest challenge in cellular scanning using SPM, especially AFM, is imaging without damaging this structures in cell membrane due to probe interaction with the surface. SICM has the capability to avoid this problem, since the probe never touches the sample.

Nevertheless, when AFM is applied to cell membrane scanning, some concerns are present. The cell membrane is very complex, *Figure 9*, composed by a rigid and stiff cytoskeleton, a fluidic lipid bilayer, and small and delicate features, including recognition proteins glycoproteins and carbohydrates. This small and delicate structures, and the rigidity of the extracellular matrix is a limiting factor of cell scanning by AFM.

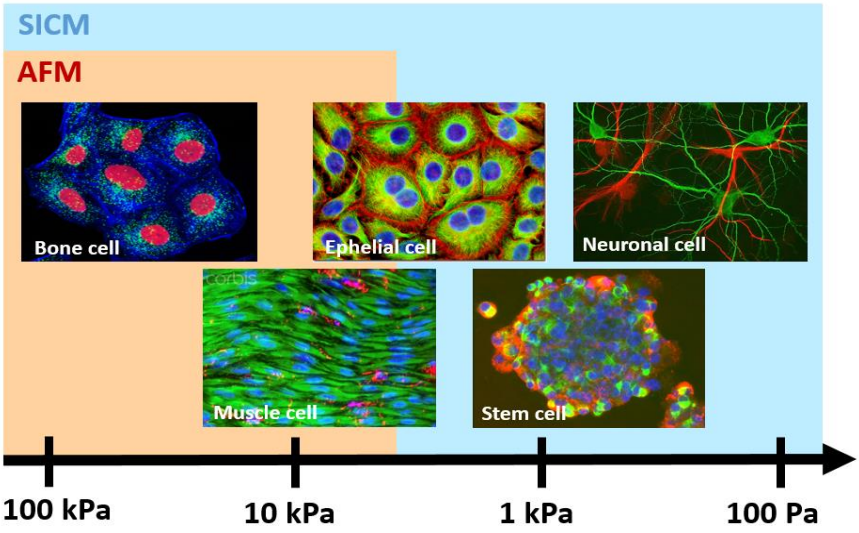

Figure 10 | Observable Pressure Range of SICM and AFM for Various Cell Types [55]. Many cell are sensitive to mechanical pressure. AFM is limited to scan cells a sensitivity range above 10kPa, becoming useless to scan samples, such as neuronal cells, stem cell and even epithelial cells. On other hand, SICM is not dependent of cell mechanical sensitivity.

In the AFM images of various cells, soft features on cellular membranes are not visible due to the force from the AFM cantilever, and only the cytoskeleton is imaged. While AFM is just applicable for rigid cells such as muscle and bone cells, *Figure 10*, SICM can image the softest cells such as the neuron cells or stem cells. Something that's impossible with any other microscopy techniques. SICM can even image suspended network of neurons.

For instance, in *Figure 11*, we see the difference in human embryonic stem cells scanning in liquid, using AFM (*Figure 11a*) and SICM (*Figure 11b*) respectively. Live cell membranes are far more complex than what is observed by AFM imaging, and in this case, with SICM it is possible to observe microvilli destroyed in AFM scanning [55].

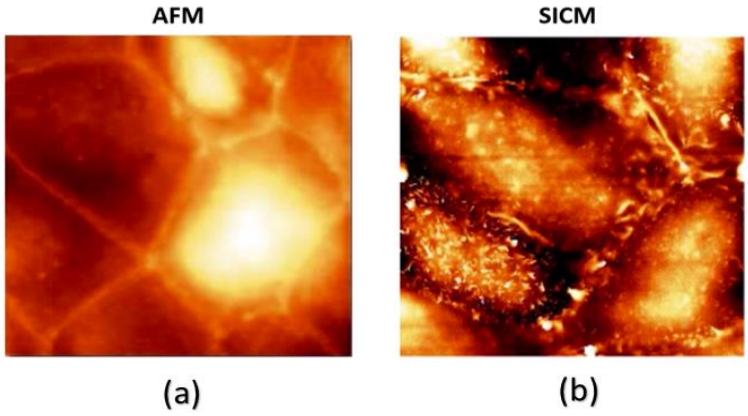

Figure 11 | Comparing AFM scanning of Human embryonic stem cells scanning with SICM imaging [55]. This is a clear example of the advantage of SICM (b) over AFM (a), for the scanning of soft and complex cell membranes. Using SICM is possible to image delicate features like microvilli as shown in this image, by Park systems.

Therefore, in comparison with other microscopy techniques, SICM is a unique tool, used to image live cell structure and cell membrane, biological interaction at cellular level and events by mechanical and ionic stimulation. SICM can give accurate morphology of fluidic cell structures, can image delicate subcellular structures, such as microvilli and projections on the cell membrane, without damage. SICM is a non-invasive imaging tool for very soft surfaces, and enables accurate height and width measurement in liquid. SICM can not only be used to generate topographical surface maps without any physical contact with the surface, but can also be used to measure the local ionic current with high spatial resolution. This ability makes this technique especially useful for local imaging of ionic currents through ion channels on cellular membranes. SICM has advantages over optical microscopy in that its resolution is not diffraction limited, and it is possible to manufacture probes with pipette opening smaller in size than the resolution of the most common optical microscopy techniques.

Such characteristics distinguish this kind of microscopy as a unique and powerful tool for cell research, with a remarkable impact on non-adherent cells imaging.

Chapter 3

3. Modeling and Simulations

This chapter shows a compact, user friendly application for modeling and simulating SICM. After reading and understanding fundamental, the project was started by implementing a MatLab based algorithm from scratch. Initially it was programed to simulate different modes in SICM, then adapted to estimate the inner radius of the pipette and to estimate approach curves. This Pipette characteristics are essential for resolution, with a critical role in the image quality and probe sensitivity. The functions of this MatLab based program can be divided as following:

- Pipette inner radius estimation.
- Approach curve estimation.
- SICM scanning mode simulation.

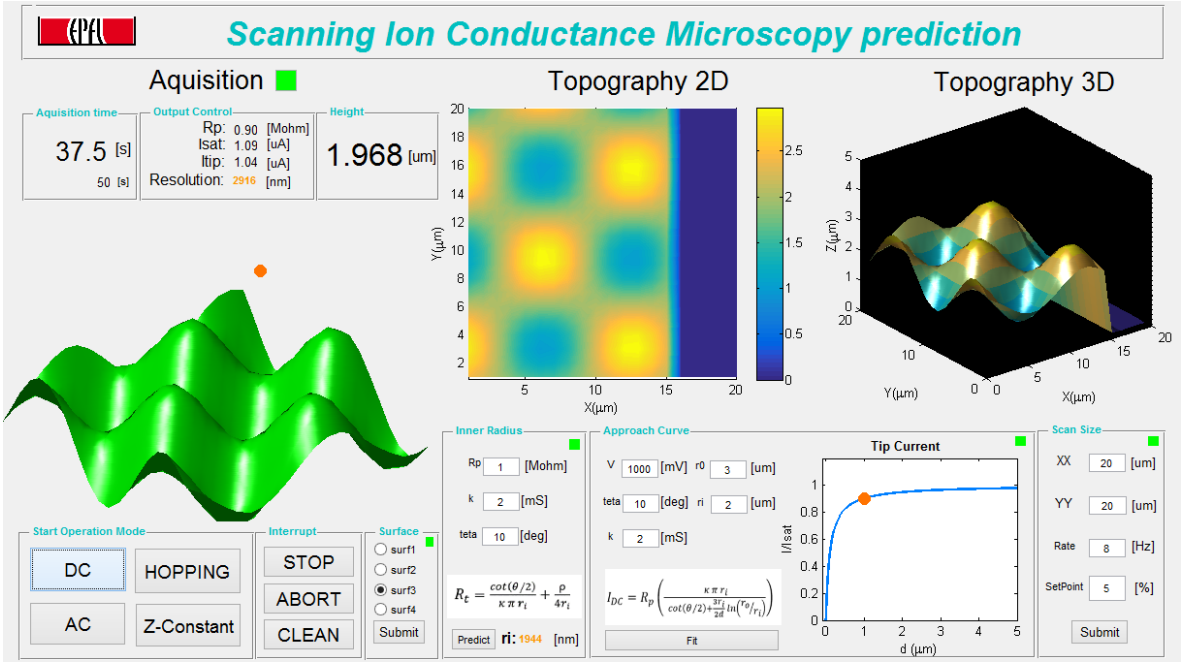

Figure 12 | *SICM prediction* Matlab based application. A compact user friendly application was created in order to characterize a huge amount of pipettes originated from different batches, by predicting its inner radius and approach curves. It also possible to simulate SICM DC mode scanning, where the dynamic orange blob corresponds to the opening of the pipette.

The SICM simulation software is shown in figure above (more detail in *Appendix A)*. Specific simulation cases, for pipette inner radius prediction, approach curve prediction, and SICM scanning mode simulation are presented in sections below.

3.1. Pipette inner radius estimation

Inner pipette radius estimation is very important for SICM measurements, because it gives an approximate idea of the resolution of the image, which is close to 1.5 times the r_i according to literature [56]. Since we are manufacturing pipettes for the first time, this estimation is even more important The alternative would be measuring the inner radius by electron microscopy (SICM), which is extremely expensive and time costly. We present our own model to calculate the inner radius based on simple assumptions.

Far from surface, access resistance of the pipette in *Equation 5* is approximately constant, and according with James E. Hall [57] can be simplified as

$$R_p \approx \frac{\rho}{4r_i} \tag{7}$$

where ρ is the resistivity, inverse of conductivity ($1/\kappa$), of our bath solution r_i is the radius of the pipette tip opening intended to predict using this program.

Regarding *Equation 4* for R_s, the total resistance, $R_t = R_s + R_p$, can be approximated by

$$R_t = \frac{cot(\theta/2)}{\kappa\, \pi\, r_i} + \frac{\rho}{4r_i} \tag{8}$$

Therefore, if we measure the current in the circuit at some large distance from any surface, knowing the voltage applied and the conductivity of the ionic solution we have in the bath, we can determine the total circuit resistance R_t. Using *Equation 8* we can use this calibration measurement to estimate the size of our tip opening r_i.

To exemplify this inner radius calculation using this program, pipettes from the first batch (*Table 3*) were used. The estimation of pipette opening in this case is about 3.5 µm, similar to the real inner radius seen in figure bellow.

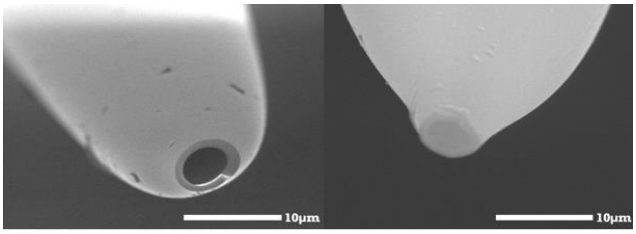

Figure 13 | Inner radius of pipettes by SEM. These are SEM images of the pipettes produced in the first batch, showing some discrepancy on tip shape. In (a), the tip external walls exhibits concave curvature and (b) exhibits convex curvature. It emphasizes the usefulness of this prediction model, since even pipettes from some batch exhibit different shape. The pipettes opening were predicted knowing the electrolyte conductivity approximated as 1.25 mS · cm (for 0.1 M KCl), and assuming the cone angle of tip walls make with the pipette axis as approximately 10^o. The total resistance R_t measured is equal to 0.9MΩ., by applying a voltage of 1V to electrodes terminal.

Appling this model to the initial batch, we can conclude that the resolution calculated, around 4.5 μm, is far away from the resolution pretended in this project. Comparing with SEM images of the same batch of pipettes, *Figure 13*, we can find that the inner radius predicted is indubitably close to the real radius. This estimating program has proven to be a useful tool to estimate the resolution we get with a given pipette.

3.2. Approach curve prediction

Approaching curve prediction is another important tool for pipette quality attestation. Once predicted, the approach curve of a particular pipette can be used to draw conclusions about the sensitivity of the pipette. The sensitivity is directly dependent on the inner radius r_i, which has a critical role on image quality and also depends on the pipette's shape.

The theoretical modeling of the resistance or ionic current observed in SICM derives from earlier *Equation 6*, which describes the relationship between observed ionic currents and tip-sample distances. The final model implemented in MatLab algorithm is obtained by normalizing the current I_{DC}, dividing by the maximum current, also called saturation current I_{sat}, when the pipette is far from the surface, given by

$$I_{sat} \approx \frac{\mathrm{V}}{R_p} \tag{9}$$

where V is the applied votage. The normalized ion current as a function of tip sample's distance dependence along the z-axis can be predicted by

$$\frac{I_{DC}}{I_{sat}} = R_p \left(\frac{\kappa \, \pi \, r_i}{cot(\theta/2) + \frac{3r_i}{2d} ln\left(r_o/r_i\right)} \right) \tag{10}$$

To model this current curve, the equation above was implemented and the predicted curve in function of the pipette displacement can be compared with the real approach curve. The approach curve measured was obtained using a pipette from batch one. A setpoint of 10% percent is used to prevent the pipette from crashing (*Figure 14*).

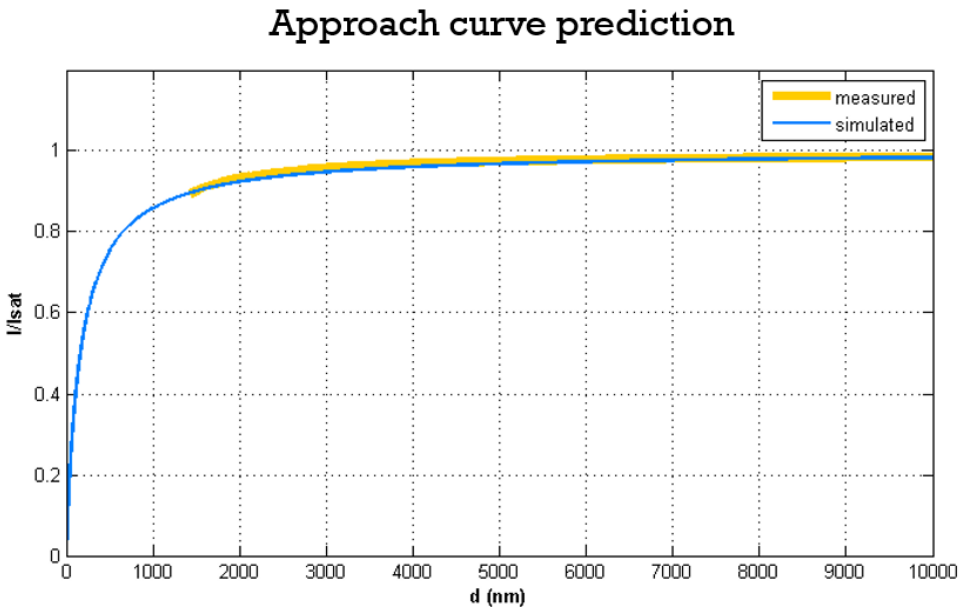

Figure 14 | Overlapping of approach curve measured with simulated curve. Accessing the pipette inner/outer of the first manufactured batch using SEM, an approach curve was simulated and then compared with a real approach curve of a pipette native from the batch. The simulated curve, represented as a blue line was obtained regarding inner radius r_i and outer radius r_o, approximately 3.5µm and 5µm respectively. This is done by observing the pipette SEM image in *Figure 13.*. The range simulated, d, comes from 0nm to 10000nm and θ assumed as 10^o. A bias voltage of 1V was applied and a conductivity of 1.25 mS/cm in 0.1M KCl solution was used.

Comparing measured current with simulated case, we can conclude that this model predicts the approach curves similarly to the real case, showing again that this simulation is useful and an accurate tool to judge the pipette's quality and respective pipette sensibility. For this first batch, looking at the approach curve, we conclude that the pipette sensibility is extremely bad, and this pipettes cannot be used to get images in the nm range.

3.3. SICM scanning mode simulation

This scanning mode simulation was developed in order to prepare basic programming methods inherent to each mode, to be implemented in LabView posteriorly. In this case, only the DC mode was implemented, based on feedback loop to control the pipette position in function of current readings, dependent on the surface distance.

Surfaces were previously created, by implementing simple mathematical functions. For instance, the green surface in *Figure 15b* and *15c* is modeled by $\cos(aX) \cdot \sin(bY)$ function, were a and b represent a constant value.

In *Figure 15*, a DC mode SICM scanning simulation is performed, with a resolution of 20 pixels by 20 lines and a sampling rate of 10Hz per pixel. Then, Height surface map and 3D topography is generated line by line and reconstructed by a Gaussian fit in real time.

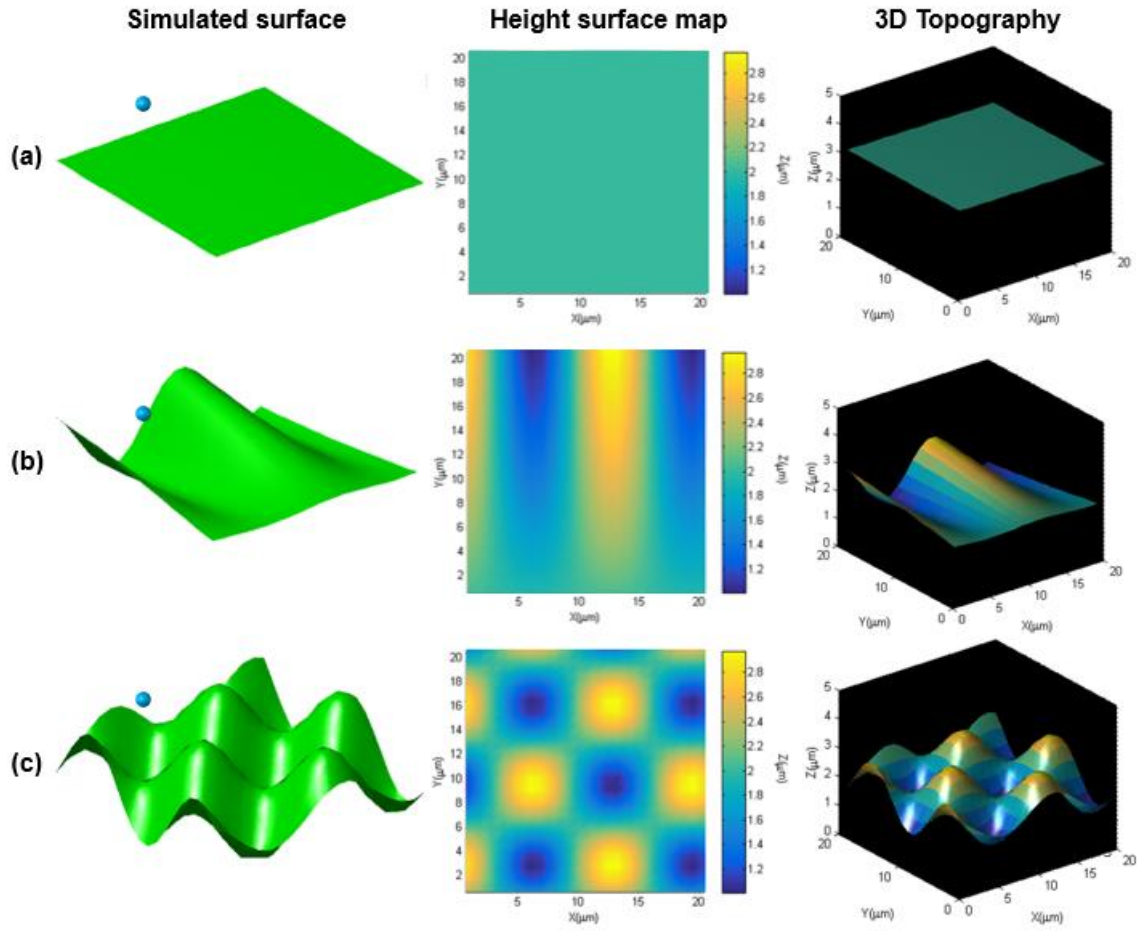

Figure 15 | SICM DC mode scanning simulation. Here I show a DC mode scanning simulation of a planar surface (a), a bended surface (b) and a sloped surface in (c). The blob in blue scans the surface and generates an height map and 3D map, 40 seconds each image since a rate of 10Hz is used. Before scan simulating, an approach curve must be first calculated. Then, the setpoint is set, a sampling rate and a scan area delimited. After that, by pressing the DC button, the pipette represented by the blue blob starts moving, pixel by pixel, and the position is recorded. The distance of the blob to the surface depends on the setpoint defined and the scan speeds depends on the rate.

This MatLab program was initially designed to simulate real time SICM scanning modes before starting the microscope construction. Posteriorly, it was adapted to judge pipette quality and it has proven as an important tool in this project.

Chapter 4

4. SICM Construction

The aim of this project is the design and construction of an SICM adapted to an inverted fluorescence microscope system for further applications in cell biology.

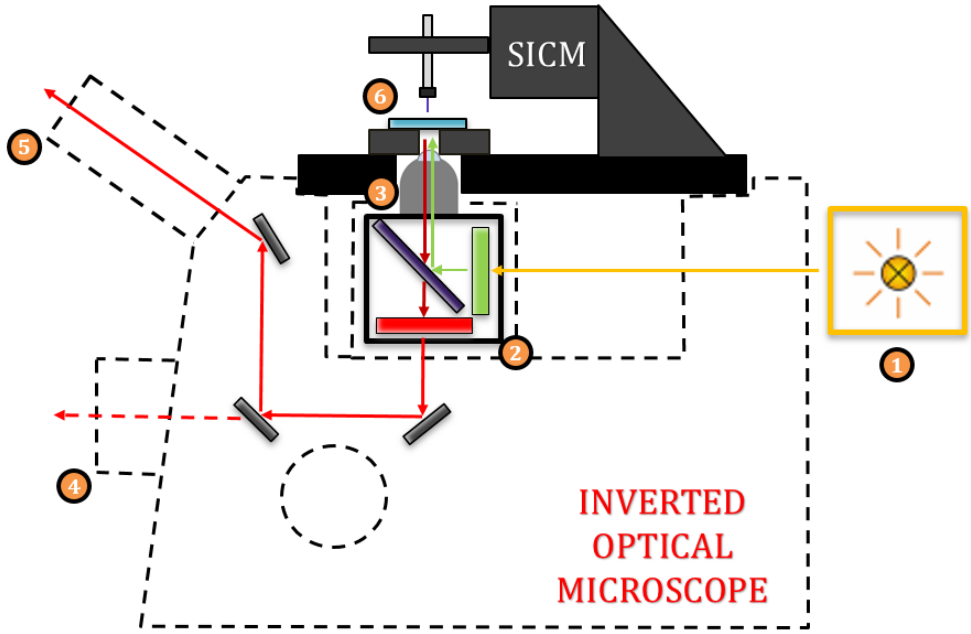

Figure 16 | SICM adapted to an inverted optical microscope. Here we illustrate a SICM with a sample placed on XY piezo stage (6), combined with fluorescence microscopy under the substrate surface. The basic elements of this fluorescence microscopy are a light source (1), the light is conducted to a Filter cube (Green excitation filter, red emission filter, dichroic mirror (2). The light excites the fluorophores, which emit light upon relaxation through the optical objective (3) and the image is captured in the Camera (4) and the user can take a look on the sample through the Eyepiece (5).

Fluorescent microscopy is a very powerful tool in optical microscopy for imaging the inside of cells. SICM is unsurpassed in its capability to resolve nanometer sized features on the surface of non-adherent living systems in physiological solution. A combination of these two techniques, *Figure 16*, will allow to get access to phenomena occurring on the inside of a cell characterizing cell surface features and achieving resolution far below the diffraction limit.

This chapter entails the design and construction of the SICM, using SolidWorks for individual piece design, CNC and leading machine for the microscope construction, further completed by manual assembly, obtaining a SICM combined with inverted optical microscope.

4.1. SICM Design

The first step in SICM construction, entails the design of the nanopipette holder (*Figure 17*), then the SICM main head (*Figure 18*) and SICM main platform (*Figure 19*). All the components were designed in SolidWorks for further machining using Alluminium Alloy and PMMA, since this materials are very easy to machine (drawings in *Appendix B1-B18*). Not all the parts shown in the drawings were designed, some of them were acquired from other setups or bought. All the pieces designed have the respective drawing reference in the Appendixes.

4.1.1. Nanopipette holder design

The pipette holder is represented in *Figure 17*, and consist on a long tube (3) (see *Appendix B2*), a top cork (2) (see *Appendix B1*) with a metallic adaptor (1) that connects the cable from the amplifier to the internal electrode through the tube into the nanopipette (6). The pipette is previously glued to a pipette adapter (4) (see *Appendix B3*) and tighten to the tube through the bottom cork (5) (see *Appendix B4*).

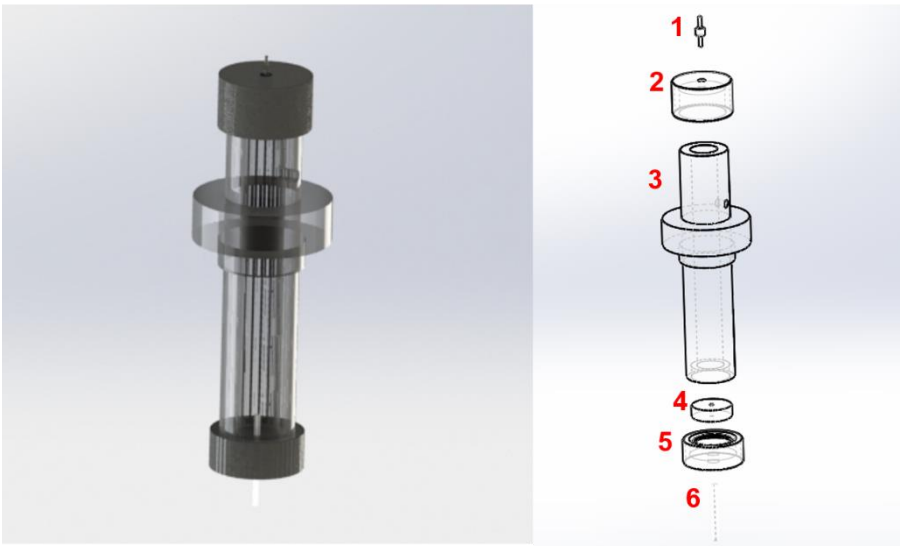

Figure 17 | Nanopipette holder designing. This element is composed by an electrode connector (1), a top cork (2), a pipette tube (3), a pipette adapter (4), a bottom cork (5) and the nanopipette (6).

4.1.2. SICM control support design

The nanopipette holder is placed into SICM control support in *Figure 18*. This support is composed by a Z piezo stage (2) linked to the nanopipette holder through an adapter (1) (see *Appendix B5*).

The piezo actuator is placed onto a plate (6) (see *Appendix B7*) connected using an adapter (3) (see *Appendix B6*). Then the plate is connected to the main head (4) through an adapter (5).

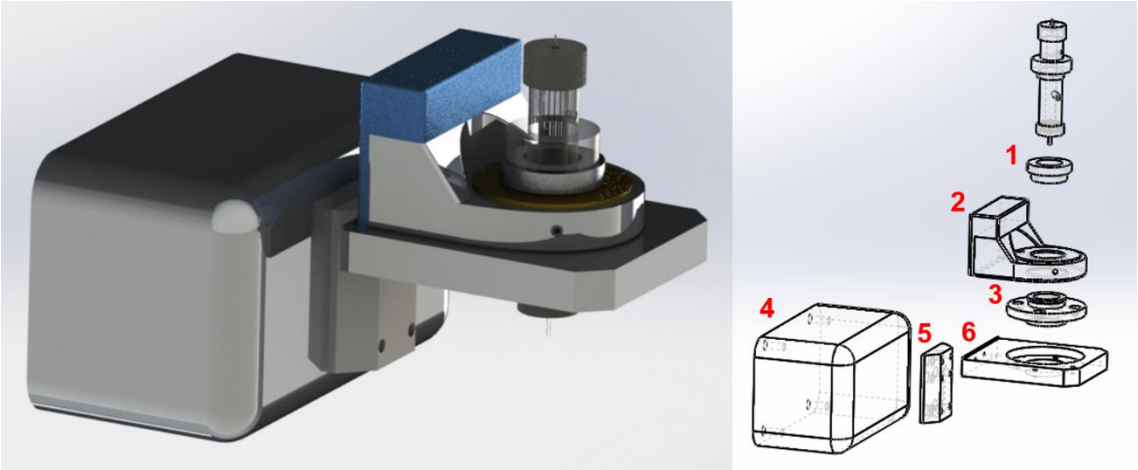

Figure 18 | SICM main head designing. This element is composed by a top Z piezo adapter (1), a Z piezo stage (2), a bottom Zpiezo adapter (3), a SICM Z controller head (4), a dovetail (5) and a Z piezo plate (6).

4.1.3. SICM platform design

The SICM control support, containing the nanopipette holder, is fixed in the main platform table (6) (see *Appendix B13*) by mean of 2 triangular supports (2) (see *Appendix B8 and B9*). The current amplifier (1) is placed in the main platform supported by a small piece (4) (see *Appendix B10*), and the XY stage (3) is supported by another plate (5) (see *Appendix B11*). Notice that the piezo stage (3), its support (5) and the table (6) have an aperture in order to adapt the optic objective. The table is adapted to the inverted optic microscope using four supports (see *Appendix B12, B14, B15, B16, B17 and B18*)

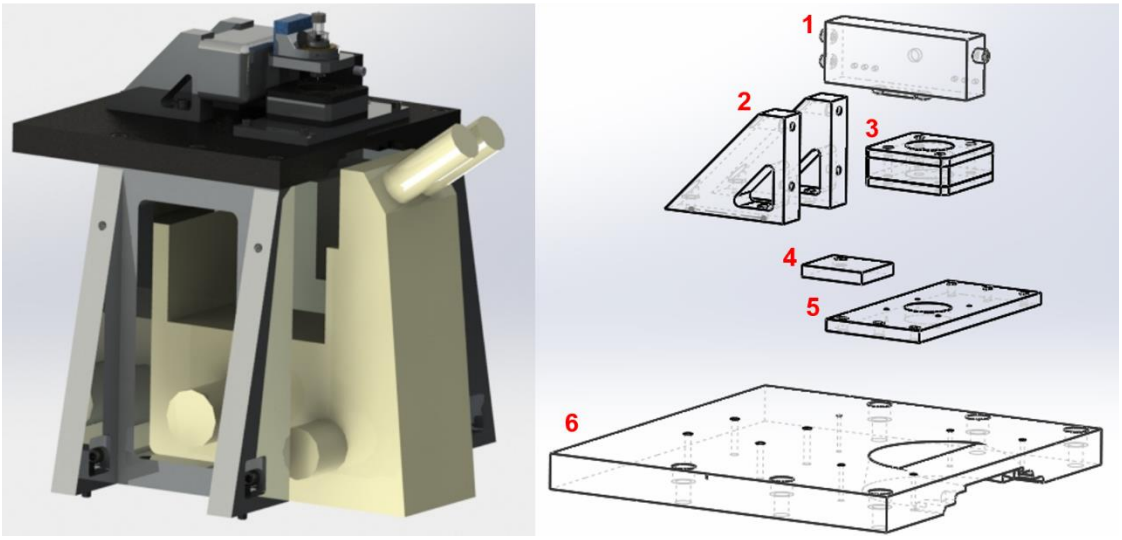

Figure 19 | SICM main platform designing. This element is composed by a current amplifier (1), SICM head binders (2), a XY piezo stage (3), an amplifier support (4), XY piezo support (5) and a Top sample table (6).

4.2. SICM Manufacturing and Assembly

After drawing SICM components, each piece was manufactured and assembled on the nanopipette holder (*Figure 20*), then the SICM main head (*Figure 21*) and SICM main platform (*Figure 23*). Then they were assembled and mounted in combination with inverted optical microscope, obtaining the final SICM setup (*Figure 27*). All the components were machined using a CNC mill and a CNC lathe.

4.2.1. Nanopipette holder manufacture

The pipette holder constructed is shown in *Figure 20* and consists on a long tube (3), bottom cork (5) and a top cork (1/2) connected to a signal cable from the amplifier. The internal electrode goes through the tube into the nanopipette and the external electrode is positioned outside. The pipette adapter (4) and all the other objects composing the holder are made with PMMA and the corks are covered with rough rubber to facilitate the twist.

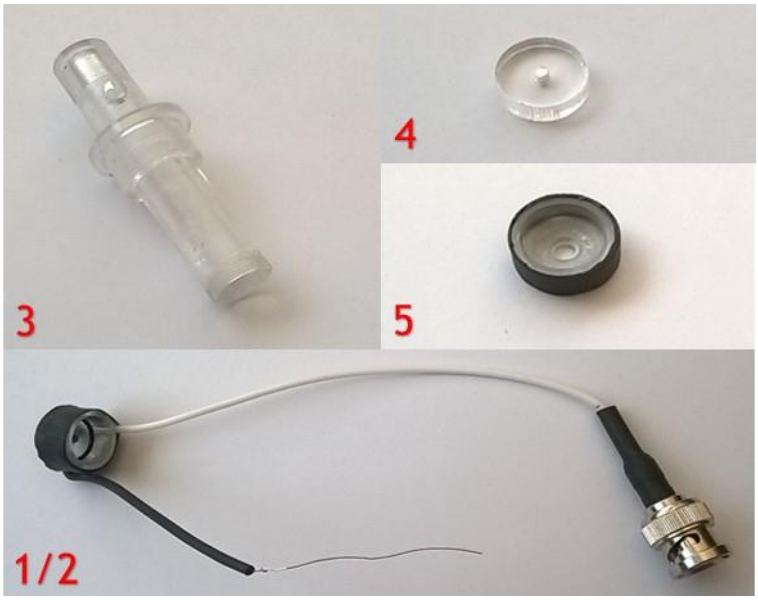

Figure 20 | Nanopipette holder manufacturing. This element is composed by a PMMA pipette tube (3), a PMMA pipette adapter (4), a PMMA bottom cork (5) and a PMMA top cork (1/2).

4.2.2. SICM control support construction

The main function of this SICM element is to support Z-axis Piezo Actuator MIPOS 100, in *Figure 21,* linked to the nanopipette holder through an adapter (1). The piezo actuator is placed onto a plate (6) connected by mean of an adapter (2). Then the plate is connected to the main head (4) through a dovetail (5). All the manufactured pieces here presented are made of Aluminum 6082-T6 as material.

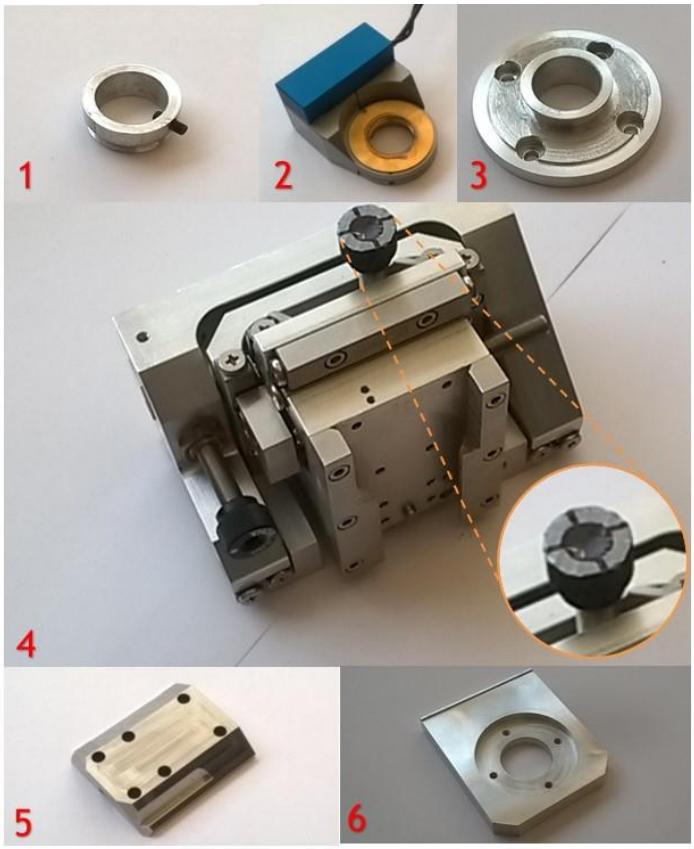

Figure 21 | SICM main head manufacturing. This element is composed by a top Z piezo adapter (1), a Z piezo stage (2), a bottom Zpiezo adapter (3), a SICM Z controller head (4), a dovetail (5) and a Z piezo plate (6).

The function of the main head in *Figure 21A*, is the displacement in Z range of the nanopipette, since the actuation range of the Z piezo is 100µm. It means that the probe is approached towards the surface manually, using the screw highlighting in (4). This thread pitch is about 350µm, so we marked the screw head dividing the pitch distance by four. Then we are approaching the probe manually with a step around 80µm. This main head, from *Santa Barbara Imaging LLC*, is typically used in AFM setups and was adapted to operate on SICM.

Then the pipette holder is assembled to the main head as seen in *Figure 2*1. At this point, we have a functional SICM, although we have to adapt it to an inverted optical microscope, so further support and adaption structures are required.

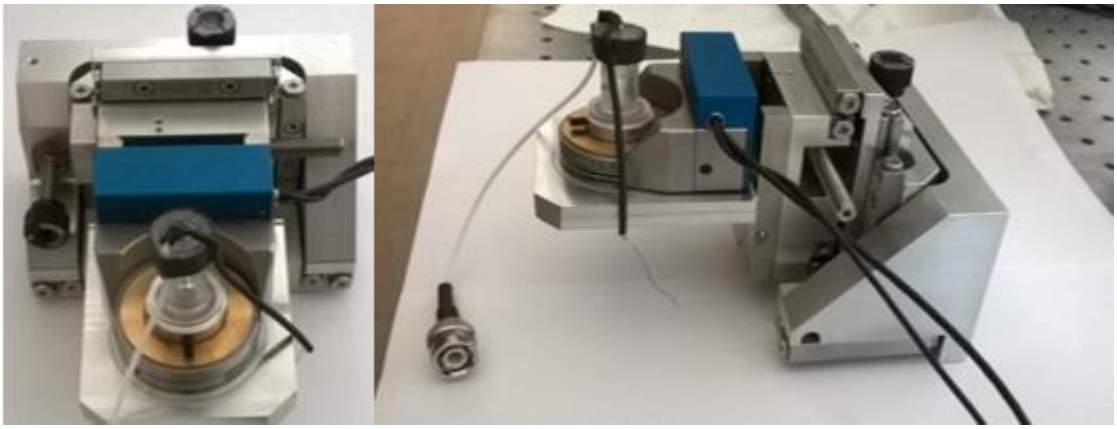

Figure 22 | Assembly of the pipette holder and the main head. Here is an image of the Assembly of the pipette holder and the main head.

4.2.3. SICM platform construction

To read the signal, a current amplifier DLPCA-200 (*Figure 23.1*) is used, placed in the main platform supported by a small piece (4). The XY stage XY-axis Piezo Actuator TRITOR (3(a)), supported by a plate (6), is used to move in XY axis, the specimen in the sample content (3(b)).

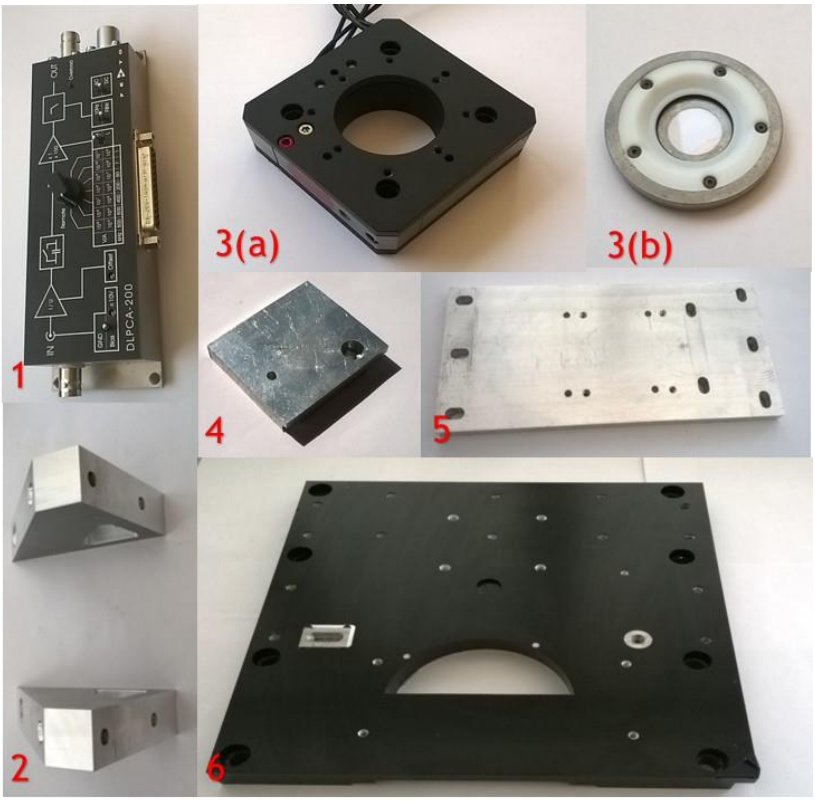

Figure 23| SICM main platform manufacturing. This element is composed by a current amplifier (1), SICM head binders (2), a XY piezo stage (3(a)), a sample content (3(b)), an amplifier support (4), XY piezo plate (5) and a Top sample table (6).

Notice the XY stage support has no aperture, because we will not run experiments using fluorescence microscopy for now, since the XY actuator is too high. In the future, a new XY piezo that fits in our setup will be constructed from scratch. All the manufactured pieces presented here are made with using Aluminum 6082-T6.

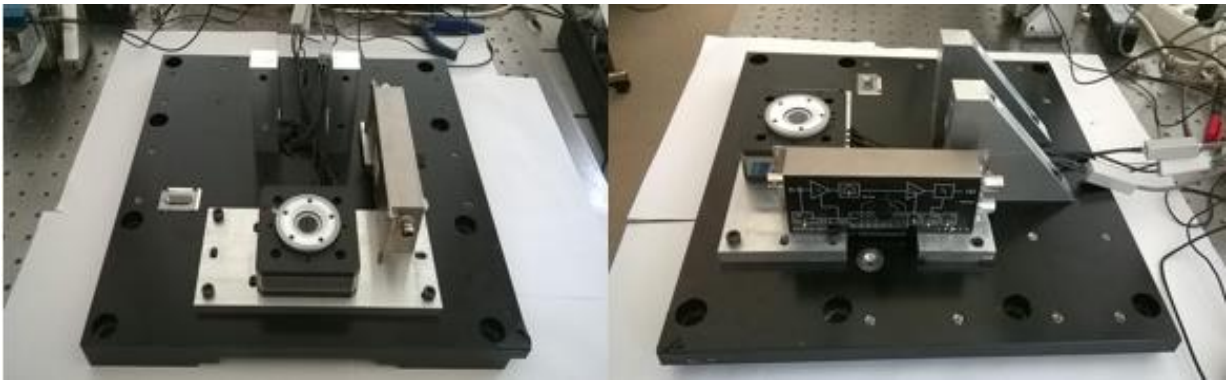

Figure 24 | Assembly of the adapting table. Here is an image of the Assembly of the table that adapts SICM to the inverted optic microscope.

The SICM control support containing the nanopipette holder is placed in the main platform table (*Figure 24*), once assembled all the table components as seen in *Figure 24*. After that, the SICM is ready to be adapted to an inverted optical microscope.

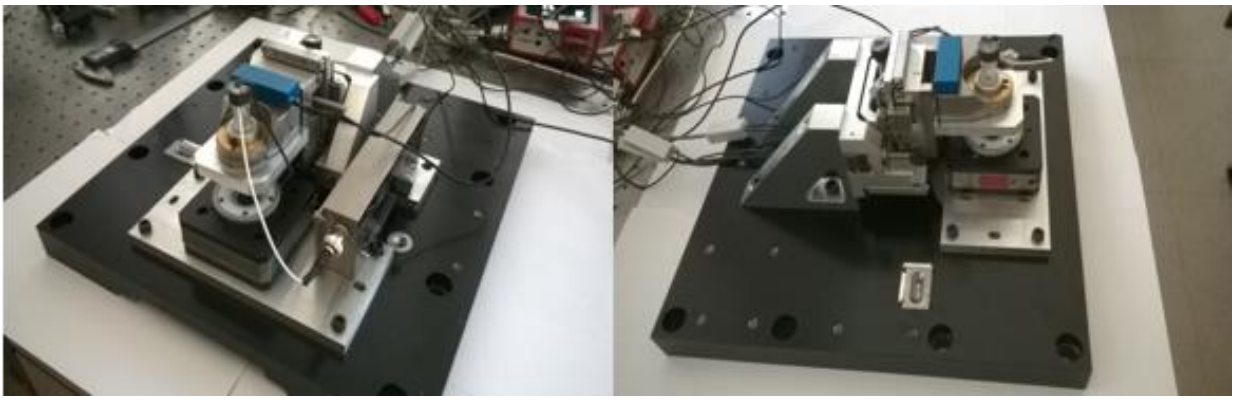

Figure 25 | Assembly of the pipette holder, the main head and table. Here is an image of the Assembly of the pipette holder, the main head and the table.

4.2.4. SICM final setup assembly

The inverted optical microscope adapted is an Axiovert 135, enclosed by four triangular pads supported by metallic panels in order to fit the SICM (*Figure 26*).

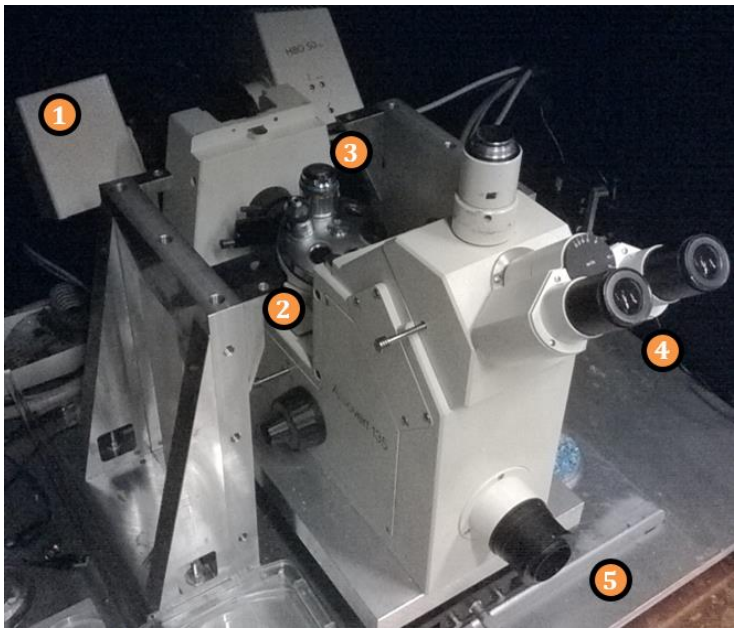

Figure 26 | Inverted optical microscope. Here is our inverted optical microscope. The basic elements of this fluorescence microscopy are the light source (1), the light is conducted to a Filter cube (2), then the filtered light wave excites the specimen through the optical objective (3) and an image is captured at Eyepiece (4) and Camera (5).

After assembling the nanopipette holder, control support head and the table, SICM can be adapted to the optical microscope, as seen in figure bellow.

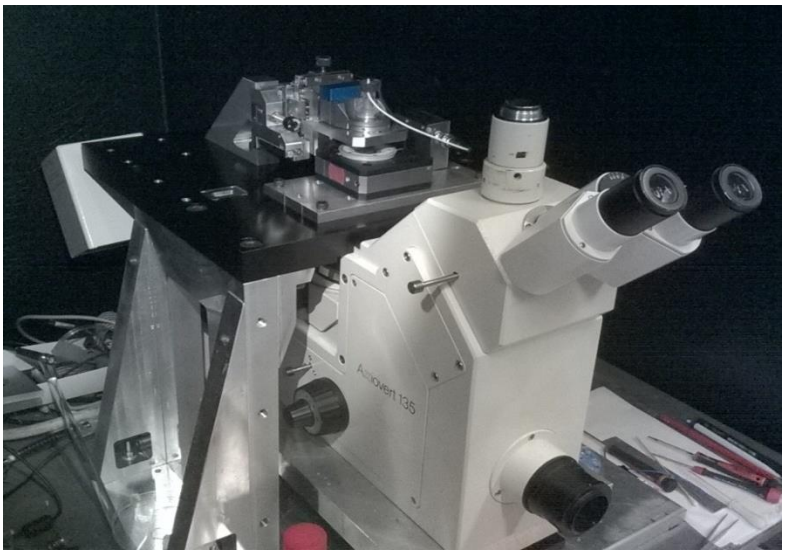

Figure 27 | Combined SICM setup. Here is the final SICM setup, after combination of SICM table with the inverted optical microscope.

Finally, the combined setup is placed onto a hanging table in order to isolate the system from vibrations and mechanical noise. The setup must be enclosed in a faraday cage to reduce EMI contamination.

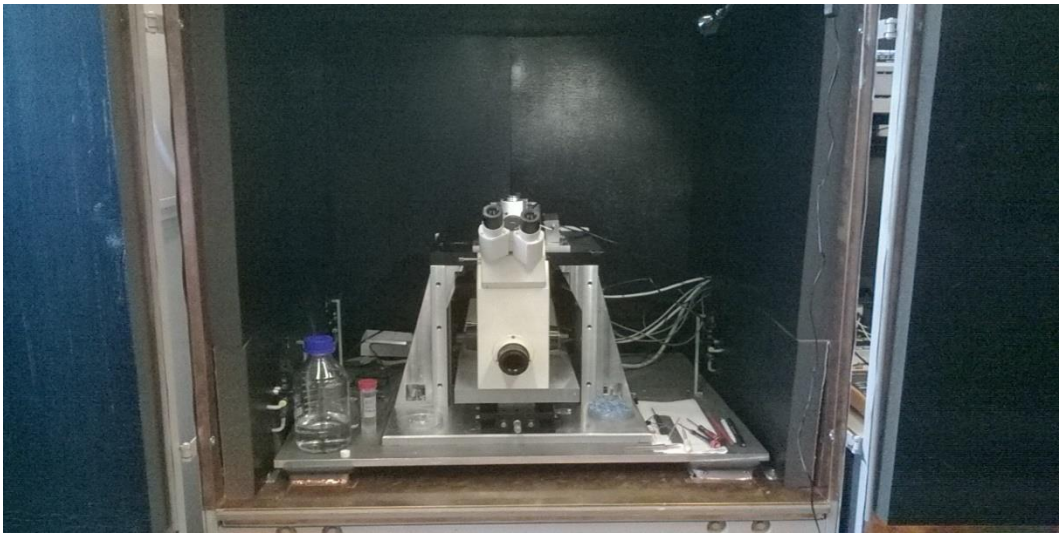

Figure 28 | SICM isolation cage. SICM setup is placed onto a hanging table to avoid mechanical vibrations, inside of a Faraday cage to avoid electromagnetic noise.

At this point, the setup is functional and it is ready for applications. However, first we have to make sure we have good pipettes as probe, and the electrodynamics system is stable. This matters will be explained in the next chapter.

Chapter 5

5. Electrochemical system

This chapter entails all the electrodynamics characterization of the setup. Starting by the electrode manufacturing and its relation with problems in reading the signal. Then, it shows different batches of nanopittes produced, with repercussion on the magnitude of the reading signal. Afterwards, approach curves are obtained with that pipettes.

5.1. Electrodes

The principle of SICM is that an ionic flows through the pipette and decreases when the probe approaches the surface. To generate the current, a voltage is applied between two electrodes, one of which is in the glass pipette, and the other in the bulk solution (*Figure 29B*).

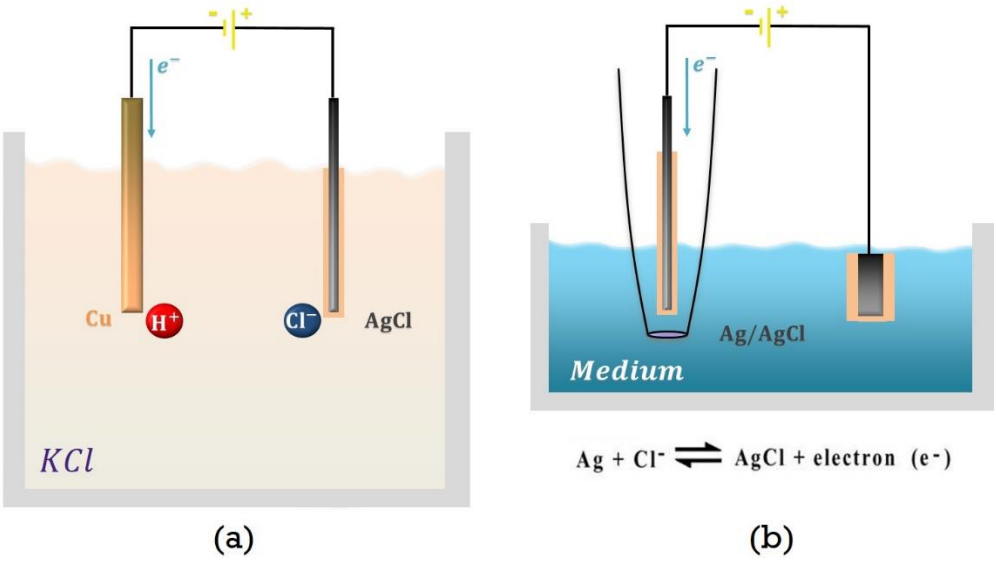

Figure 29 | SICM electrodes. Here we show AgCl electrodes manufacturing in KCl solution (A) and tipical SICM setup in KCl solution, where one of Ag/AgCl electrodes is in the glass pipette and the other in the bulk solution (B). In this SICM setup, Ag/AgCl electrodes are produced using Ag wire of 0.25mm (see *Appendix C*). The silver wire is cleaned with a fine grade emery paper and rinsed with distilled water. Then, we immerge the silver wire (as an anode) and the copper wire (as a cathode) into 0.1 M KCl (see *Figure 29A*) and we apply 10 mA/cm^2 during 5 min. After the electrolysis, we rinse the electrode with pure water and it is stored in 1M KCl.

In this SICM setup, we produced our own Ag/AgCl electrodes. One of the electrodes produced is shown in the figure bellow.

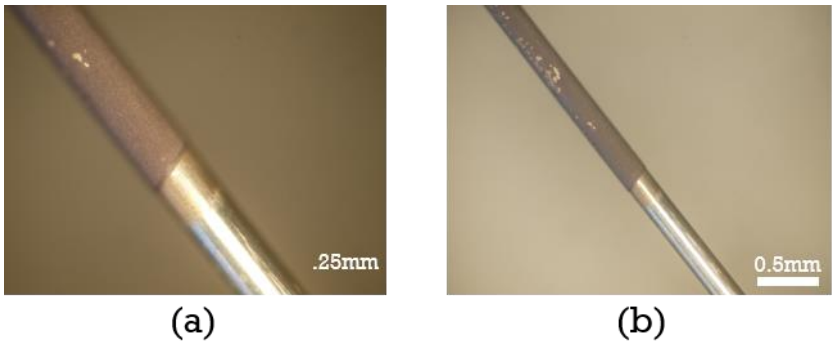

Figure 30 | SICM electrodes manufacturing. Here we show the Cl deposited onto the silver surface at different scale bars, 0.25mm (A) and 0.5mm (B).

The step of electrodes production in SICM setups is critical, with a crucial role in current stability. Irregularities on the deposited surface layer, as seen in *Figure 30* , usually originates drifts in the electrode potential, leading to difficulties during the measurements. Ideally, the deposited chloride layer should be perfectly uniform. Another problem is electrode damaging when the electrode is placed into the pipette due to the sharp circular edge scratching the electrode surface.

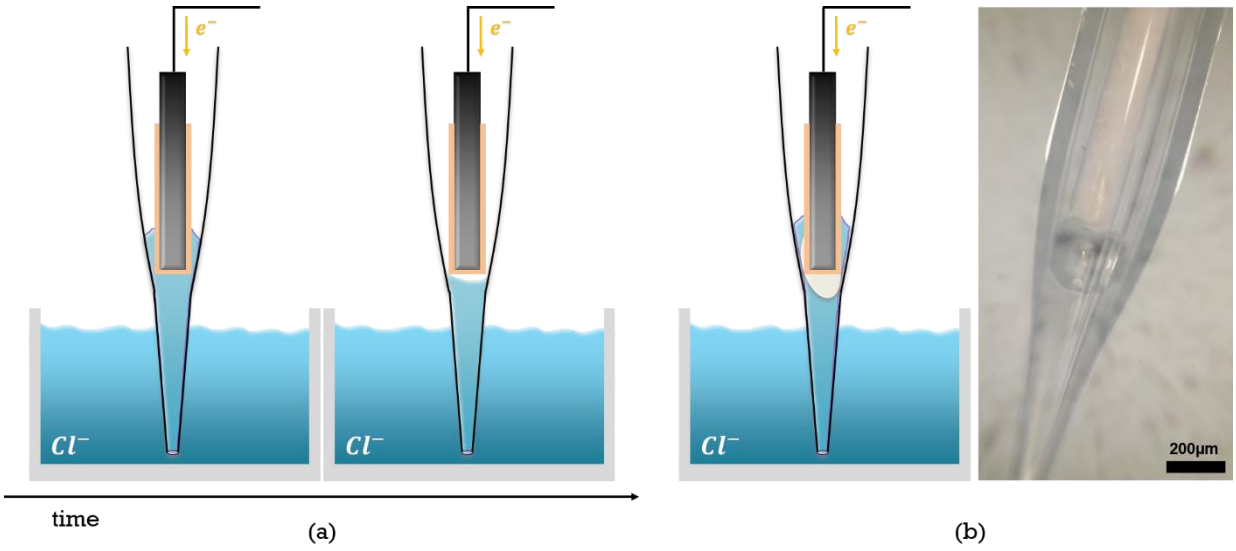

Figure 31 | Electrode-Electrolyte contact interface inside of the pipette. Here we show liquid evaporation over time (A) and bubble formation (B), leading to current drifts.

In addition, a high potential difference between the electrodes and the bulk solution often creates air bubbles produced by oxygen and hydrogen, as shown in *Figure 31B*. Another concern is liquid evaporation over time, leading to current drifts when the layer between electrodes and the electrolyte is too thin, as seen in *Figure 31A*.

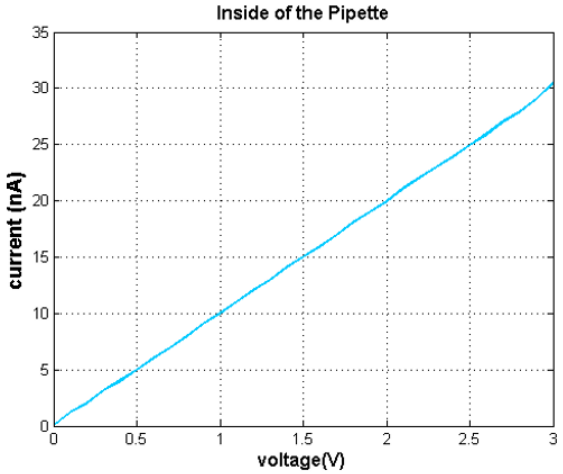

Figure 32 | Electrodes characterization. Here we show the response in current in function of the voltage applied, tested in free bulk solution of 0.1 M HCl, and inside of the nanopipette.

The current in function of voltage shows a perfectly linear response under the range of 3V, *Figure 32*, approving just one reaction dependence at the electrodes surface. In order to ensure measurements under the electrolyze point of water, a scanning a bias voltage under 1V is be used.

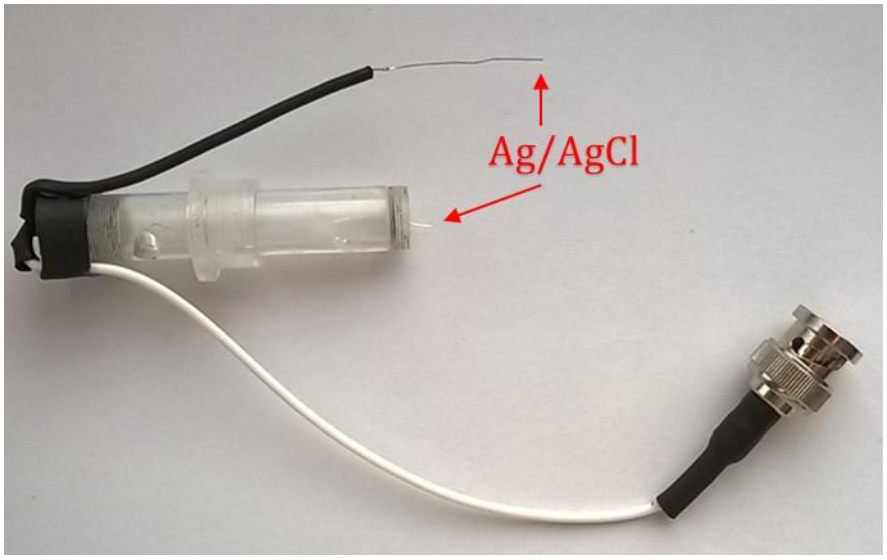

Figure 33 | Electrodes placed in nanopipette holder. Here we show the electrodes one of which is in the glass pipette, and the other in the bulk solution. There are no a specific position for the two electrodes.

One of the electrodes connects the ground and the other one to the connector in the top cork, through the tube into the nanopipette. The current flows into the two electrodes, *Figure 33*, through the white cable connected to the current amplifier. This current comes from the current amplifier DLPCA-200 (*Figure 23E*), also capable of applying a bias voltage in the range of 0-10V).

5.2. Nanopipettes manufacturing

The pipettes have a critical impact in SICM measurements, since they are directly related with the probe sensitivity and scanning resolution. As a result, pipette manufacturing has an important role, in order to obtain proper pipette inner radius size.

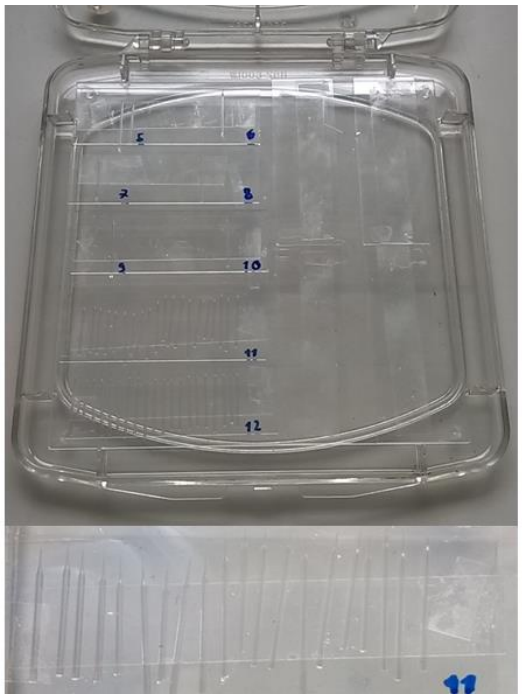

Figure 34 | Storing Pipettes. Pipettes generated with different fabrication parameters in different batches are stored and identified by different numbers.

Pipettes were manufactured in different batches and stored as seen in *Figure 34*. Three kind of capillaries were used, quartz glass capillaries with 0.3 mm of inner diameter, borosilicate glass with 0.5 mm of inner diameter and borosilicate glass with 0.6 mm of inner diameter (see *Appendix D*).

In order to find the ideal nanopipette, several batches with different fabrication parameters were produced by mean of a CO2 laser machine sutter p2000 [58]. *Table 3* shows the characterization of the nanopipettes produced.

For some pipettes, no current was detected, which means the pipettes were sealed. For other pipettes, an approach curve was not successfully achieved, even reading a current, which means the tip opening is not perpendicular to the vertical axis of the pipette. The pipettes performing the best results are from the batch 12, were 98% of good quality approach curves have been obtained and high resistance corresponding to small inner radius has been read.

Table 3 | Pipettes characterization for several batches.

Batch	Material	Heat	Fil	Vel	Del	Pull	N	R (MΩ)	Bad App (%)	Good App (%)	Predicted inner radius
1	Quartz	650	0	20	128	0	31	0.9	13	0	2.2µm
2	Quartz	650	0	20	128	200	22	0.7	18	0	2.8µm
3	Borosil 0.5mm	295	4	35	250	150	15	0.7	66	0	2.8µm
4	Borosil 0.6mm	295	4	35	250	150	9	0.5	66	0	3.9µm
5	Borosil 0.5mm	295	4	35	200	150	7	2.7	0	0	720nm
6	Borosil 0.5mm	380	4	35	250	150	8	0.7	0	0	720nm
7	Borosil 0.5mm	380	4	30	250	150	5	1.5	20	0	1.3µm
8	Borosil 0.5mm	380	4	30	280	150	6	0.4	0	0	4.9µm
9	Borosil 0.5mm	380	4	40	200	150	4	3	0	0	648nm
10	Borosil 0.5mm	380	3	30	250	150	5	0.5	20	0	3.9µm
11	Borosil 0.5mm	320	4	40	235	150	7	3.4	29	71	572nm
12	Borosil 0.5mm	325	4	35	235	150	7	10.2	50	98	191nm
13	Borosil 0.5mm	350	4	35	235	150	13	1.3	30	0	1.5µm

A certain amount of pipettes N from each batch were tested, the maximum resistance R measured, an approach curve was performed and the inner radius predicted regarding *Equation 8*, applying a bias voltage of 1V, assuming a teta angle of 10 degrees and a conductance of 5mS. The HEAT parameter specifies the output power of the laser, and consequently the amount of energy supplied to the glass. FIL specifies the scanning pattern of the laser beam that is used to supply HEAT to the glass. The VEL specifies the velocity at which the puller bar must be moved before the hard pull is executed. The DEL controls the timing of the start of the hard pull relative to the deactivation of the laser and finally the PULL controls the force of the hard pull.

The best pipettes from batch 12 have also been characterized by SEM and TEM microscopy in *Figure 35*. The inner radius of the pipette match pretty well with pipettes seen in literature, *35A*. In *Figure 35B* it is possible to see the pipette walls profile (the tip looks blurred due optical distortion). However, pipette manufacturing using laser machine does not always work well. Even within the same batch, some pipette are sealed as seen in *Figure 35D* or its aperture is not well shaped, because there is no reproducibility in this kind laser based machine.

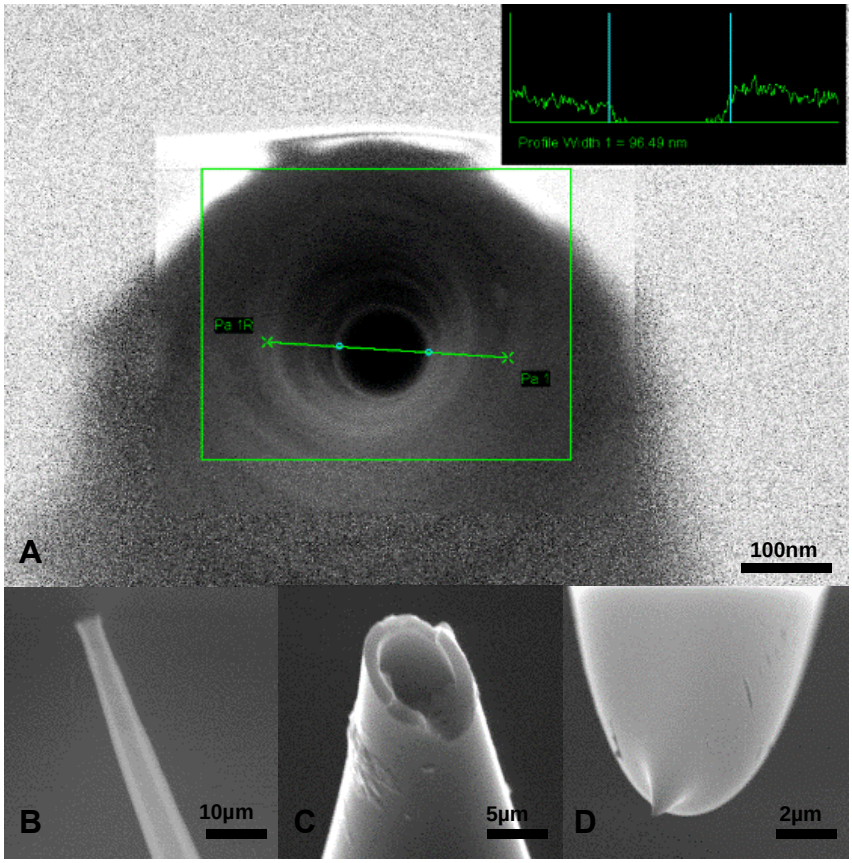

Figure 35 | Pipette tip characterization. Here is possible to see the inner radius of a really good pipette in A by SEM, the pipette wall in B by TEM, a deform tip opening in C by SEM, and a sealed pipette in D by SEM.

After manufacturing, the pipette must be assembled in the adapter before starting a new measurement (*Figure 36C*). To do that, the pipette is glued in the adapter and incorporated in a Teflon mold (*Figure 36B*). Then the pipette is filled with a syringe (*Figure 36D*); If some bubbles remain inside of the pipette, we should take them out with a vacuum pump or a lighter.

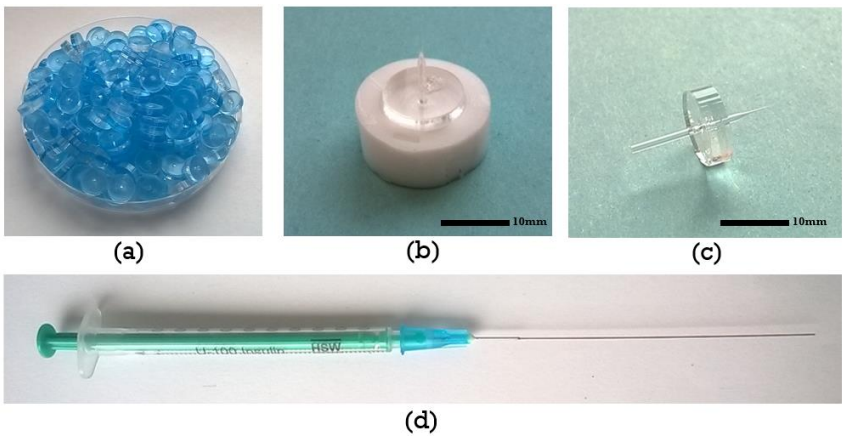

Figure 36 | Pipette setting-up. Here we show pipette adapters (A), the mold for pipette gluing (B), pipette sealed in the adapter (C) and a syringe to fill pipettes (D).

5.3. Approach Curves characterization

After mounting the microscope and producing the probes, approach curves had been characterized. An Approach curve is the basic mechanism to detect the surface and scan a sample, so that its characterization is crucial to generate a real and clean image. They are extremely related with the pipette opening characteristics.

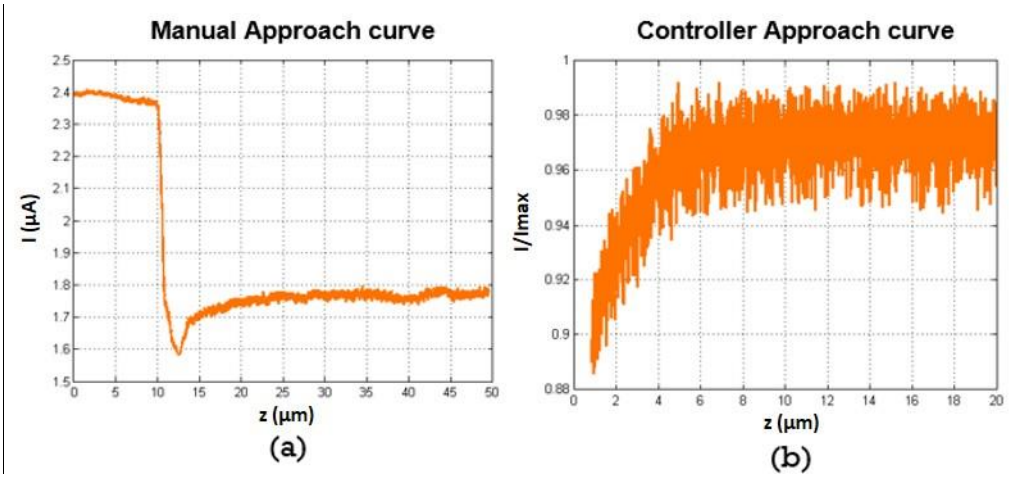

Figure 37 | Approach curves. Here we show a manual approach curve measured on the oscilloscope (A), and an approach curve achieved with Labview controller (B).

In first place, some approach curves were produced manually, screwing down the main head very slowly *(Figure 21a*) and reading the current in an oscilloscope with a sampling rate of 1MHz, as seen in figure above (A). Because we are doing it manually and we don't have good sensitivity and the pipette breaks. Since the current rises instantaneously after breaking, the approach curve is captured trough a trigger on oscilloscope that detects an increasing in current.

Afterwards, once we make sure we can get approach curves using the pipette manufactured, we produced approach curves by mean of a Labview controller. A simple program to approach the probe with a step of 1nm over a range of 100µm was developed, recording the current in each step, as shown in *Figure 37b*.

For more accurate analizes of curve data, it was low pass filtered at 10Hz and then characterized, allowing the distinction between good and bad pipettes, *Figure 38*. All the pipettes manufactured in *Table 3* were tested and its approach curves were characterized as good, bad, and no approach curve.

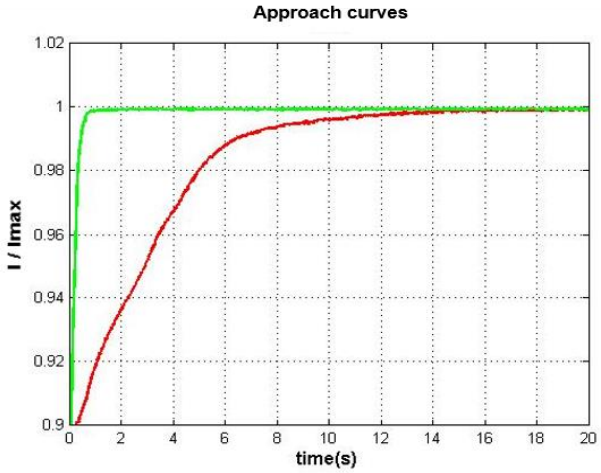

Figure 38 | Approach curves characterization. Here we compare good quality approach curves (green) with bad quality approach curves (red).

On *Figure 38*, a good approach curve and a bad one are overlapped and compared in a range of 20µm. We define a good approach curve when the current starts decreasing under 1um from the surface (delimiting a set point of 90% in maximum current). On other hand, we define a bad approach curve when the current start decreasing above 1um from the surface (delimiting a setpoint of 90% in maximum current). However, sometimes no approach curve is achieved (or a distorted one), because the pipette shape is not good, so that the pipette breaks very easily.

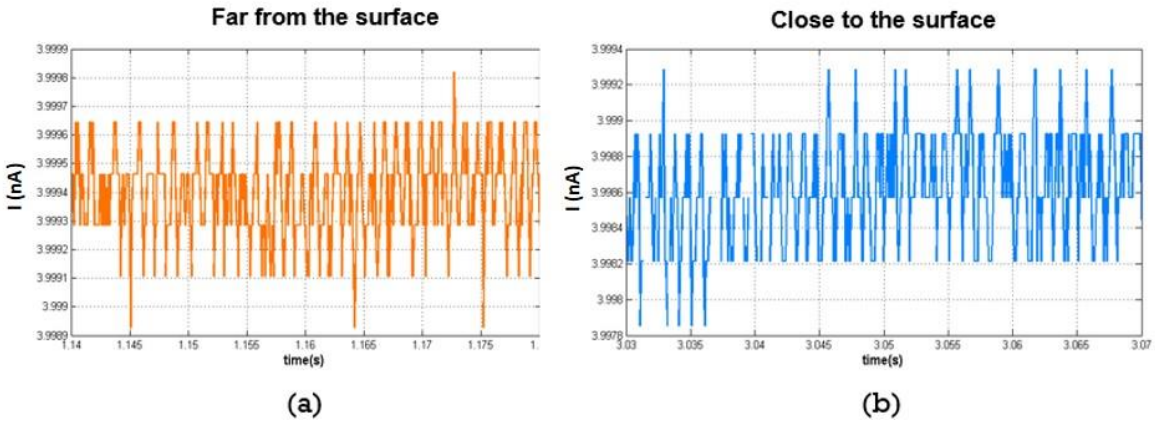

Figure 39 | System Noise. Here we show pipette adapters (A), the mold for pipette gluing (B), pipette sealed in the adapter (C) and a syringe to fill pipettes (D).

After signal filtering, the noise measured far from the surface is very satisfactory (*Figure 39a*). Once close to the surface the noise increases and once in a while distortions happens due to mechanical noise (*Figure 39b*).

In *Figure 40* we show a typical approach curve, when the pipette approaches to the surface at 1 Hz. The probe moves step by step (generally 1nm every step) and the current is read until reach a defined setpoint, in this case 98% of the maximum current. The pipette is moved back and the maximum current recorded for every ramp.

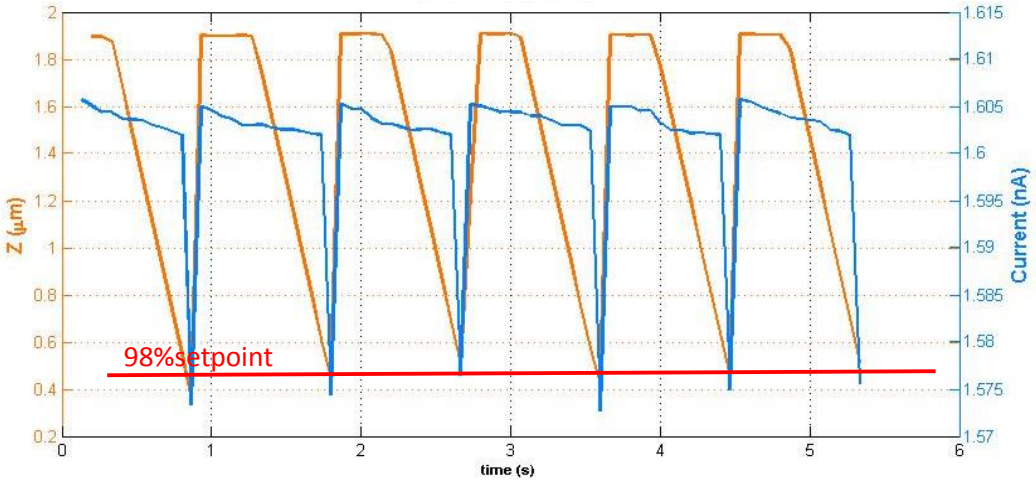

Figure 40 | Z piezo displacement Vs Current. Here we present the current values (blue) in function of Z piezo displacement (orange) during SICM scanning in Hopping mode.

Nevertheless, some drifts in current are usual during the measurement, leading to inaccurate values and distorted approach curves. In *Figure 41* (yellow plots) we show abrupt drifts in current readings before scanning and during scanning in the orange plots bellow, caused mainly by electrochemically problems described in *Chapter 5*.

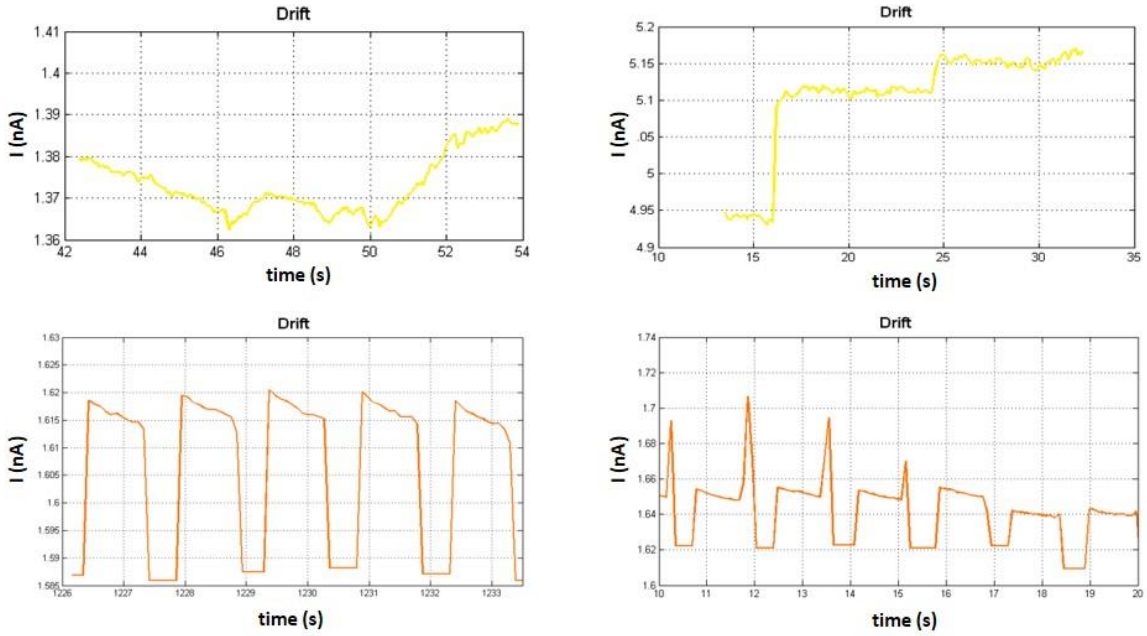

Figure 41 | Current Drift. Here we show drifts in current during scanning (orange) and before scanning with the pipette fixed in Z range (yellow).

Chapter 6

6. Control System

6.1. Main Control System

The SICM scanning is controlled by an ordinary computer communicating via ethernet interface with the field programmable gated array (FPGA) incorporated in the NI COMPACT C-RIO Real-Time Controller running LabVIEW Real-Time for deterministic control.

The signal from ion current readings is amplified using a DLPCA-200 amplifier, with a trans impedance gain from 10^6 to 10^{10} V/A and an adjustable bias voltage in the range of 200mV-1V *Figure 42*. An analog filter SRS SIM965 with 10 mV resolution and 1 MHz bandwidth is used to filter the signal, by implementing a low pass filter at 10Hz.

An accurate 16-bit 1MHz NI 9223 ADC MODULE was used for analog to digital conversion and input the signal in the FPGA. A fast 16-bit 100kHz NI 9263 DAC MODULE controls the Z-position of the Z-axis piezo actuator and XY-position of the XY-axis piezo stage.

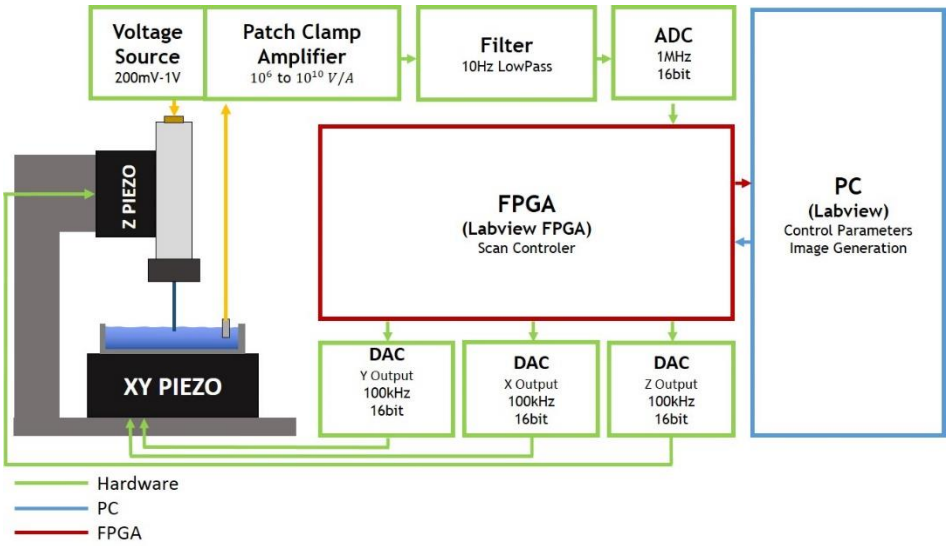

Figure 42 | SICM control system. Here we show how the SICM microscope communicates with the hardware components, computer and FPGA.

The FPGA drives all input and output operation and complex data analyses and image processing runs on the PC. The PC is used to set the scan parameters and to store the ion current and the pipette *z*-position every pixel read on FPGA, generating an image in real time, line by line.

6.2. Piezoelectric stages

The image generated is particularly dependent on the appropriate acting of XY-axis piezo stage controlling X and Y position, and also the Z-axis piezo actuator which controls the probe position. The XY-axis Piezo Actuator TRITOR102SG with a free central hole for inverted optical microscopy adaptation, 80 µm XY range, sensitivity of 0.125 V/µm, output monitor of -0.004V to 9.998V in X axis and 0.007V to 10.005V in Y axis, is driven by a Digital system d-Drive 20bit resolution and sampling rate of 50 kSPS. The Z-axis Piezo Actuator MIPOS100, 100 µm adjustment range, sensitivity of 0.0944 V/µm and 0.007V to 10.005V output monitor, is driven by a 12V40 OEM Controller.

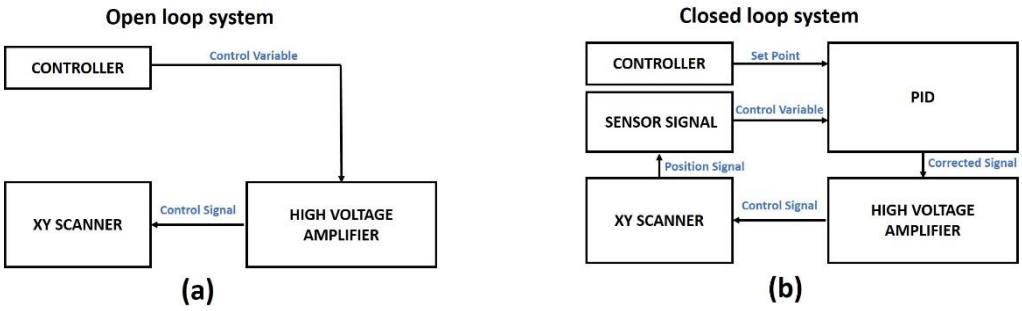

Figure 43 | XY stage controller. Schematic of an open loop system (a) and close loop system (b), exemplified by an image.

Instead of driving the piezo actuator directly with the controller, open loop system illustrated in *Figure 43a*, we can drive it using a closed system represented in *Figure 43b*, avoiding displacement hysteresis, drift, creep and other non-linarites. In the closed loop system a PID reads the real position from a sensor and correct the signal to the setpoint coming from the controller, correcting non-linarites in real-time, as seen in *Figure 43b*. The input voltage should be smooth (*Figure 44a*). At the end, four images are generated corresponding to trace and retrace of the piezo movement, as shown in *Figure 44b*, avoiding creep in XY piezo displacement and getting more information about the sample.

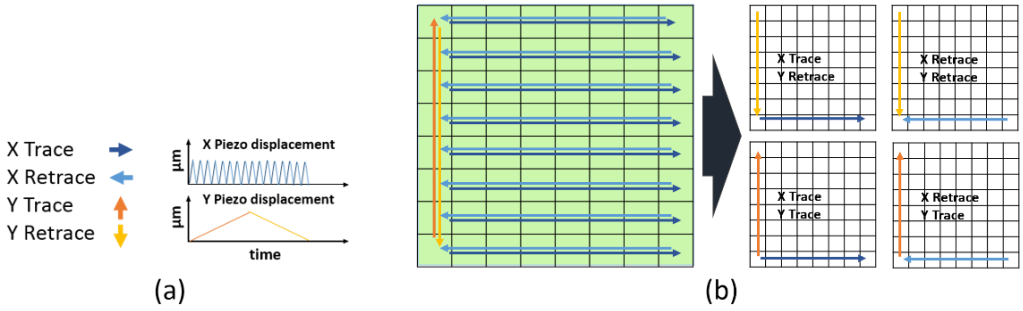

Figure 44 | XY stage displacement. Here we show XY-axis displacement, snd the respective four images gererated, XTraceYTrace, XRetraceYTrace, XTraceYRetrace, XRetraceYRetrace, printed line by line on the real time software.

6.3. Acquisition Software

6.3.1. Real time interface

The acquisition software was implemented in LabVIEW Real time based programming and compiled in the computer, the code can be seen in *Appendix F*. *Figure 45* shows the user interface developed (see *Appendix E*), which can be divided in the following functionalities:

- Approach to the surface
- Approach curve characterization
- DC Mode Scanning
- Hopping Mode scanning
- Data Processing

Figure 45 | Labview Real-time user interface. The program is mainly divided in the approaching to the surface (left), surface scanning (center), and image processing (right).

6.3.1a. Approach to the surface

The first step, before start scanning is the approach to the surface, manually and automatically. By clicking in the hopping approach bottom (yellow bottom on top left) we approach to the surface automatically, covering a distance of 100µm. If a decreasing in current is not identified the user stop the hopping approach by clicking in the stop bottom (red bottom on top left) and we approach manually a distance of 80µm with the holder head. This process is repeated until the surface is reached.

In order to have an efficient approach the parameters should be set properly, the rate of approach ("Z Rate [µm]"), the displacement ("displacement step [µm]"), the Z piezo sensitivity ("Zpiezo Sense [V/µm]") and the setpoint ("Setpoint Voltage [mV]"). A vector of positions is created according the displacement step and the piezo sensitivity. Then, a *while* loop sends the position to the piezo through the FPGA at each turn (running at the approaching rate defined previously). In meanwhile the current is read and drawn in the Real time acquisition plot on top left in *Figure 45*, if current drops by the setpoint defined the loop is interrupted. The position ("position [µm]") and the current signal ("signal [V]") are shown on the screen in real time and the position where the setpoint is reached ("Setpoint postion [µm]") is shown after each approach curve (theoretically should be the same for the same position if the system is well shielded from the noise and the setpoint chosen is appropriate for the pipette size). See the block diagram in *Appendix G* illustrating this algorithm execution in more detail.

6.3.1b. Approach curve characterization

In order to get more information about the system's noise and pipette quality, we can characterize an approach curve by fitting the curve with the polynomial model shown in *Equation 3*. We also can get access to the maximum current ("Imax [nA]") and setup resistance ("Setup R [MOhm]"). See the block diagram in *Appendix H* illustrating this algorithm execution in more detail.

6.3.1c. Scanning

For scanning, two operational modes are available, DC mode and Hopping mode (*Figure 45* on center up). First, the parameters, such as the setpoint ("I/Imax setpoint"), scan size ("Scan Size [µm]"), resolution in X-axis ("pixels") and in Y-axis ("lines") are set. Then, the user can chose the scanning mode in the separators and set the corresponding mode parameters, before start scanning.

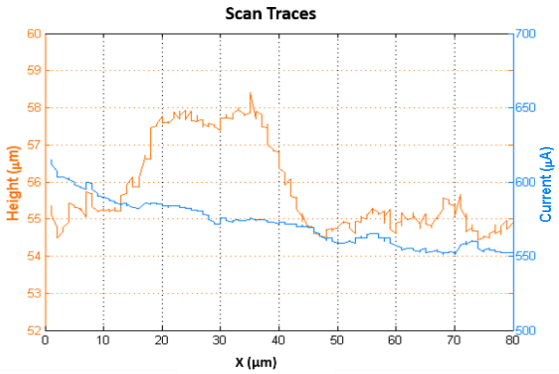

Figure 46 | Scan traces. Shows Height and current traces for each line.

During the scanning the height traces and the current readings (*Figure 46*) are shown in the software (*Figure 45 on top right*), and the respective trace and retrace images as well (*Figure 45 on center down*).

6.3.1d. Data Processing

After scanning, in order to calculate the correct topography for complex structures, the image can be reconstructed using a Gaussian function (*Figure 45 on right down*). An example of fitting performance is shown in the figure bellow. See the block diagram in *Appendix L* illustrating this algorithm execution in more detail.

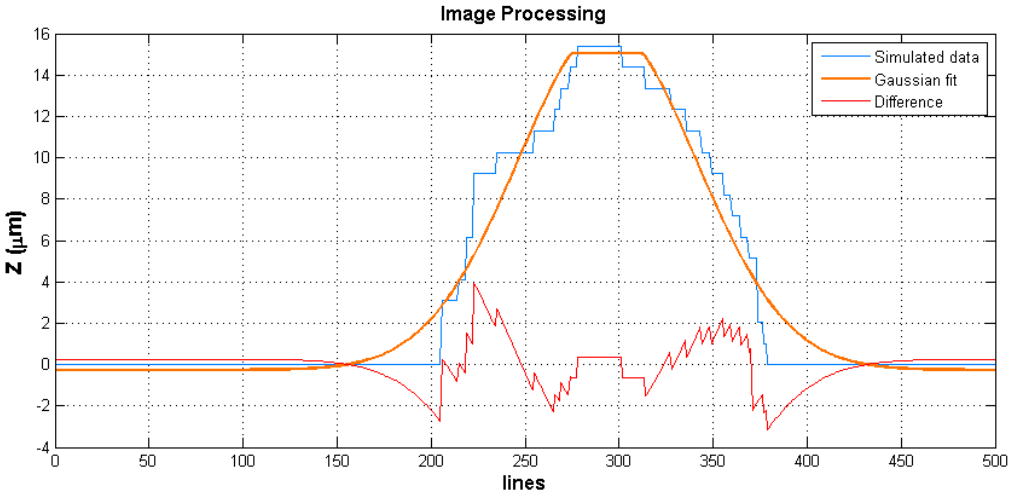

Figure 47 | Image reconstruction. A Gaussian fit (in orange) is implemented to a simulated line (in blue) representing the surface measured during the scanning.

6.3.2. FPGA interface

The FPGA was programmed using LabVIEW FPGA based programming (see *Figure 48* and *Appendix M*), the code can be seen in *Appendix N*. Technically the FPGA is a hidden part of the running program in lab view Real-time, however, because this is an experimental software developed from scratch. I have implemented a user interface to play with the division of time in each task inside of hopping algorithm, in order to improve the scanning performance.

Figure 48 shows internal parameters of the Approach function, DC mode, and Hopping mode. Relevant parameters for the performance improvement are the time delay to record the maximum current ("wait Imax [mSec]"), approaching rate ("wait Signal [mSec]"), and retract rate ("Retract step [µSec]"). Regarding the scanning performance in real time, the PID response for DC mode, Zpiezo Position and current signal is monitored in real time.

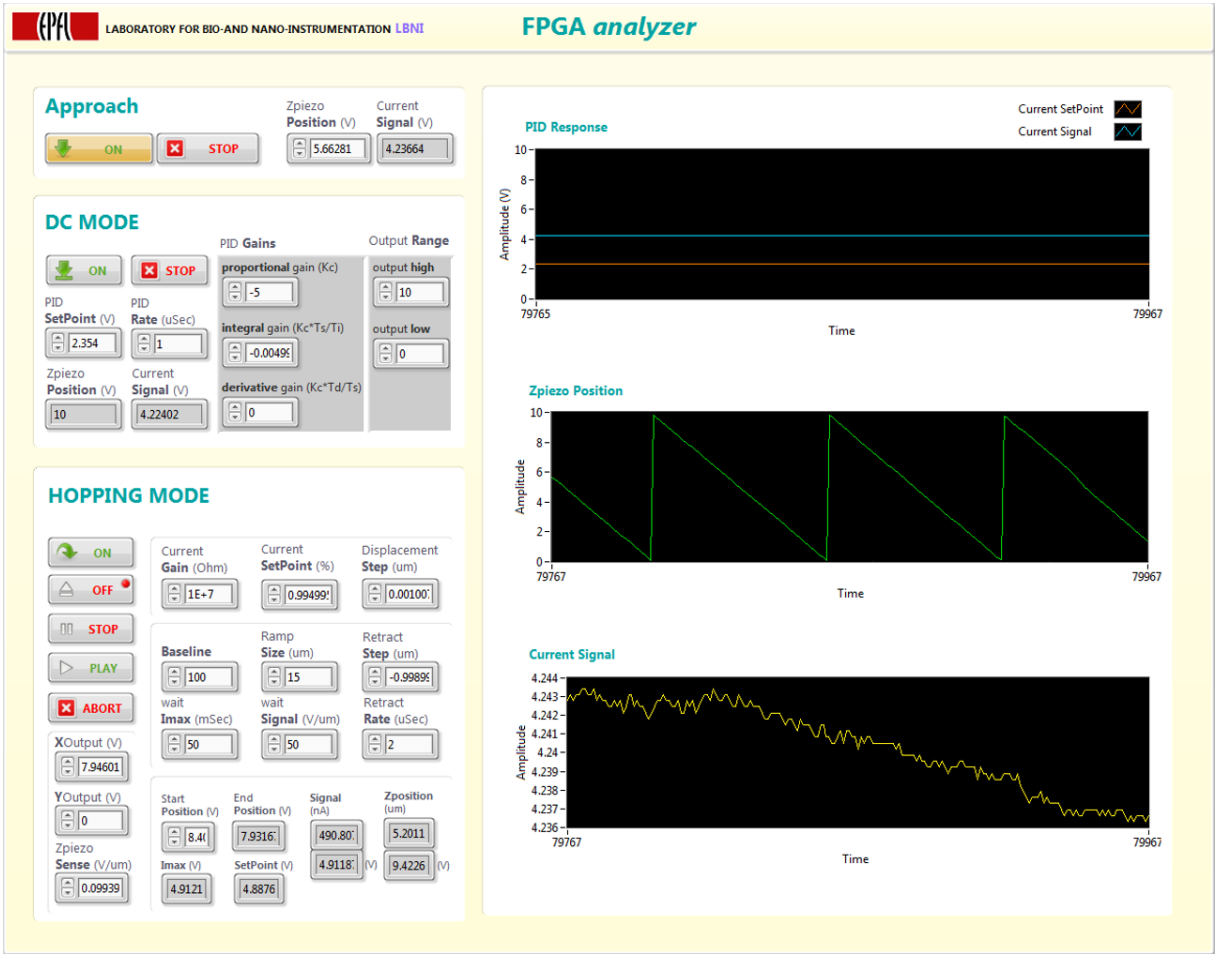

Figure 48 | Labview FPGA interface. Shows internal parameters of FPGA on left and signal recordings on right.

Chapter 7

7. Imaging Performance

7.1. DC Mode

7.1.1. Implementation

The easier mode to implement in SICM is the DC mode (constant distance mode), so to test our setup the DC mode was implemented in Labview real time, with a very simple user interface (see *Figure 45 on top center*). The user can set the gains of the PID and also adjust the thermal drift in real time as the DC mode is very prone to changes in current over time.

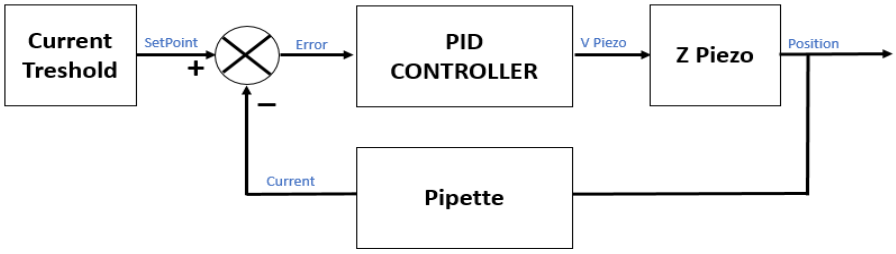

Figure 49 | Feedback controller. PID controller implemented in labview FPGA.

Basically, we have a PID controller implemented in the FPGA, which controls the pipette position loop accordingly with the current readings and the threshold defined (see DC mode fundaments details in *Chapter 2*). *Figure 49* shows the diagram of the negative feedback loop controller implemented. See the block diagram in *Appendix I*, illustrating this algorithm execution in more detail.

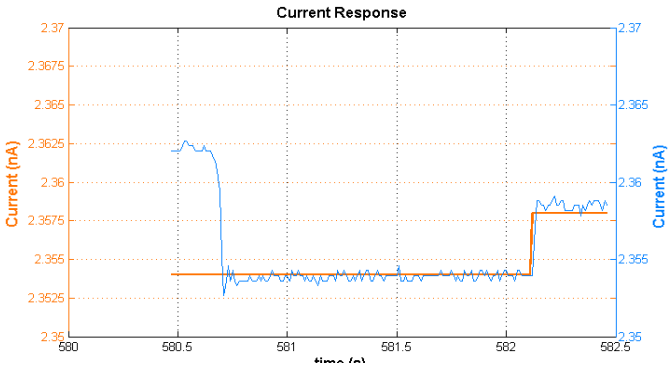

Figure 50 | PID response. The setpoint is represented in orange; the current readings from the pipette positioned by the feedback controller is represented in blue.

Judging the performance, we can see in *Figure 50* the PID response for a changing in the threshold (orange line), showing a fast response and stable threshold tracking by the current signal.

7.1.2. DC Scanning

The DC mode programing implemented was tested, firstly, in a flat surface slightly sloped. *Figure 51* shows the respective XtraceYtrace, XtraceYtrace, XtraceYretrace, XretraceYretrace images. The surface slope follows the pipette movement over the XY stage displacement shown in *Figure 44*.

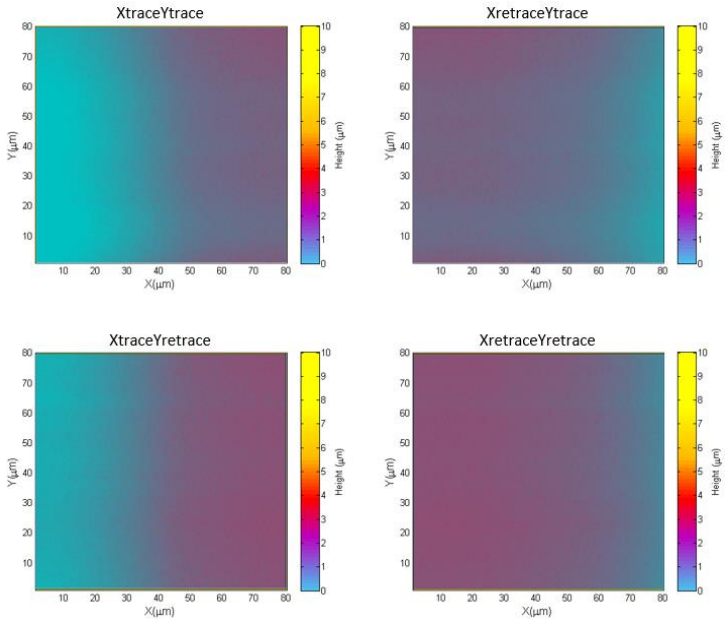

Figure 51 | DC mode scanning of a flat surface. This four images shows the XtraceYtrace, XtraceYtrace, XtraceYretrace and XretraceYretrace according the xy piezo displacement represented in *Figure 44*.

Then, the DC mode scanning was tested in cut PMMA, using a huge pipette (less prone to brake). *Figure 52b* shows imaging of one of those blobs resulting from the PMMA machined, with a setpoint of 4%, resolution of 128 pixels by 128 lines and a scan rate of 1Hz per line.

7.2. Sensitive Backstep hopping mode (SBH mode)

7.2.1. Implementation

As the main program and novel scanning mode, the sensitive backstep hopping mode was implemented. Likewise the traditional hopping mode (*Figure 52*) the probe is lowered to the sample until the given setpoint is reached, and the height is recorded, however in SBH mode the probe is lowered slower close to the surface, detecting the drop in current more accurately. Additionally, instead of dragging back the pipette to a fixed distance, the probe retracts by a defined distance α, increasing the temporal resolution of the scanning. Then the pipette is laterally moved and another measurement is made, and the process repeats until the sample topography be reconstituted.

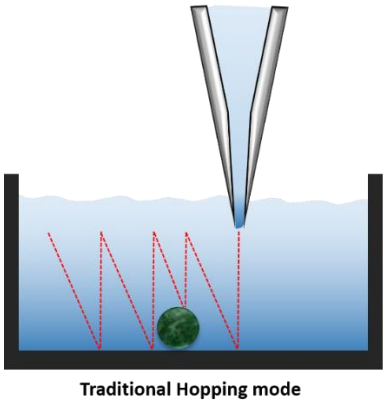

Figure 52 | Traditional Hoping mode scanning.
Here is represented the traditional hopping mode (a).

The performance of a SBH mode was then tested at a scan rate of 100ms per approach curve. Apparently, we have a flatter baseline and better tracking for this scan mode, comparing with the traditional hooping mode performance shown in *Figure 40*.

The SBH mode was implemented in LabVIEW Real-Time and LabVIEW FPGA, ending up with just one image corresponding to the alternate X trace and retrace over Y-axis scanning (shown in *Figure 53*). See the block diagram in *Appendix J*, illustrating this algorithm execution in more detail.

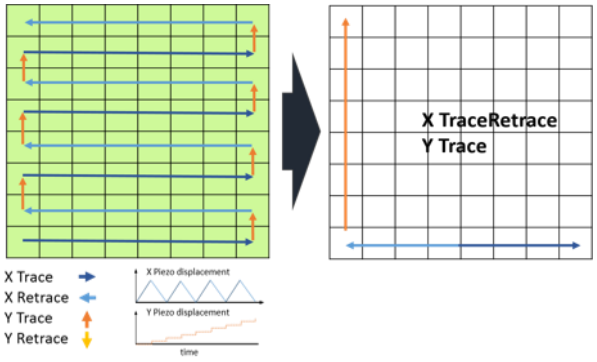

Figure 53 | XY stage displacement. Here we show XY-axis displacement for Hopping mode scanning.

7.2.2. Backstep Scanning

A negative PDMS profile of a meander cooper line (*Figure 54a*) was used as a calibration sample. The figure bellow shows the topography in low resolution of the smaller line in *Figure54d* and the larger line in *Figure54b* with the respective height profile in *Figure54c*. The profile figure shows a good match with the real structure size, 56µm in this case.

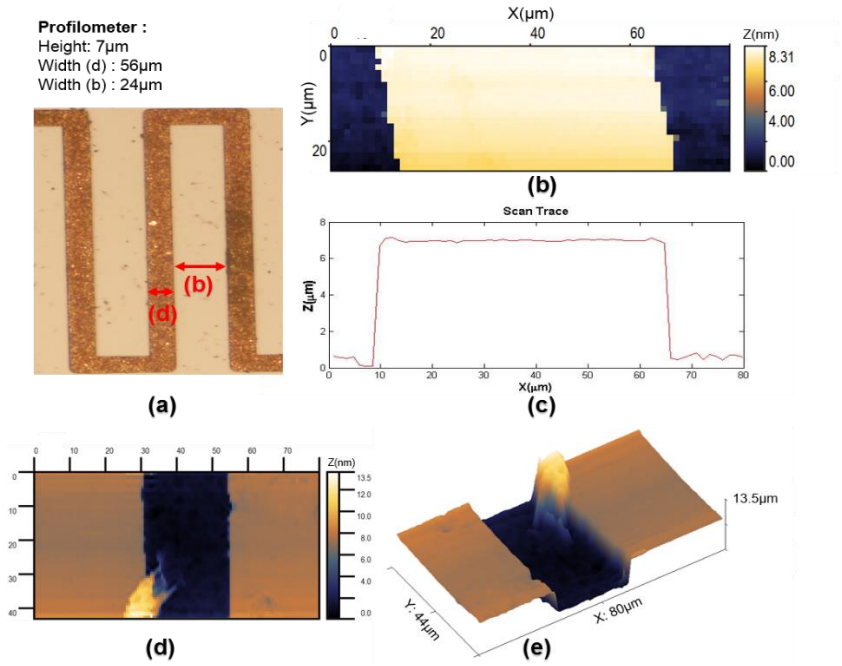

Figure 54 | PDMS Meander cooper line calibration sample. The calibration sample sizes were characterized by a profilometer and the image under optical microscope is shown in A, D shows the topography of the smaller line and the 3D can be seen in E. B shows the larger line and the respective Height profile in E.

Then, higher complexity samples, resulting from cut PMMA with a profile seen in *Figure 55a*, have been scanned. The figure bellow shows the SICM topography *(Figure 55b*) matching with the profile expected from optical microscopy.

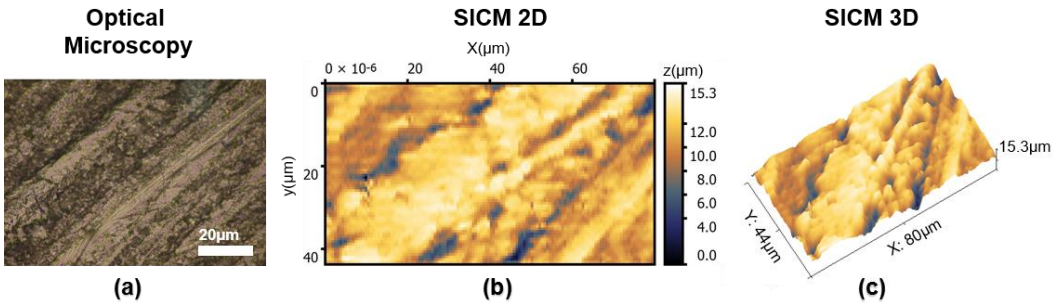

Figure 55 | Complex cut PMMA sample. Optical image of the sample in A, SICM topography in B and 3D image in C.

Finally, in order to simulate suspended features, stretched tape was used for scanning. *Figure 56* shows scanning in low resolution (128 by 128p), at a scan rate of 100ms each approach curve (*Figure 56b and 56c*). Comparing with AFM image (A), the filaments connecting blobs (*Figure 56d*) are tighter, since a setpoint of 2% was used, so that the pipette is interacting and distorting this filaments.

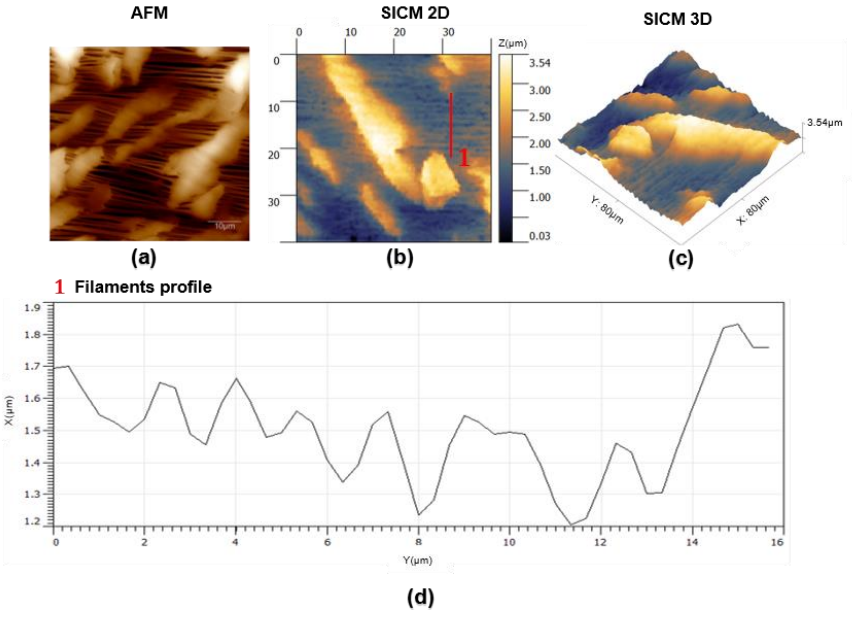

Figure 56 | Stretched tape scanning. AFM scanning in A, SICM scanning in B and C. The filaments profile are shown in D.

Afterwards, in order to obtain a higher resolution image, the same stretched tape was scanned with a resolution of 256pixels by 256lines, at a rate of 100ms per approach curve using

a setpoint of 2% (*Figure 57a*). The reason for using a higher setpoint 2% is because the noise attenuation of my system is not good enough to scan over long periods of time under a setpoint of 2%, and also because the pipettes are too big requiring higher a setpoint for stable current tracking.

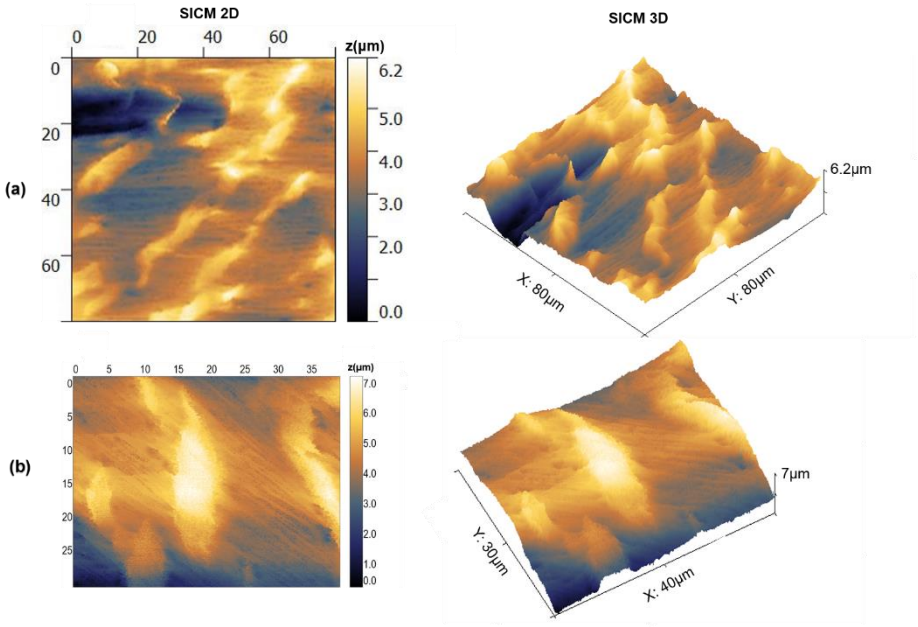

Figure 57 | Stretched tape scanning in higher resolution. Stretched tape scanning in higher resolution in A, and smaller size scanning in B highlighting the filaments connecting blobs.

Chapter 8

Conclusion

The principle of the proposed microscope is the same as conventional SICM. However, here I presented my own approach; resulting in a unique design and construction of a SICM from scratch. In addition, we also reported an innovative scanning mode- sensitive backstep hopping mode (SBH mode), which allows accurate tracking of the setpoint during measurement. Moreover, this SICM has shown imaging of complex and non-adherent structures, under the diffraction limit.

For low noise measurements and higher speed, we need pipette openings in the range of 50nm to 100nm. However, manufacturing of the pipettes with the proper opening size was challenging due to the low reproducibility of the laser pulling machine.

In the future, improvements and setup adaptations have to be implemented for specific applications. The temporal resolution could be increased by optimizing the software and stabilizing the electrochemical system. In addition, in order to be able to move the optical microscopy objective towards the sample, a new XY piezo stage needs to be constructed.

After the optimization of all the parts of the setup, we intend to apply this SICM to biological studies; namely topographical characterization of living cells and bacteria. More interestingly would be the creation of new microscopic techniques; for instance a radiofrequency technique combined with SICM.

Annexes

Appendix A

MatLab Simulation Software Layout

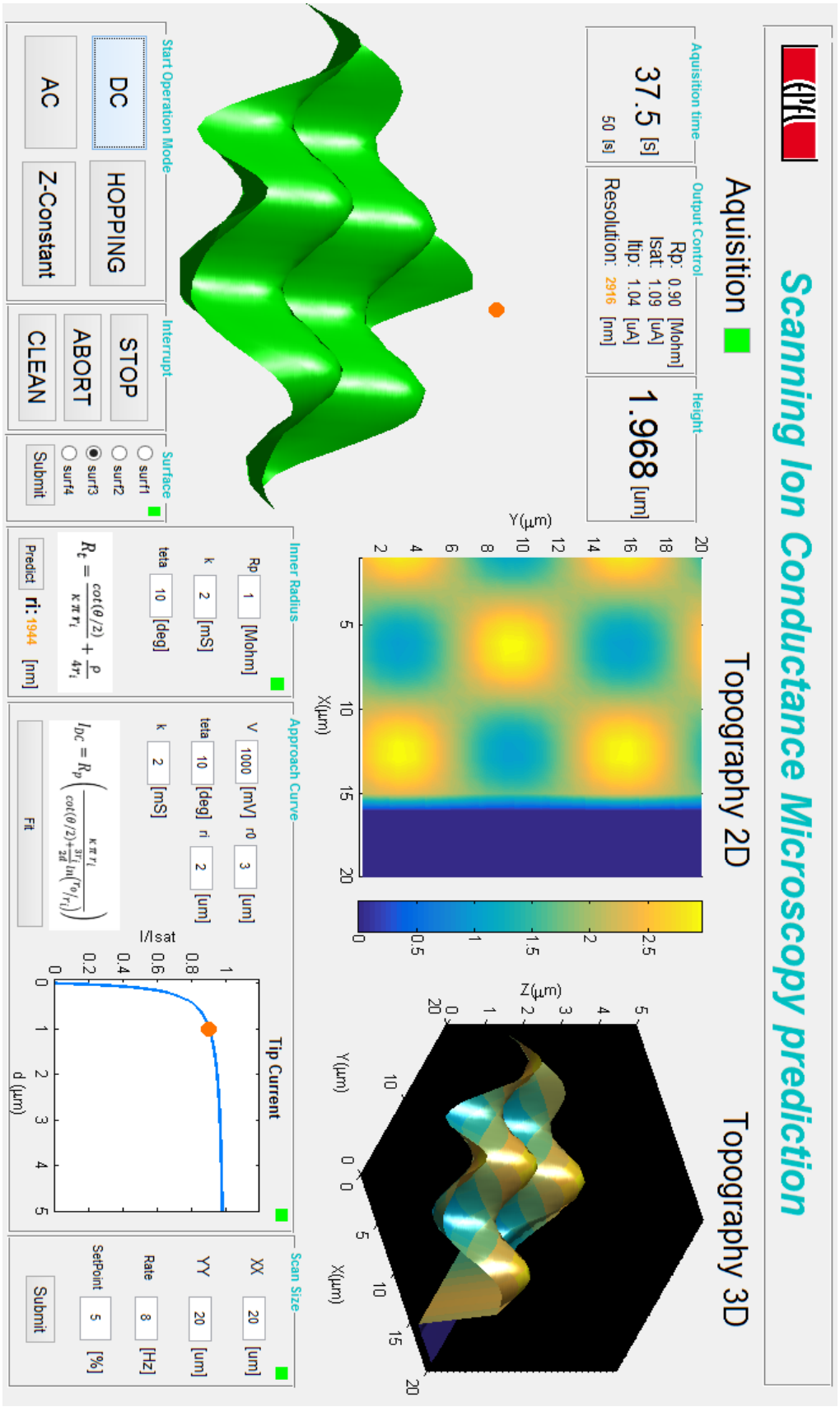

The SICM simulation software functions are briefly explained bellow:

- Inner Radius panel: Used for pipette inner estimation, based on *Equation 8*. For that, we have to set the resistance of the pipette R_p in Mohm, the medium conductivity κ in mS, and the angle between the center axis of the pipette and its walls, *teta* (θ) in degrees.
- Approach Curve panel: Used for pipette sensitivity estimation, based on *Equation 10* model. For that, we have to set the voltage applied to the electrodes terminal V in mV, the resistance of the pipette R_p in MOhm, the medium conductivity κ in mS, the angle between the center axis of the pipette and its walls *teta* (θ) in degrees, and the outer/inner radius (r_o and r_i respectively) in µm.
- Scan Size panel: Contains the parameters to be defined before scanning, XX and YY represents the image size in µm, Sampling Rate in Hz and the setpoint in percentage.
- Start Operation Mode panel: Contains operations mode scanning to be simulated and next panel, Interrupt, comprises control buttons. Surface panel, contains a series of different surfaces to be scanned. The surface loaded is shown above the panel. The orange orb corresponds to the position of pipette opening and the resultant topography is plotted in the center.

On the top panel, the total acquisition time can be seen. In addition, the pipette resistance R_p, the maximum current I_{sat} and current defined in set point I_{sat}, the resolution and the pipette height at each position can be accessed in that panel.

Appendix B

SICM Drawings (SoliDWorks)

- B1 Top Cork
- B2 SICM Tube
- B3 Pipette Adapter
- B4 Bottom Cork
- B5 Top Z Piezo Adapter
- B6 Bottom Z Piezo Adapter
- B7 Z Piezo Plate
- B8 Right SICM Binder
- B9 Left SICM Binder
- B10 Amplifier Support
- B11 XY Piezo Support
- B12 Right Brace Front
- B13 Top Sample Table
- B14 Left Brace Front
- B15 Right Brace Back
- B16 Left Brace Back
- B17 Right Sample Table
- B18 Left Sample Table

Appendix B1

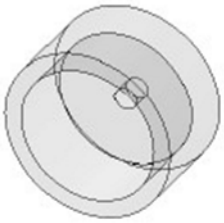

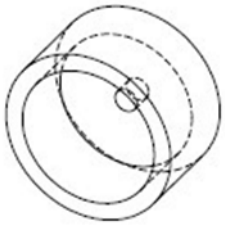

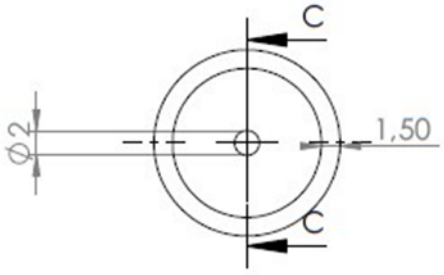

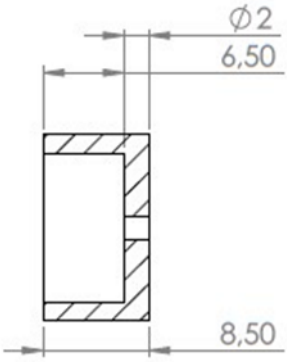

SECTION C-C

	NAME	SIGNATURE	DATE	MATERIAL:	
DRAWN	SAMUEL		03.04.15	PMMA	EPFL STI-IBI-LBNI
CHK'D					
APPV'D					
MFG					
Q.A				DIMENSIONS ARE IN MILLIMETERS TOLERANCES: ISO 2768-f FINISH: NONE DEBUR AND BREAK SHARP EDGES	TITLE: TOP CORK — A4
THE INFORMATION CONTAINED IN THIS DRAWING IS THE SOLE PROPERTY OF LBNI. ANY REPRODUCTION IN PART OR AS A WHOLE WITHOUT THE WRITTEN PERMISSION OF LBNI IS PROHIBITED.				DO NOT SCALE DRAWING	SCALE: 2:1 — SHEET 1 OF 1

Appendix B2

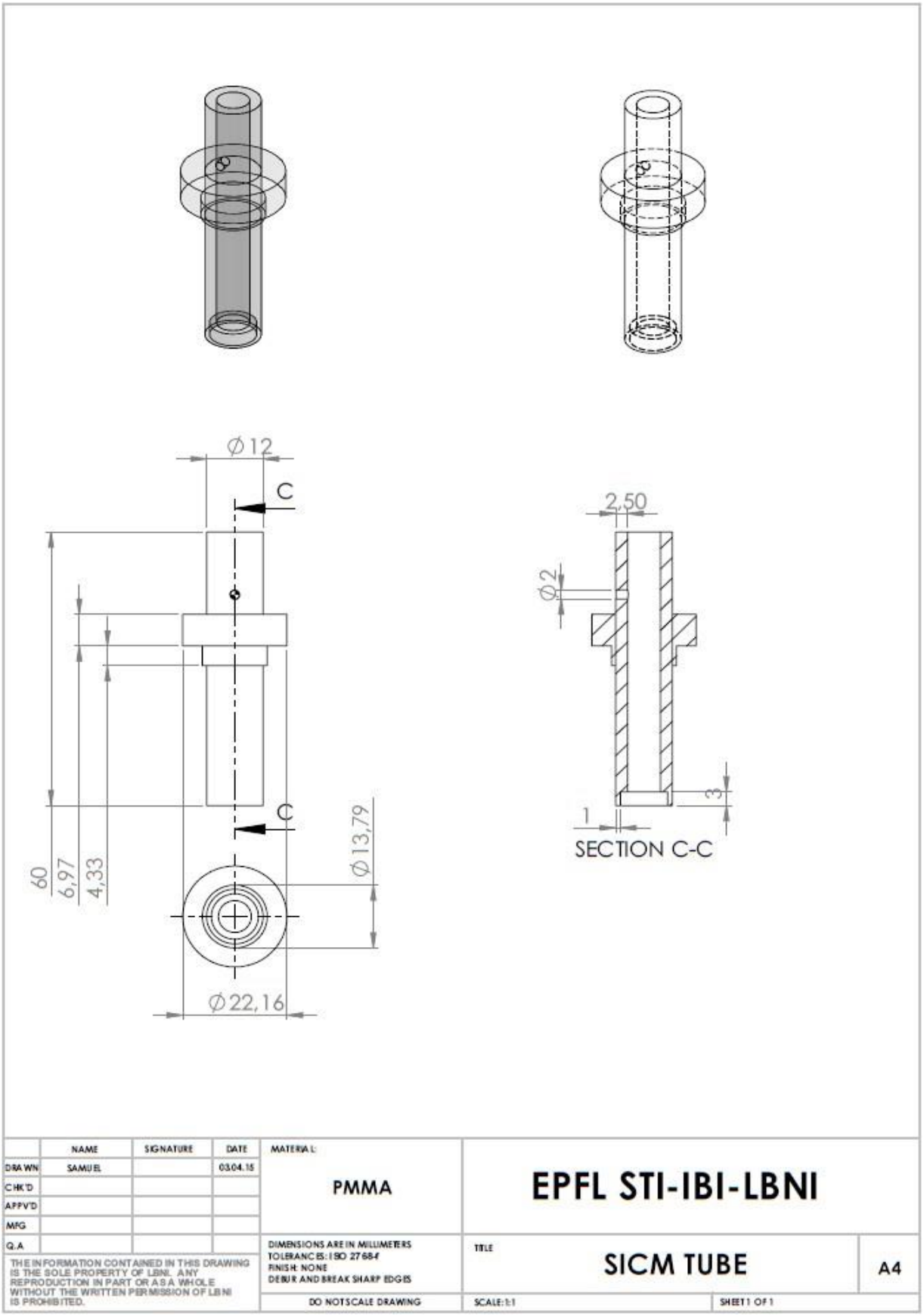

	NAME	SIGNATURE	DATE	MATERIAL:	
DRAWN	SAMUEL		03.04.15	PMMA	EPFL STI-IBI-LBNI
CHK'D					
APPV'D					
MFG					
Q.A				DIMENSIONS ARE IN MILLIMETERS TOLERANCES: ISO 2768-f FINISH: NONE DEBUR AND BREAK SHARP EDGES	TITLE: SICM TUBE — A4
THE INFORMATION CONTAINED IN THIS DRAWING IS THE SOLE PROPERTY OF LBNI. ANY REPRODUCTION IN PART OR AS A WHOLE WITHOUT THE WRITTEN PERMISSION OF LBNI IS PROHIBITED.				DO NOT SCALE DRAWING	SCALE: 1:1 — SHEET 1 OF 1

Appendix B3

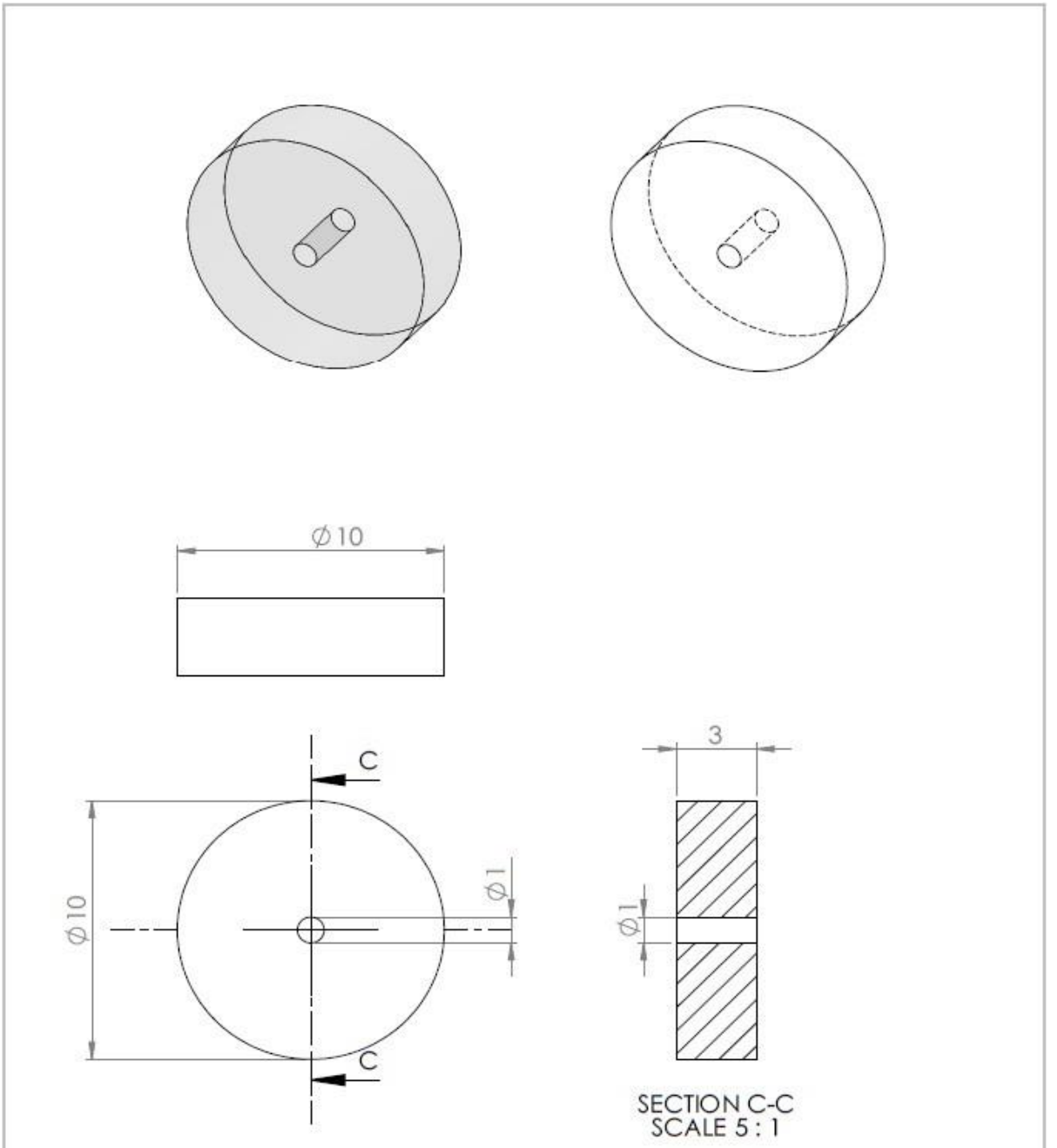

	NAME	SIGNATURE	DATE
DRAWN	SAMUEL		03.04.15
CHK'D			
APPV'D			
MFG			
Q.A			

THE INFORMATION CONTAINED IN THIS DRAWING IS THE SOLE PROPERTY OF LBNI. ANY REPRODUCTION IN PART OR AS A WHOLE WITHOUT THE WRITTEN PERMISSION OF LBNI IS PROHIBITED.

MATERIAL: PMMA

DIMENSIONS ARE IN MILLIMETERS
TOLERANCES: ISO 2768-f
FINISH: NONE
DEBUR AND BREAK SHARP EDGES

DO NOT SCALE DRAWING

EPFL STI-IBI-LBNI

TITLE: PIPETTE ADAPTER

A4

SCALE: 5:1

SHEET 1 OF 1

Appendix B4

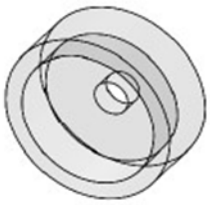

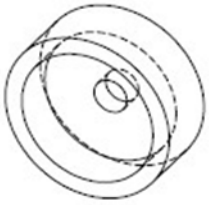

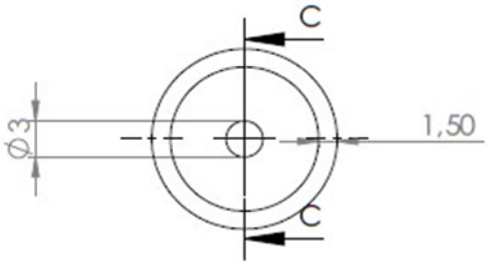

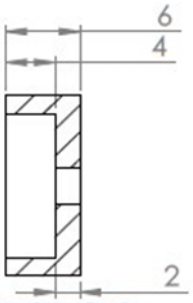

SECTION C-C
SCALE 2 : 1

	NAME	SIGNATURE	DATE	MATERIAL:	
DRAWN	SAMUEL		03.04.15	PMMA	EPFL STI-IBI-LBNI
CHK'D					
APPV'D					
MFG					
Q.A					

THE INFORMATION CONTAINED IN THIS DRAWING IS THE SOLE PROPERTY OF LBNI. ANY REPRODUCTION IN PART OR AS A WHOLE WITHOUT THE WRITTEN PERMISSION OF LBNI IS PROHIBITED.

DIMENSIONS ARE IN MILLIMETERS
TOLERANCES: ISO 2768-f
FINISH: NONE
DEBUR AND BREAK SHARP EDGES

TITLE: BOTTOM CORK

A4

DO NOT SCALE DRAWING | SCALE: 2:1 | SHEET 1 OF 1

Appendix B5

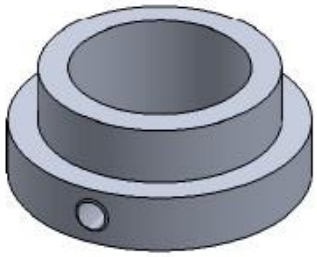

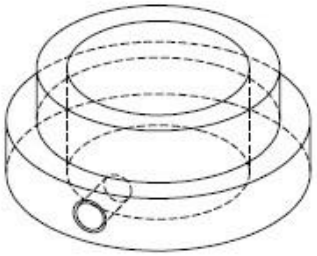

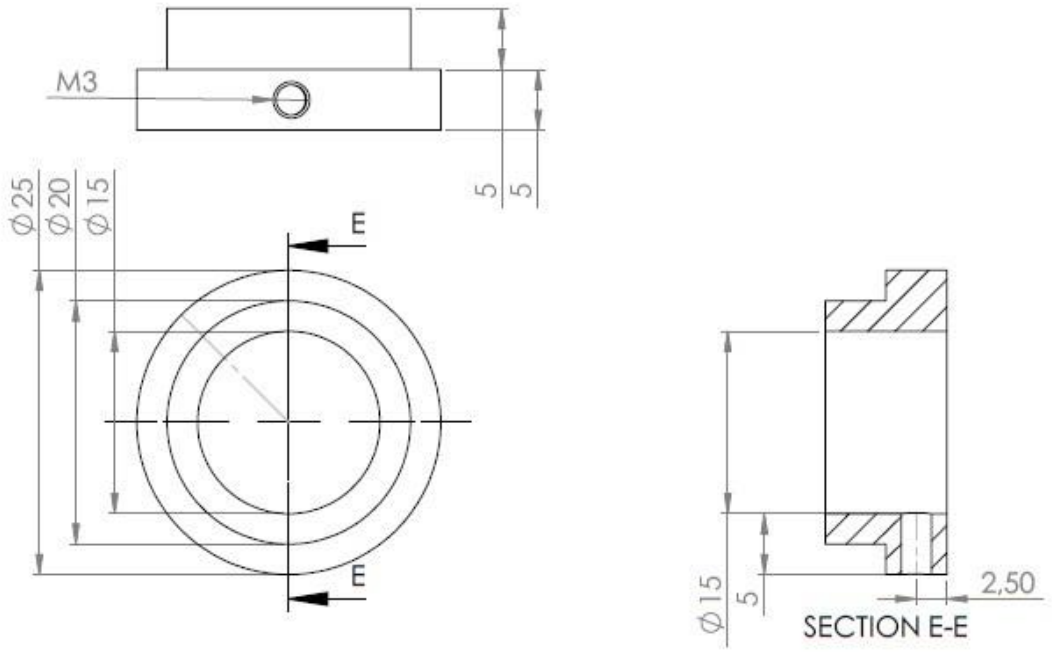

	NAME	SIGNATURE	DATE	MATERIAL:	EPFL STI-IBI-LBNI	
DRAWN	SAMUEL		03.04.15	ALUMINUN 6082-T6		
CHK'D						
APPV'D						
MFG						
Q.A				DIMENSIONS ARE IN MILLIMETERS TOLERANCES: ISO 2768-f FINISH: NONE DEBUR AND BREAK SHARP EDGES	TITLE: TOP ZPIEZO ADAPTER	A4
THE INFORMATION CONTAINED IN THIS DRAWING IS THE SOLE PROPERTY OF LBNI. ANY REPRODUCTION IN PART OR AS A WHOLE WITHOUT THE WRITTEN PERMISSION OF LBNI IS PROHIBITED.				DO NOT SCALE DRAWING	SCALE: 2:1	SHEET 1 OF 1

Appendix B6

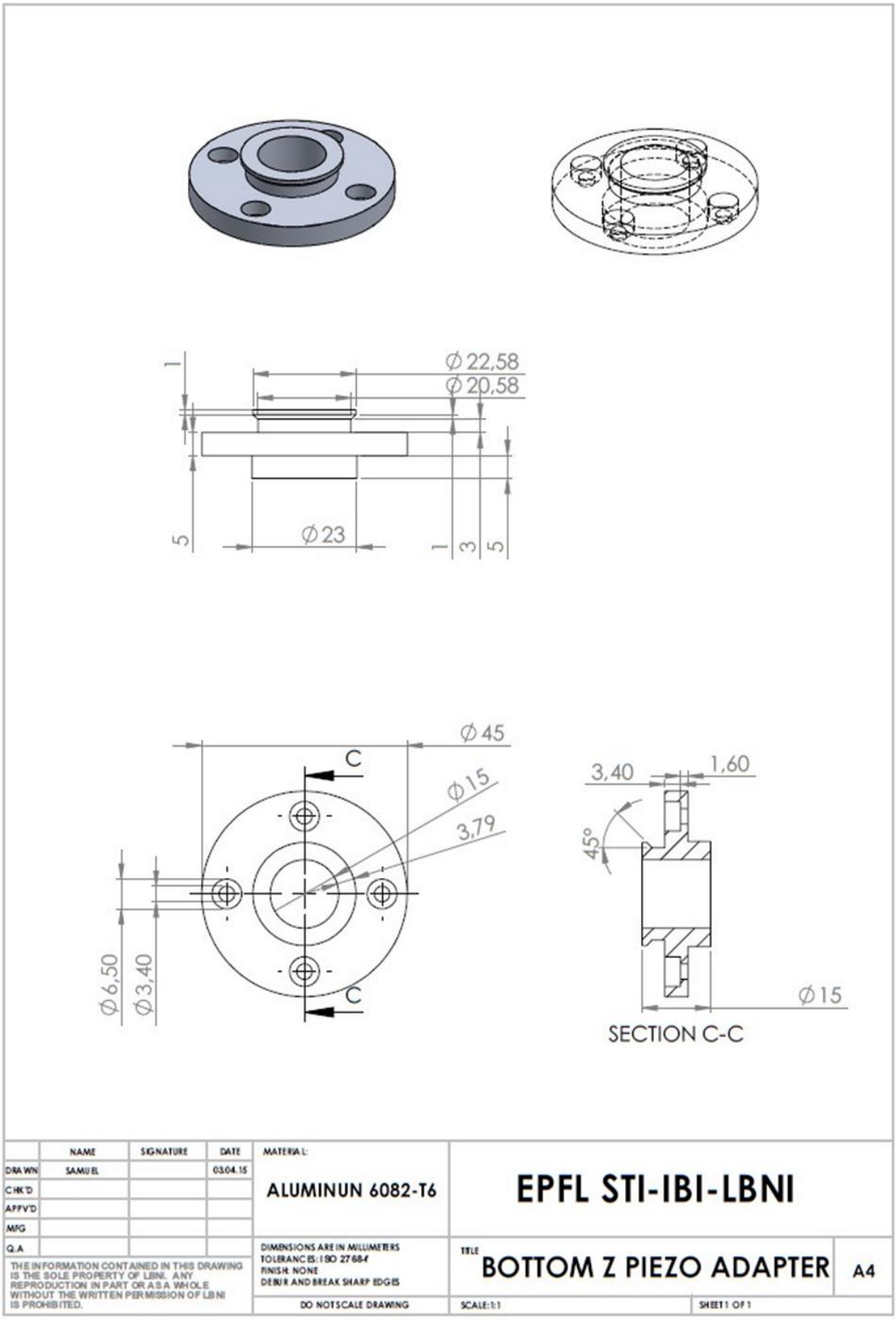

	NAME	SIGNATURE	DATE
DRAWN	SAMUEL		03.04.15
CHK'D			
APPV'D			
MFG			
Q.A			

THE INFORMATION CONTAINED IN THIS DRAWING IS THE SOLE PROPERTY OF LBNI. ANY REPRODUCTION IN PART OR AS A WHOLE WITHOUT THE WRITTEN PERMISSION OF LBNI IS PROHIBITED.

MATERIAL: ALUMINUN 6082-T6

DIMENSIONS ARE IN MILLIMETERS
TOLERANCES: ISO 2768f
FINISH: NONE
DEBUR AND BREAK SHARP EDGES

DO NOT SCALE DRAWING

EPFL STI-IBI-LBNI

TITLE: BOTTOM Z PIEZO ADAPTER

A4

SCALE: 1:1

SHEET 1 OF 1

Appendix B7

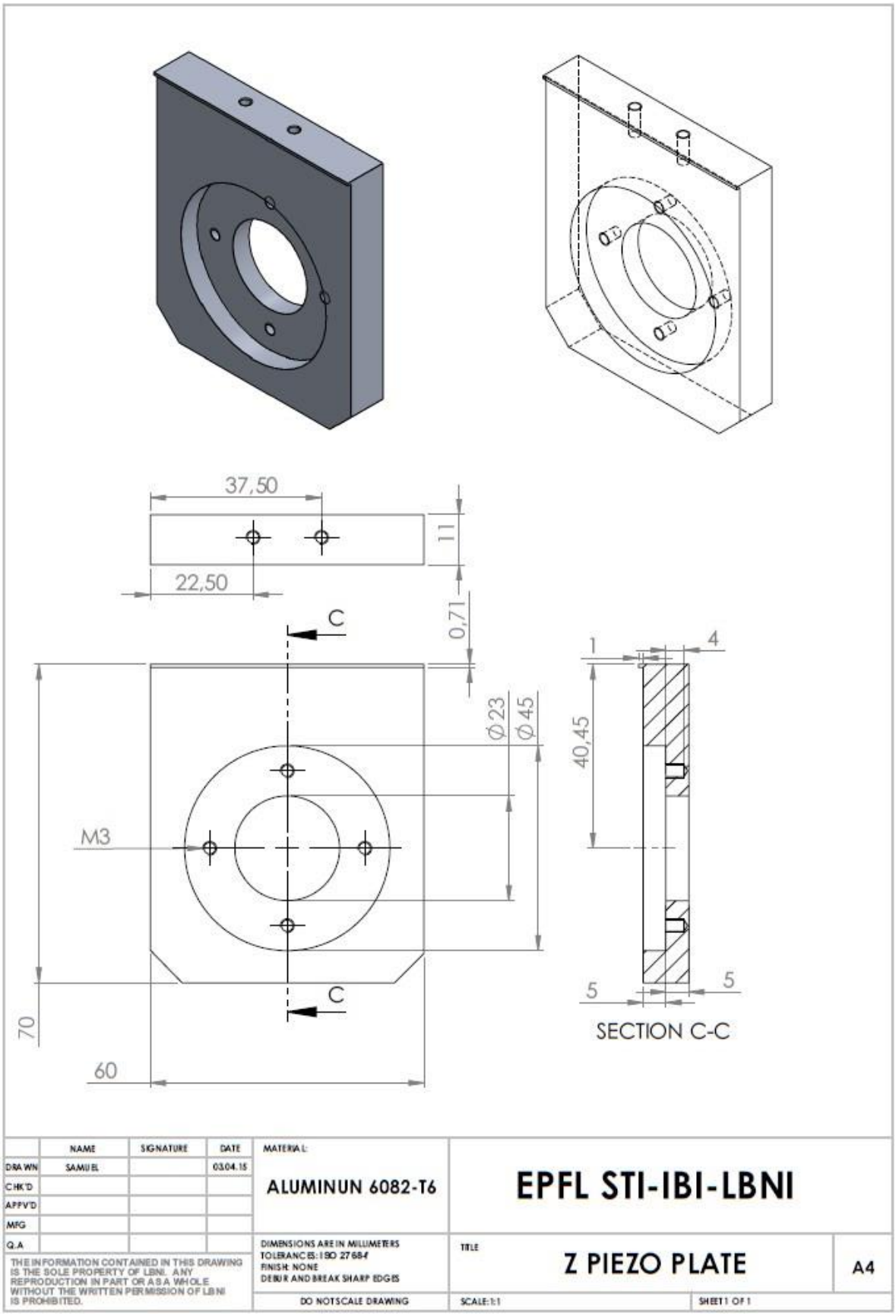

	NAME	SIGNATURE	DATE
DRAWN	SAMUEL		03.04.15
CHK'D			
APPV'D			
MFG			
Q.A			

THE INFORMATION CONTAINED IN THIS DRAWING IS THE SOLE PROPERTY OF LBNI. ANY REPRODUCTION IN PART OR AS A WHOLE WITHOUT THE WRITTEN PERMISSION OF LBNI IS PROHIBITED.

MATERIAL: ALUMINUN 6082-T6

DIMENSIONS ARE IN MILLIMETERS
TOLERANCES: ISO 2768-f
FINISH: NONE
DEBUR AND BREAK SHARP EDGES

DO NOT SCALE DRAWING

EPFL STI-IBI-LBNI

TITLE: **Z PIEZO PLATE**

A4

SCALE: 1:1

SHEET 1 OF 1

Appendix B8

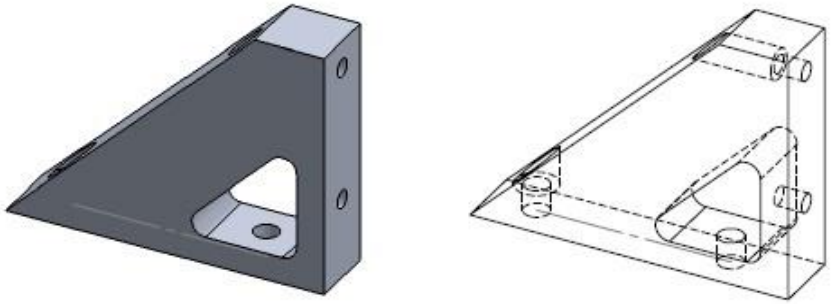

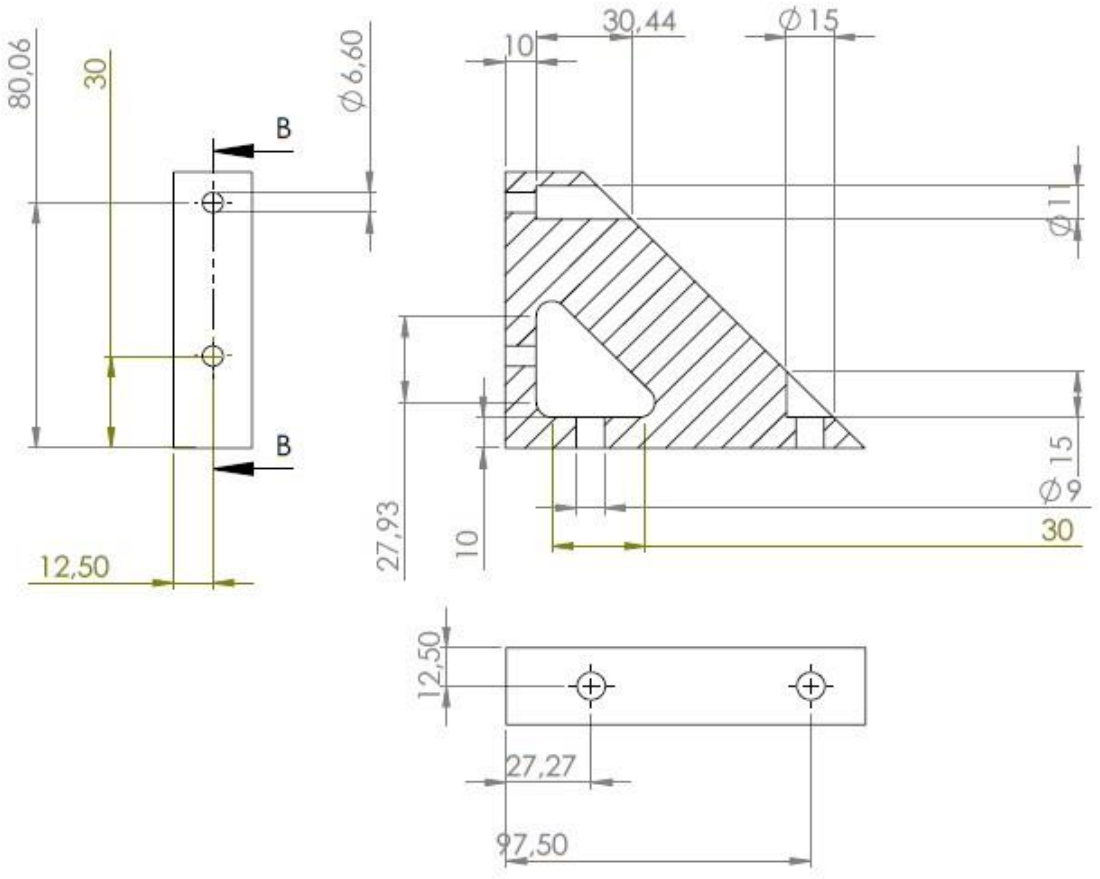

	NAME	SIGNATURE	DATE
DRAWN	SAMUEL		03.04.15
CHK'D			
APPV'D			
MFG			
Q.A			

THE INFORMATION CONTAINED IN THIS DRAWING IS THE SOLE PROPERTY OF LBNI. ANY REPRODUCTION IN PART OR AS A WHOLE WITHOUT THE WRITTEN PERMISSION OF LBNI IS PROHIBITED.

MATERIAL:
ALUMINUN 6082-T6

DIMENSIONS ARE IN MILLIMETERS
TOLERANCES: ISO 2768-f
FINISH: NONE
DEBUR AND BREAK SHARP EDGES

DO NOT SCALE DRAWING

EPFL STI-IBI-LBNI

TITLE
RIGHT SICM BINDER

A4

SCALE: 1:2

SHEET 1 OF 1

Appendix B9

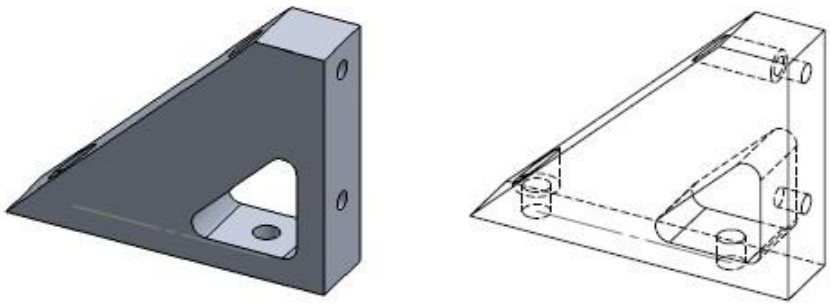

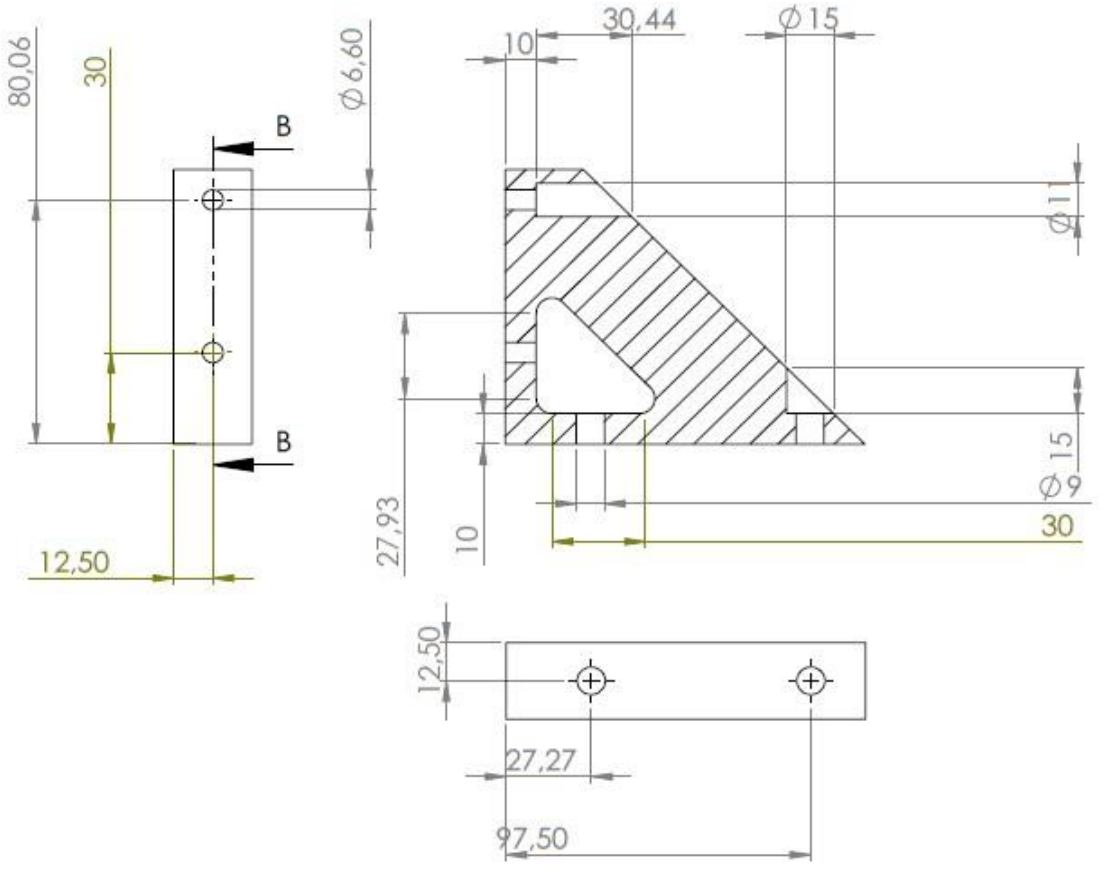

	NAME	SIGNATURE	DATE	MATERIAL:	
DRAWN	SAMUEL		03.04.15	ALUMINUN 6082-T6	EPFL STI-IBI-LBNI
CHK'D					
APPV'D					
MFG					
Q.A					

THE INFORMATION CONTAINED IN THIS DRAWING IS THE SOLE PROPERTY OF LBNI. ANY REPRODUCTION IN PART OR AS A WHOLE WITHOUT THE WRITTEN PERMISSION OF LBNI IS PROHIBITED.

DIMENSIONS ARE IN MILLIMETERS
TOLERANCES: ISO 2768-f
FINISH: NONE
DEBUR AND BREAK SHARP EDGES

DO NOT SCALE DRAWING

TITLE: LEFT SICM BINDER

A4

SCALE: 1:2

SHEET 1 OF 1

Appendix B10

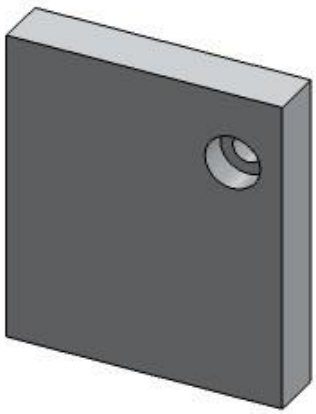

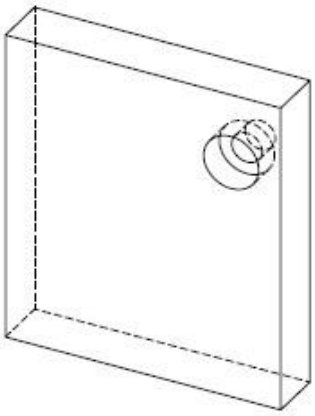

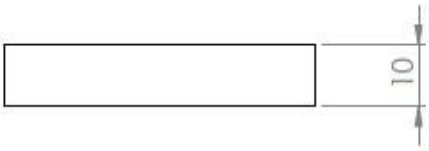

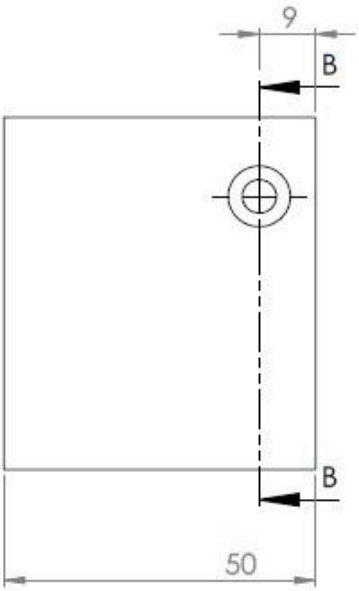

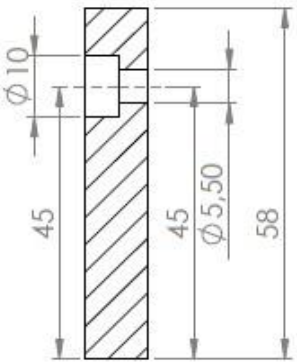

SECTION B-B

	NAME	SIGNATURE	DATE
DRAWN	SAMUEL		03.04.15
CHK'D			
APPV'D			
MFG			
Q.A			

THE INFORMATION CONTAINED IN THIS DRAWING IS THE SOLE PROPERTY OF LBNI. ANY REPRODUCTION IN PART OR AS A WHOLE WITHOUT THE WRITTEN PERMISSION OF LBNI IS PROHIBITED.

MATERIAL: ALUMINUN 6082-T6

DIMENSIONS ARE IN MILLIMETERS
TOLERANCES: ISO 2768f
FINISH: NONE
DEBUR AND BREAK SHARP EDGES

DO NOT SCALE DRAWING

EPFL STI-IBI-LBNI

TITLE: **AMPLIFIER SUPPORT**

A4

SCALE: 1:1

SHEET 1 OF 1

Appendix B11

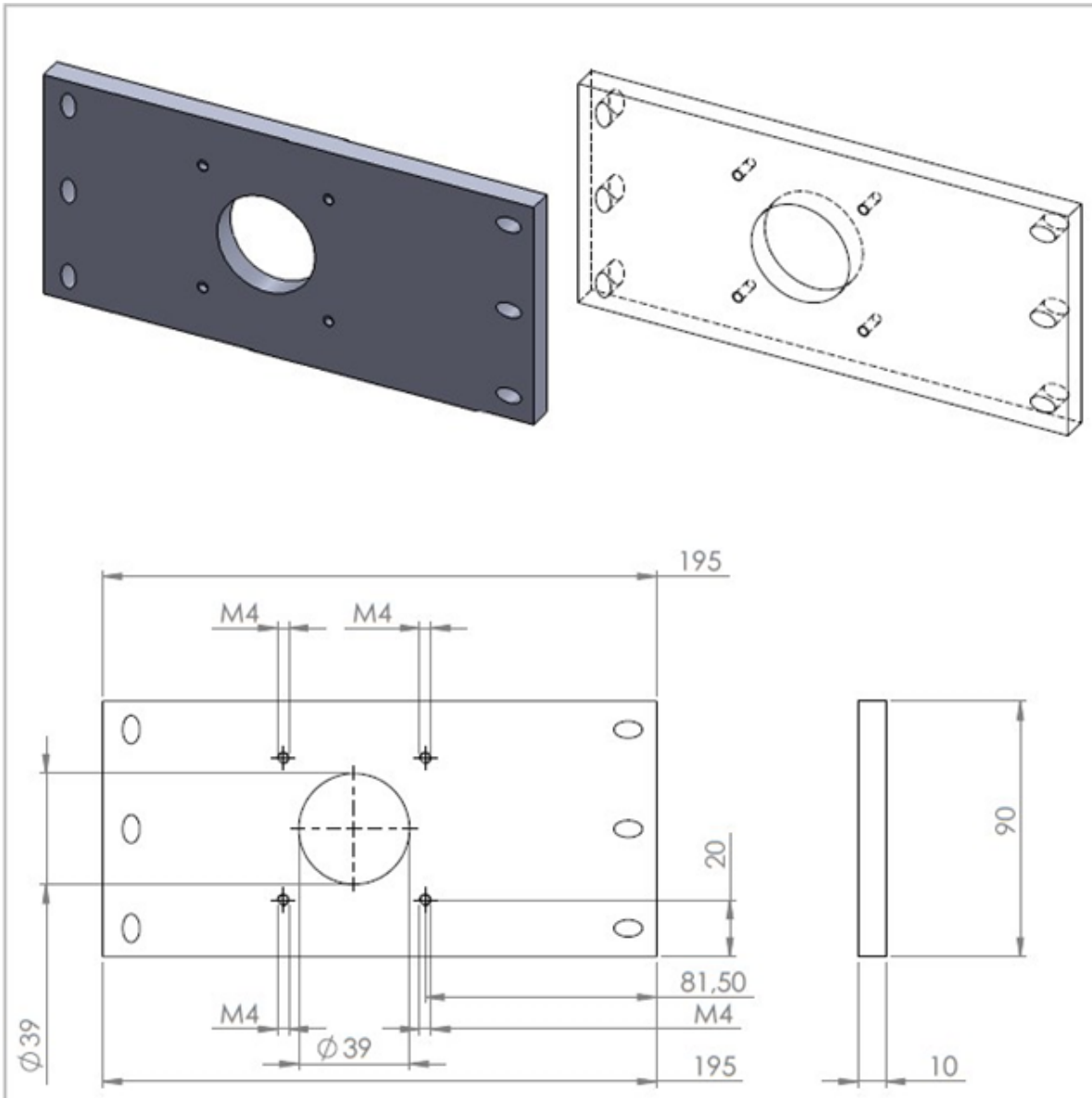

	NAME	SIGNATURE	DATE
DRAWN	SAMUEL		03.04.15
CHK'D			
APP'D			
MFG			
Q.A			

THE INFORMATION CONTAINED IN THIS DRAWING IS THE SOLE PROPERTY OF LBNI. ANY REPRODUCTION IN PART OR AS A WHOLE WITHOUT THE WRITTEN PERMISSION OF LBNI IS PROHIBITED.

MATERIAL: ALUMINUN 6082-T6

DIMENSIONS ARE IN MILLIMETERS
TOLERANCES: ISO 2768f
FINISH: NONE
DEBUR AND BREAK SHARP EDGES

DO NOT SCALE DRAWING

EPFL STI-IBI-LBNI

TITLE: **XY PIEZO SUPPORT**

A4

SCALE: 1:1

SHEET 1 OF 1

Appendix B12

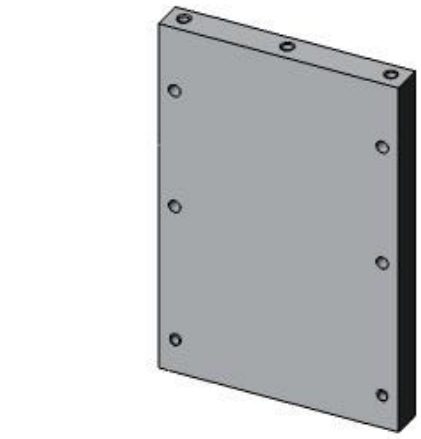

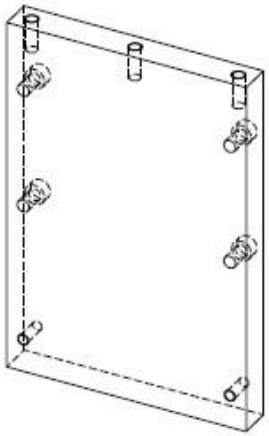

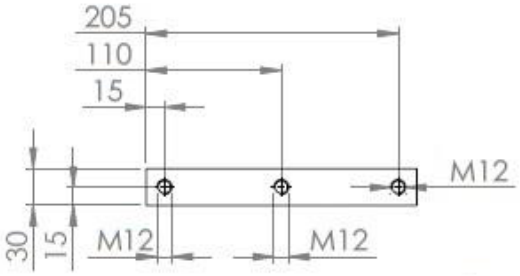

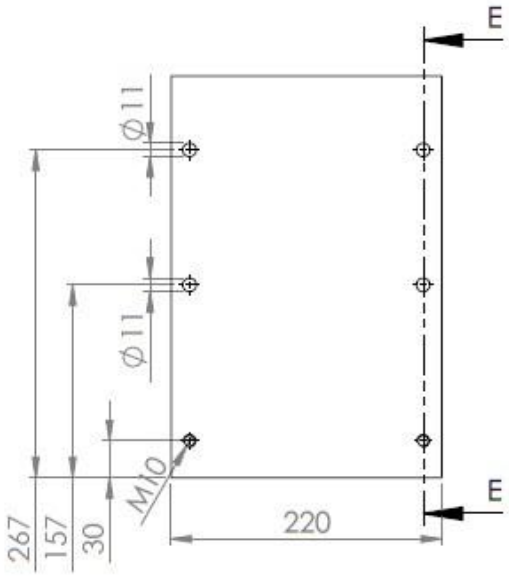

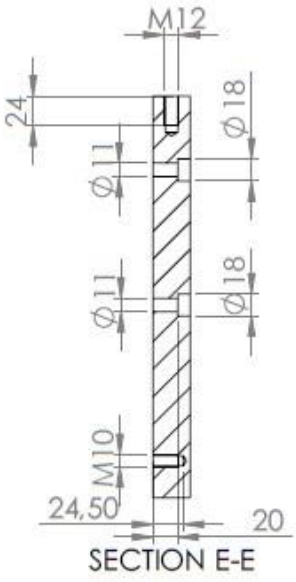

	NAME	SIGNATURE	DATE	MATERIAL:	
DRAWN	SAMUEL		03.04.15	ALUMINUN 6082-T6	EPFL STI-IBI-LBNI
CHK'D					
APPV'D					
MFG					
Q.A				DIMENSIONS ARE IN MILLIMETERS TOLERANCES: ISO 2768-f FINISH: NONE DEBUR AND BREAK SHARP EDGES	TITLE: RIGHT SAMPLE TABLE — A4
THE INFORMATION CONTAINED IN THIS DRAWING IS THE SOLE PROPERTY OF LBNI. ANY REPRODUCTION IN PART OR AS A WHOLE WITHOUT THE WRITTEN PERMISSION OF LBNI IS PROHIBITED.				DO NOT SCALE DRAWING	SCALE: 1:5 — SHEET 1 OF 1

Appendix B13

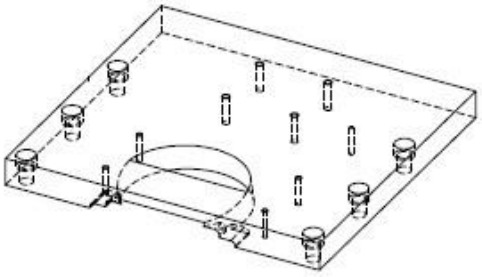

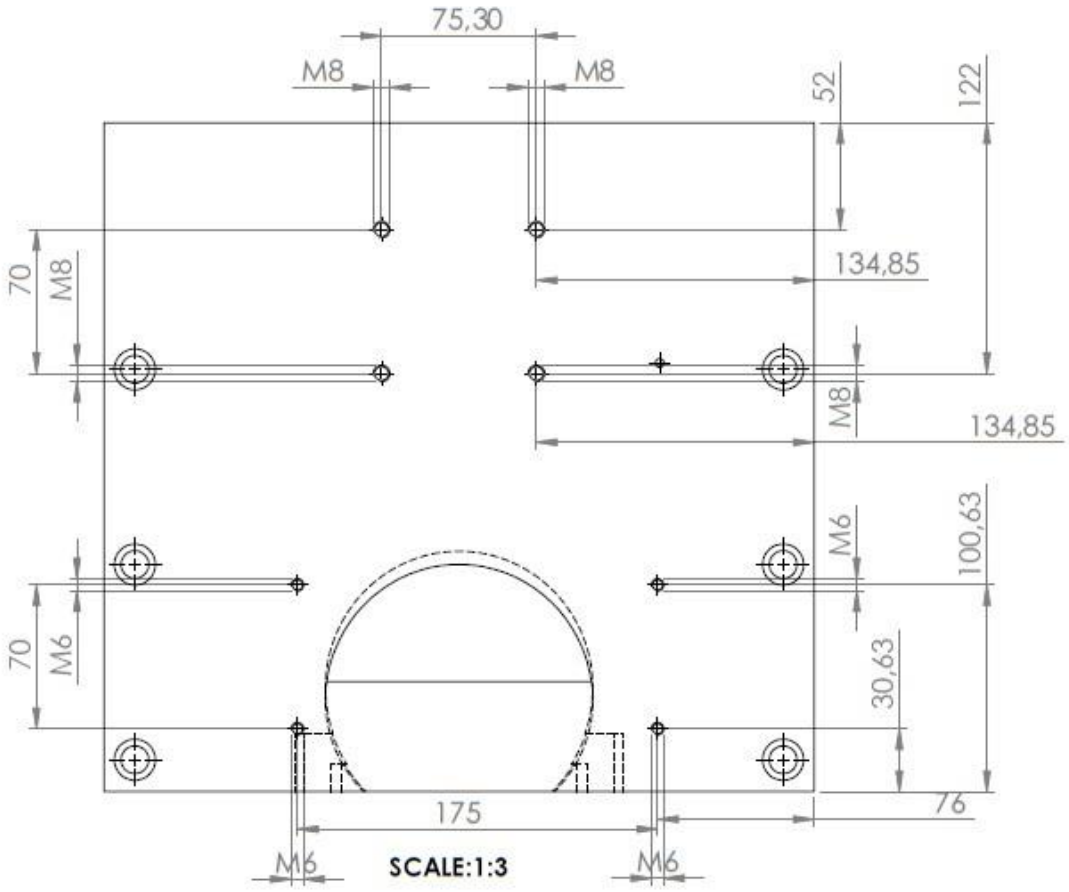

	NAME	SIGNATURE	DATE
DRAWN	SAMUEL		03.04.15
CHK'D			
APPV'D			
MFG			
Q.A			

THE INFORMATION CONTAINED IN THIS DRAWING IS THE SOLE PROPERTY OF LBNI. ANY REPRODUCTION IN PART OR AS A WHOLE WITHOUT THE WRITTEN PERMISSION OF LBNI IS PROHIBITED.

MATERIAL: ALUMINUN 6082-T6

DIMENSIONS ARE IN MILLIMETERS
TOLERANCES: ISO 2768-f
FINISH: NONE
DEBUR AND BREAK SHARP EDGES

DO NOT SCALE DRAWING

EPFL STI-IBI-LBNI

TITLE: **TOP SAMPLE TABLE**

A4

SCALE: 1:6

SHEET 1 OF 1

Appendix B14

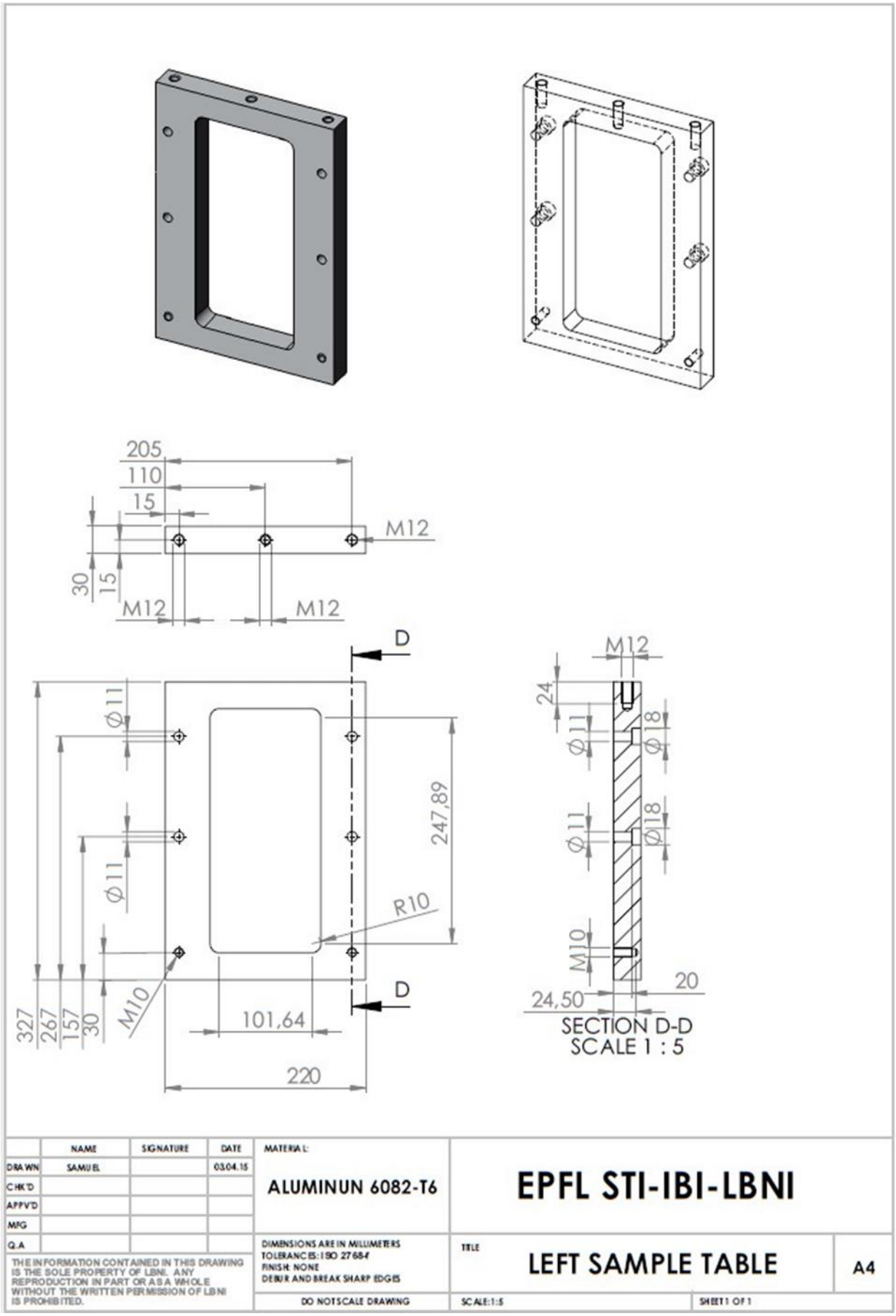

	NAME	SIGNATURE	DATE
DRAWN	SAMUEL		03.04.15
CHK'D			
APPV'D			
MFG			
Q.A			

THE INFORMATION CONTAINED IN THIS DRAWING IS THE SOLE PROPERTY OF LBNI. ANY REPRODUCTION IN PART OR AS A WHOLE WITHOUT THE WRITTEN PERMISSION OF LBNI IS PROHIBITED.

MATERIAL: ALUMINUN 6082-T6

DIMENSIONS ARE IN MILLIMETERS
TOLERANCES: ISO 2768-f
FINISH: NONE
DEBUR AND BREAK SHARP EDGES

DO NOT SCALE DRAWING

EPFL STI-IBI-LBNI

TITLE: **LEFT SAMPLE TABLE**

A4

SCALE: 1:5

SHEET 1 OF 1

Appendix B15

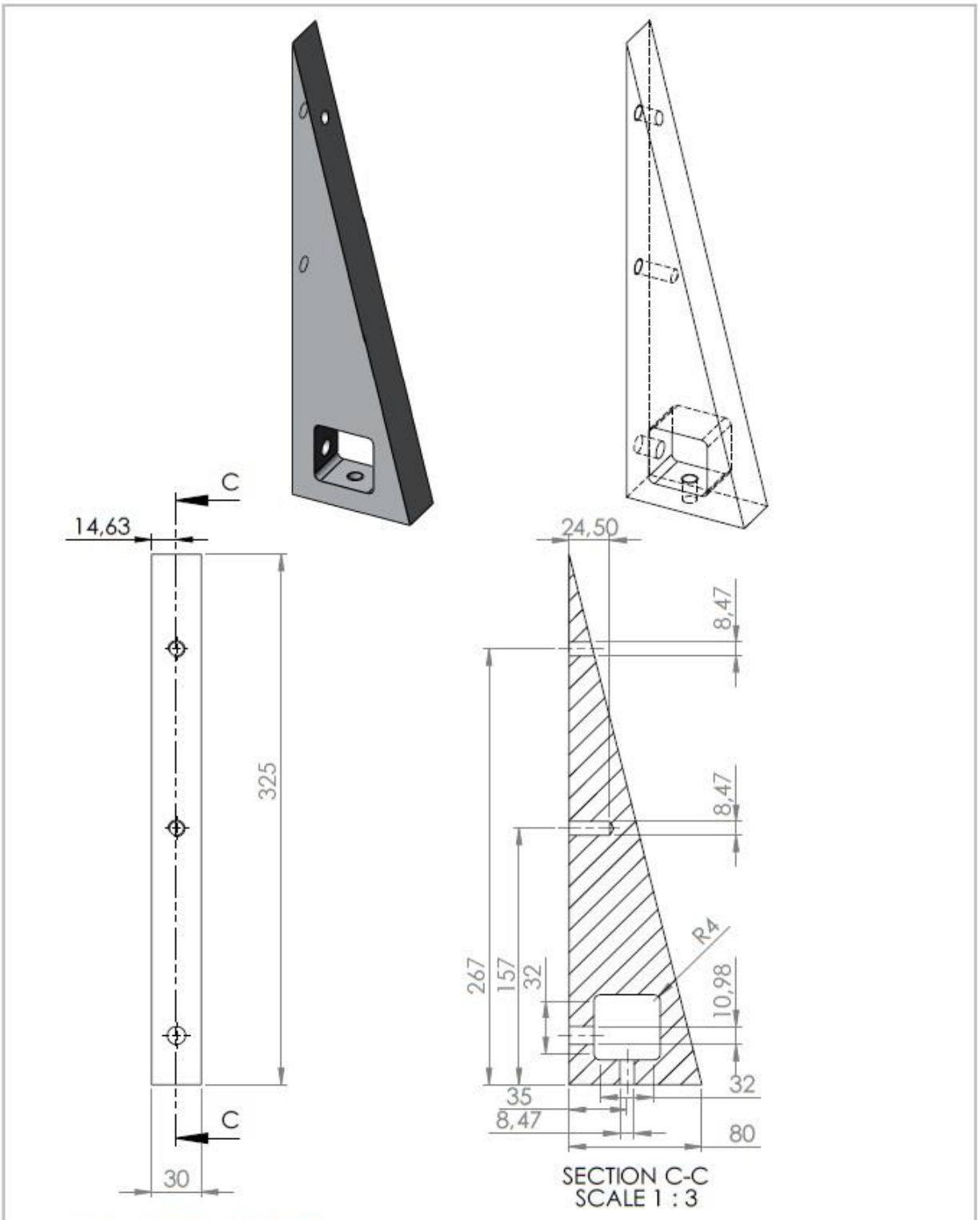

	NAME	SIGNATURE	DATE
DRAWN	SAMUEL		03.04.15
CHK'D			
APPV'D			
MFG			
Q.A			

THE INFORMATION CONTAINED IN THIS DRAWING IS THE SOLE PROPERTY OF LBNI. ANY REPRODUCTION IN PART OR AS A WHOLE WITHOUT THE WRITTEN PERMISSION OF LBNI IS PROHIBITED.

MATERIAL: ALUMINUN 6082-T6

DIMENSIONS ARE IN MILLIMETERS
TOLERANCES: ISO 2768f
FINISH: NONE
DEBUR AND BREAK SHARP EDGES

DO NOT SCALE DRAWING

EPFL STI-IBI-LBNI

TITLE: **RIGHT BRACE FRONT**

A4

SCALE: 1:3

SHEET 1 OF 1

Appendix B16

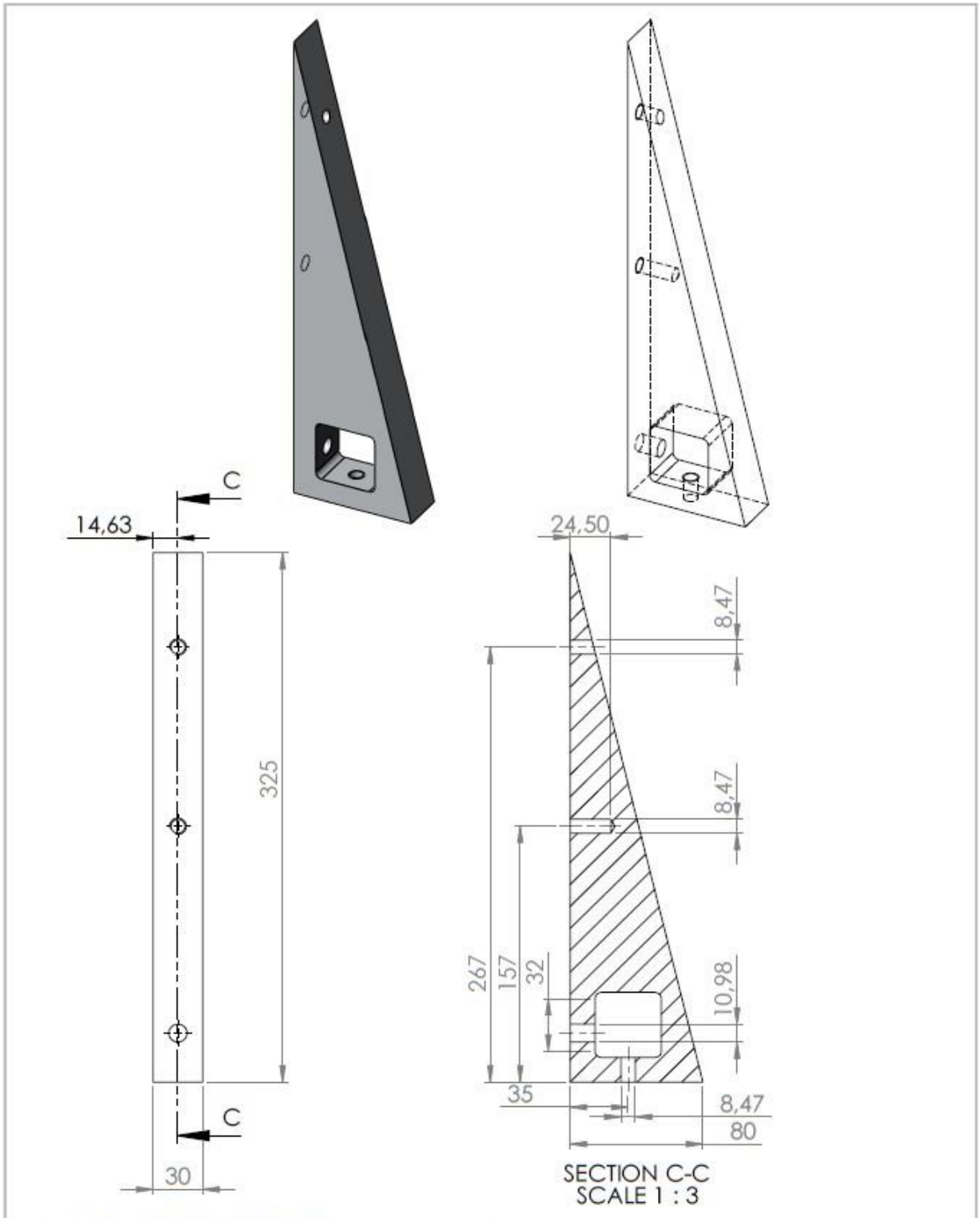

	NAME	SIGNATURE	DATE
DRAWN	SAMUEL		03.04.15
CHK'D			
APPV'D			
MFG			
Q.A			

THE INFORMATION CONTAINED IN THIS DRAWING IS THE SOLE PROPERTY OF LBNI. ANY REPRODUCTION IN PART OR AS A WHOLE WITHOUT THE WRITTEN PERMISSION OF LBNI IS PROHIBITED.

MATERIAL: ALUMINUN 6082-T6

DIMENSIONS ARE IN MILLIMETERS
TOLERANCES: ISO 2768f
FINISH: NONE
DEBUR AND BREAK SHARP EDGES

DO NOT SCALE DRAWING

EPFL STI-IBI-LBNI

TITLE: **LEFT BRACE FRONT**

A4

SCALE: 1:3

SHEET 1 OF 1

Appendix B17

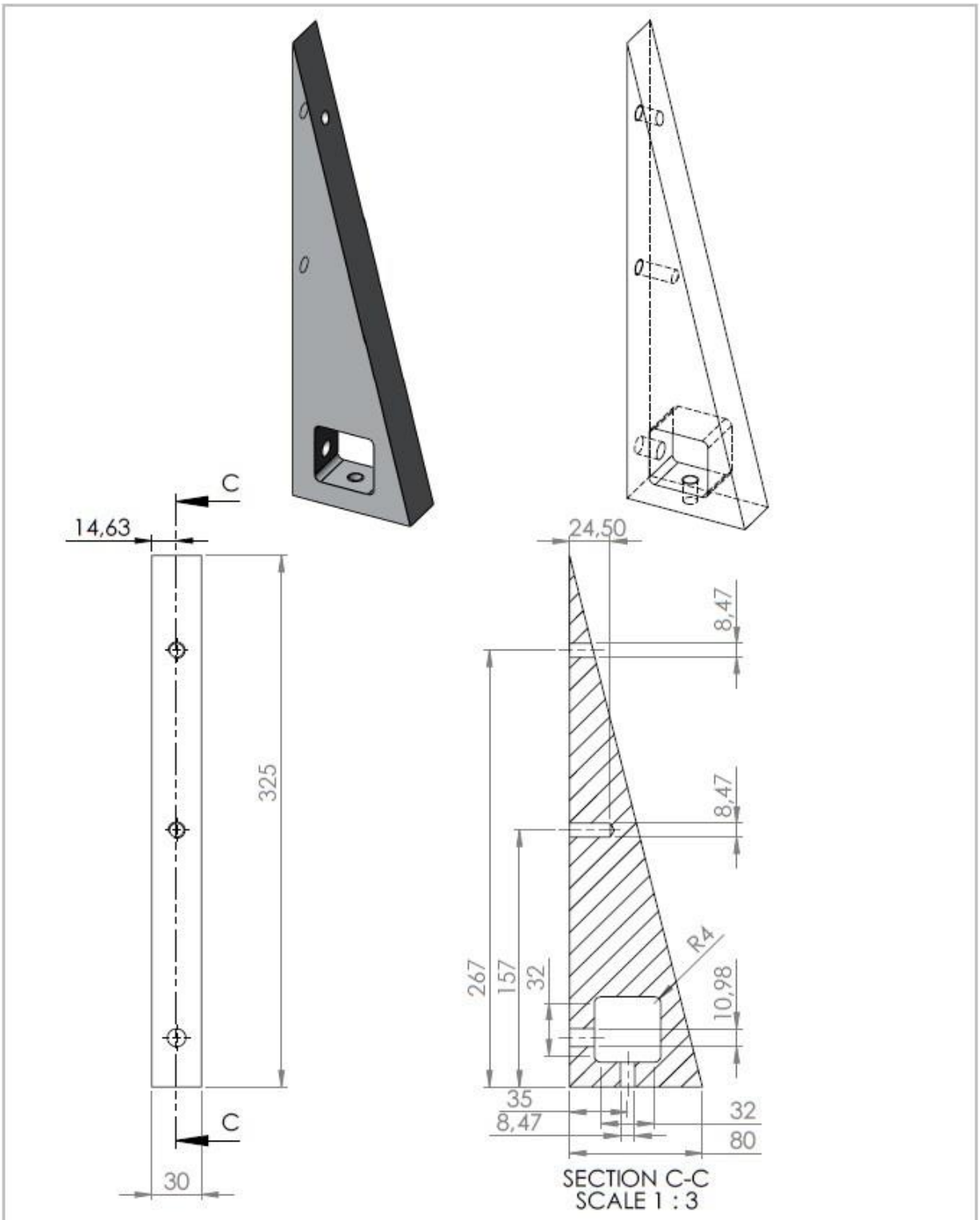

	NAME	SIGNATURE	DATE
DRAWN	SAMUEL		03.04.15
CHK'D			
APPV'D			
MFG			
Q.A			

THE INFORMATION CONTAINED IN THIS DRAWING IS THE SOLE PROPERTY OF LBNI. ANY REPRODUCTION IN PART OR AS A WHOLE WITHOUT THE WRITTEN PERMISSION OF LBNI IS PROHIBITED.

MATERIAL: ALUMINUN 6082-T6

DIMENSIONS ARE IN MILLIMETERS
TOLERANCES: ISO 2768f
FINISH: NONE
DEBUR AND BREAK SHARP EDGES

DO NOT SCALE DRAWING

EPFL STI-IBI-LBNI

TITLE: **RIGHT BRACE BACK**

A4

SCALE: 1:3

SHEET 1 OF 1

Appendix B18

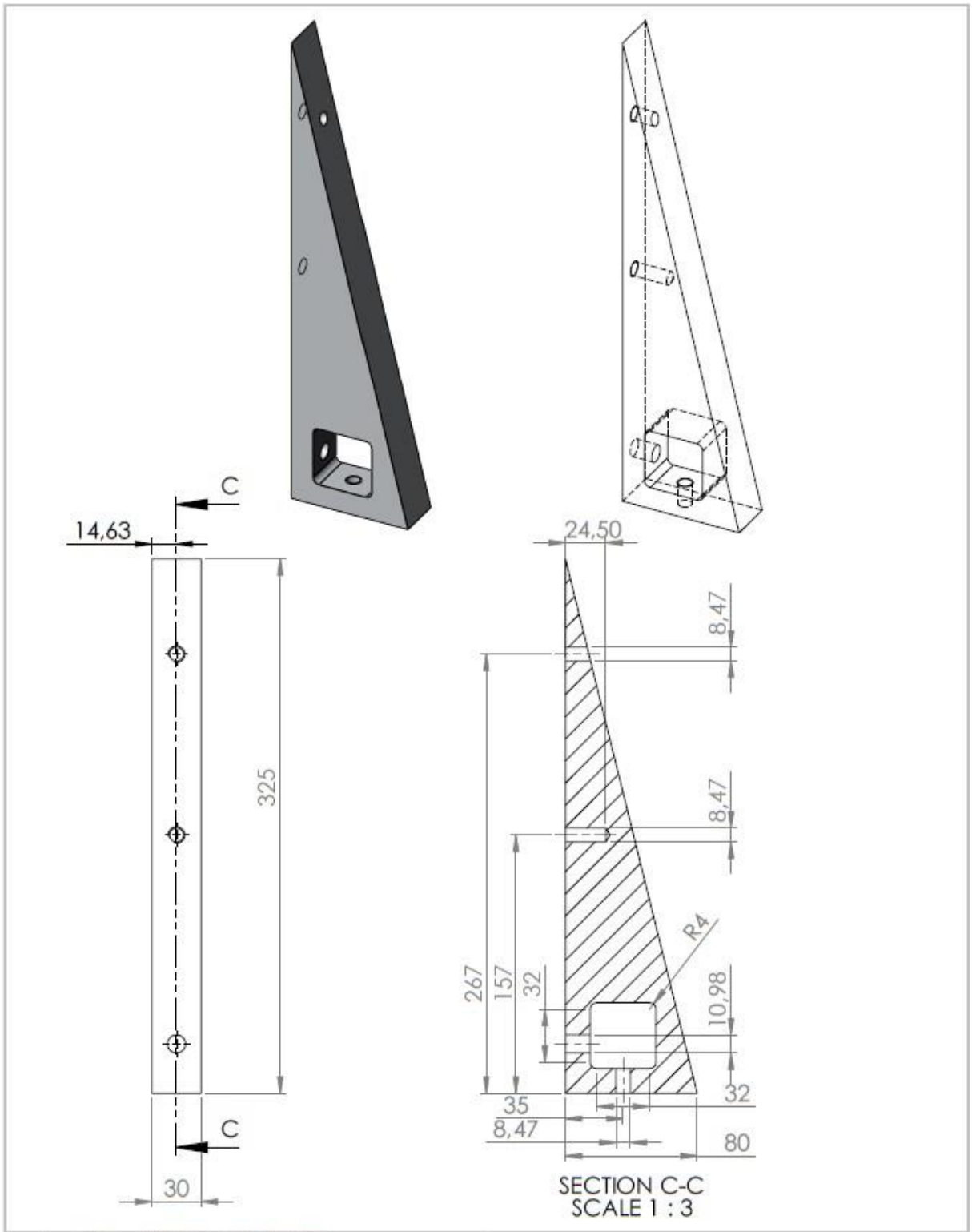

	NAME	SIGNATURE	DATE
DRAWN	SAMUEL		03.04.15
CHK'D			
APPV'D			
MFG			
Q.A			

THE INFORMATION CONTAINED IN THIS DRAWING IS THE SOLE PROPERTY OF LBNI. ANY REPRODUCTION IN PART OR AS A WHOLE WITHOUT THE WRITTEN PERMISSION OF LBNI IS PROHIBITED.

MATERIAL: ALUMINUN 6082-T6

DIMENSIONS ARE IN MILLIMETERS
TOLERANCES: ISO 27684
FINISH: NONE
DEBUR AND BREAK SHARP EDGES

DO NOTSCALE DRAWING

EPFL STI-IBI-LBNI

TITLE: **LEFT BRACE BACK**

A4

SCALE: 1:3

SHEET 1 OF 1

Appendix C

Ag/AgCl Electrodes Manufacturing

Material:

-Silver wire (0.25mm)

-Copper wire(1mm)

-KCl 0.1M

Procedure:

- Clean the silver wire with a fine grade emery paper and rinse it with distilled water.

-Immerge the Silver wire (as an Anode) and the Copper wire (as a Cathode) into 0.1 M KCl. Apply 10 mA/cm^2 during one hour.

-After the electrolysis, rinse the electrode with pure water and store in KCl.

Appendix D

Pipettes

Product information:

- Quartz glass capilaries, 70 mm lenght, 0.5 mm outer diameter, 0.3 mm inner diameter, Product 1401693, Hilgenberg.
- Borosilicate glass with filament, 100mm lenght, 1mm outer diameter, 0.5 mm inner diameter, Product BF100-50-10, Sutter Instrument.
- Borosilicate glass with filament, 80mm lenght, 1mm outer diameter, 0.58 mm inner diameter, Product GB100F-8P, Science Products.

Appendix E

Microscope Software (Developed in LabView Realtime)

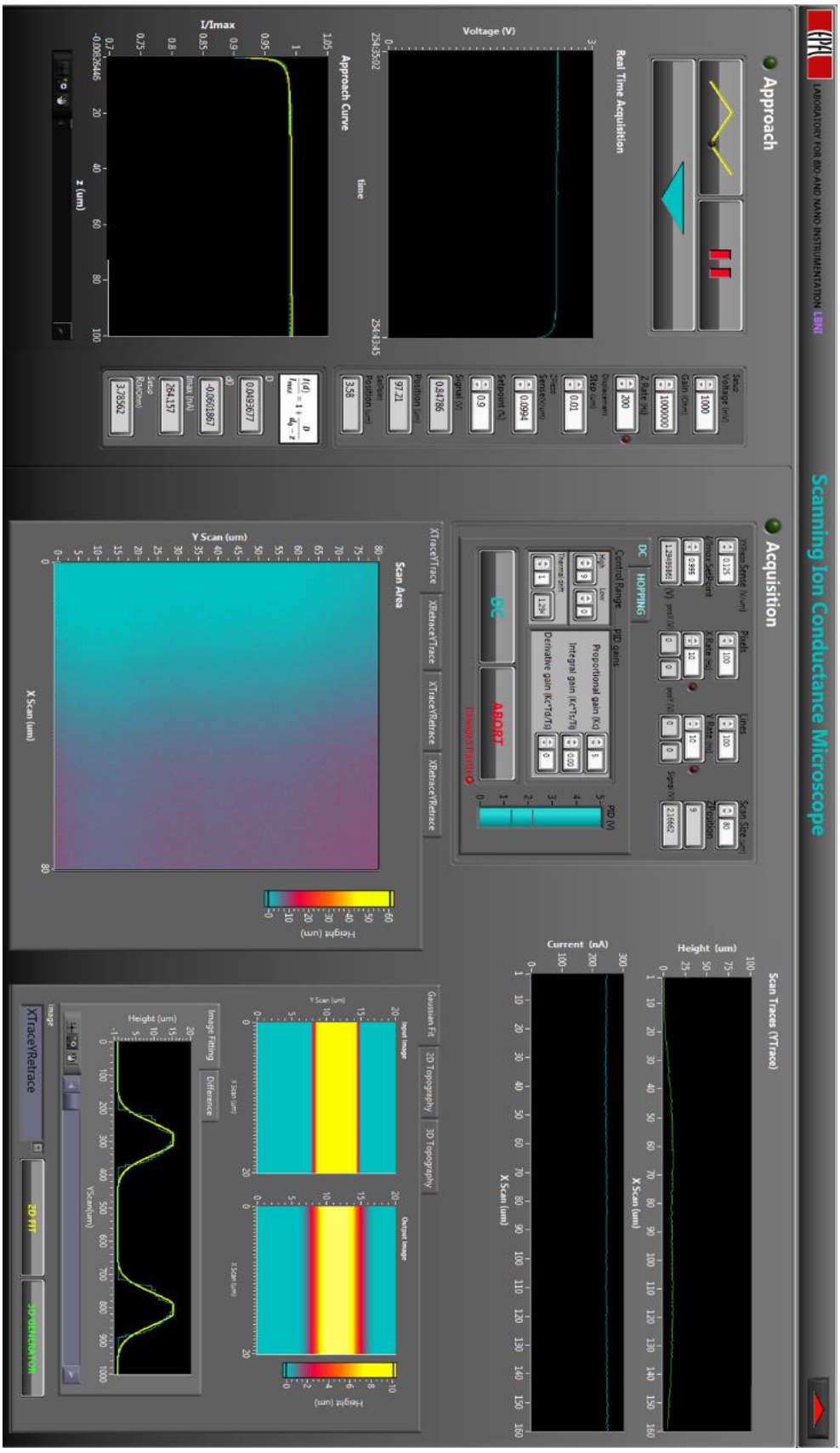

Appendix F

Labview Realtime code

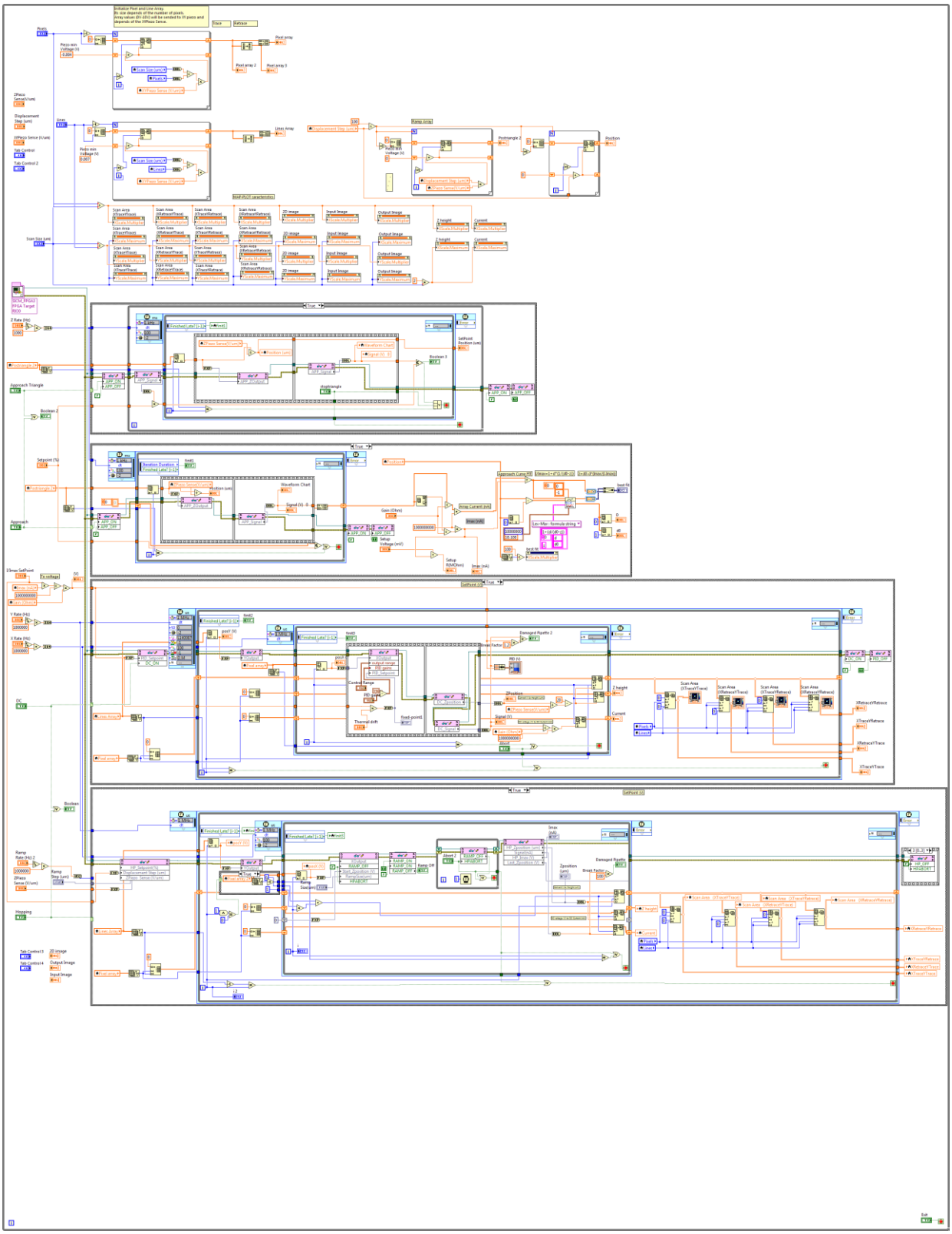

Appendix G

Approach to the surface block diagram

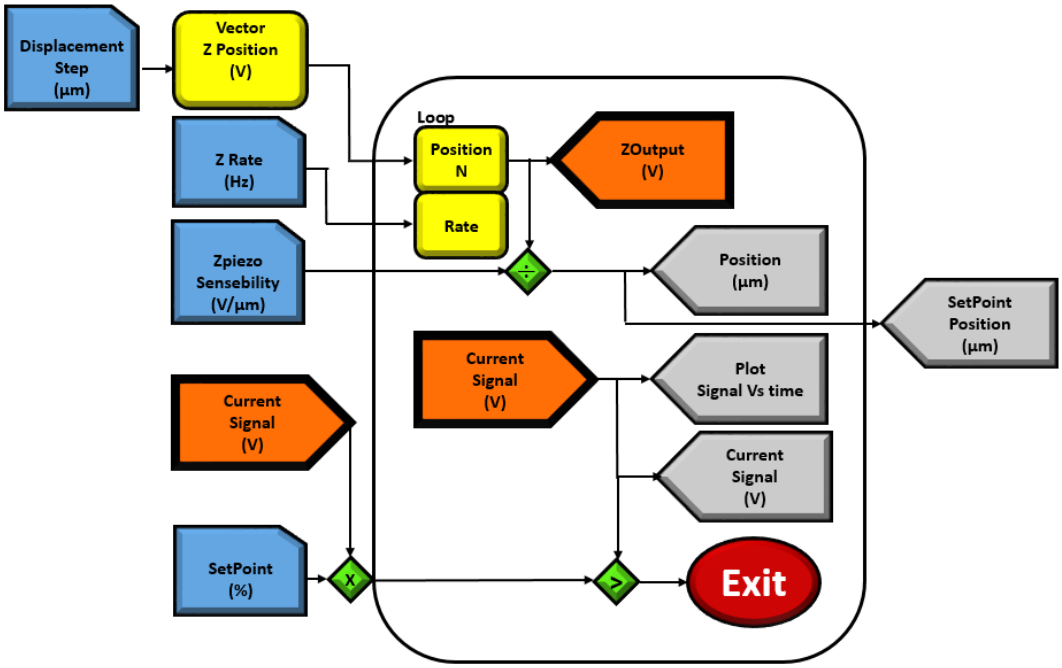

Blue: User variables on screen.

Yellow: Internal ariables .

Orange: Running in FPGA.

Green lozenge: Arithmetic operators .

Green square: Internal constants.

Red: Loop termination conditions.

Appendix H

Approach curve characterization block diagram

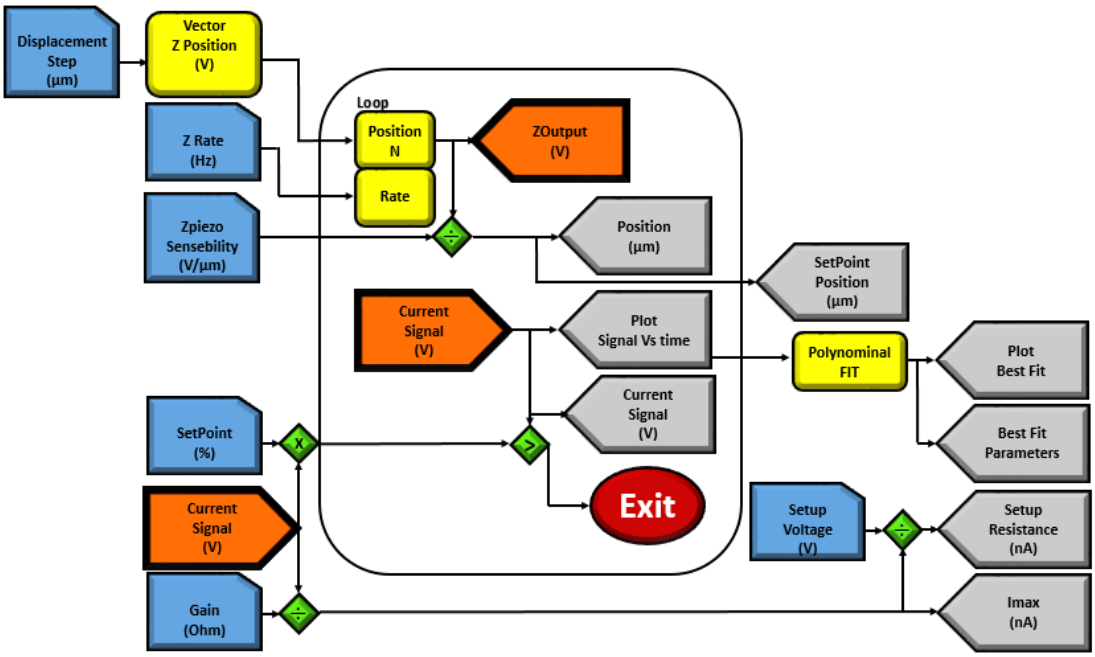

Blue: User variables on screen.

Yellow: Internal ariables .

Orange: Running in FPGA.

Green lozenge: Arithmetic operators .

Green square: Internal constants.

Red: Loop termination conditions.

Appendix I

DC mode block diagram

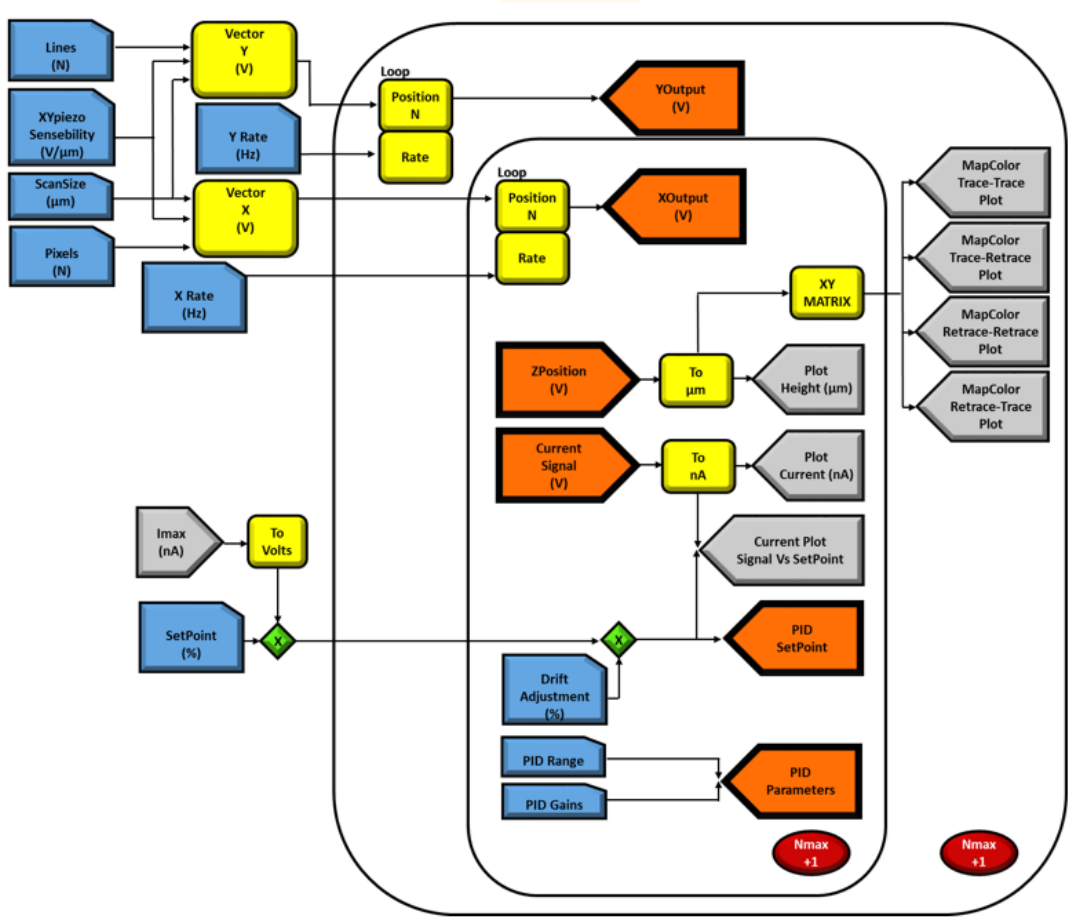

Blue: User variables on screen.

Yellow: Internal ariables .

Orange: Running in FPGA.

Green lozenge: Arithmetic operators .

Green square: Internal constants.

Red: Loop termination conditions.

Appendix J

Hopping mode block diagram

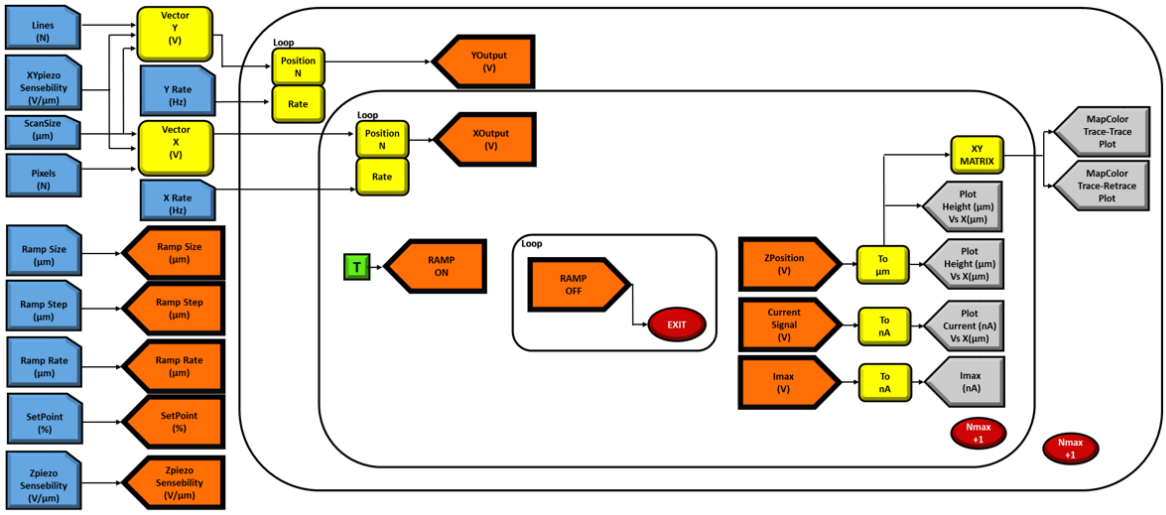

Blue: User variables on screen.

Yellow: Internal ariables .

Orange: Running in FPGA.

Green lozenge: Arithmetic operators .

Green square: Internal constants.

Red: Loop termination conditions.

Appendix L

Data fit block diagram

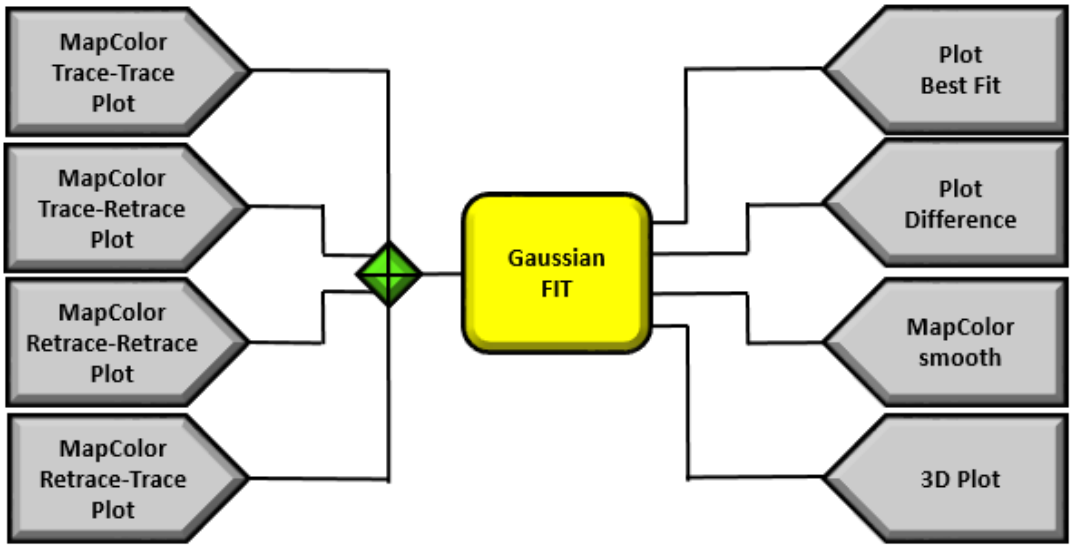

Blue: User variables on screen.

Yellow: Internal ariables .

Orange: Running in FPGA.

Green lozenge: Arithmetic operators .

Green square: Internal constants.

Red: Loop termination conditions.

Appendix M

FPGA Software (Developed in LabView FPGA)

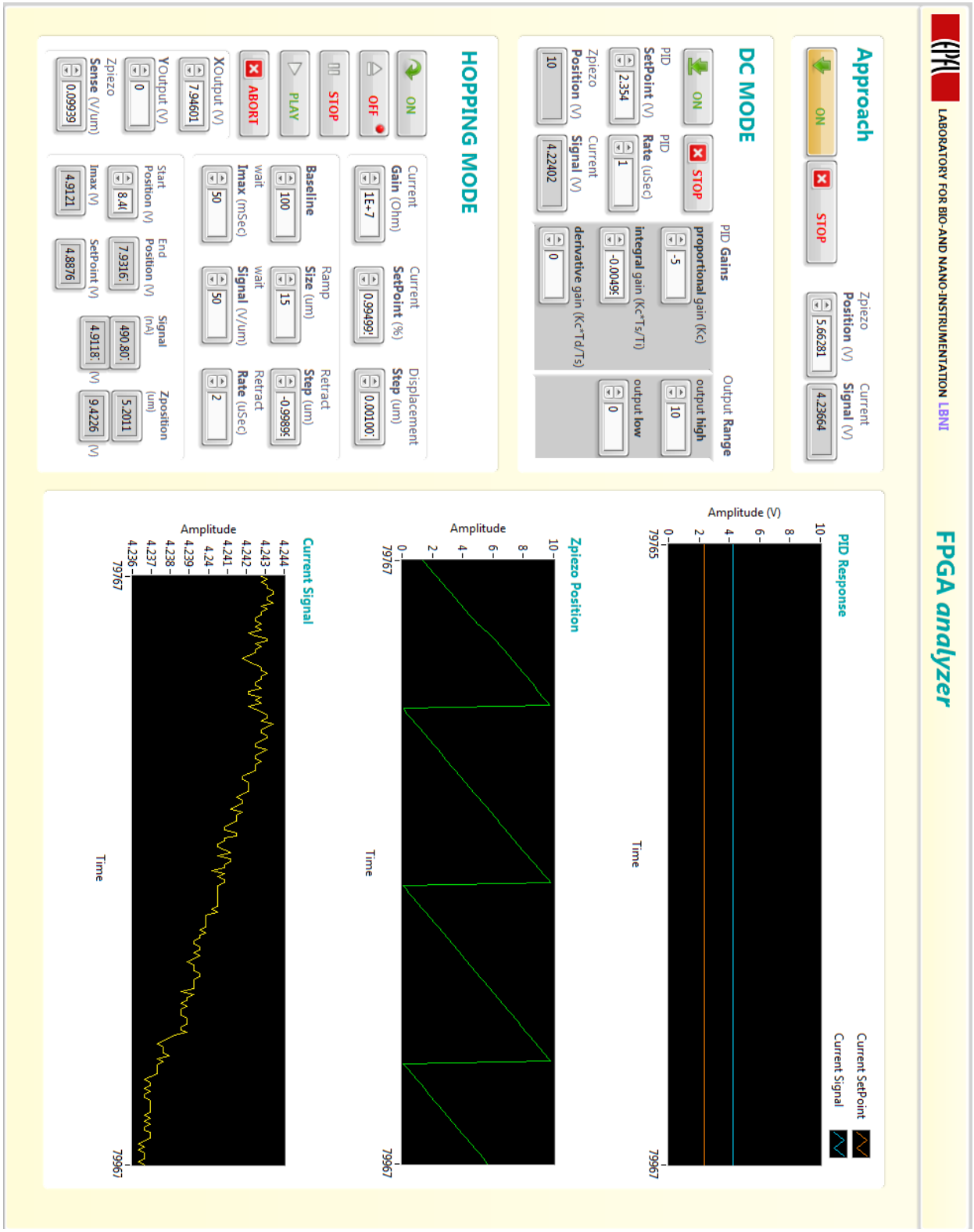

Appendix N

LabView FPGA code

Bibliography

[1] F. M Harold, Ion currents and physiological functions in microorganisms (1977). Ann. Rev. Microbiol, 181-203.

[2] O. P. Hamill, A. Marty, E. Neher, B. Sakmann, F. J. Sigworth (1981). Improved patch-clamp techniques for high-resolution current recording from cells and cell-free membrane patches, Excitable Tissues And Central Nervous Physiology, August, Volume 391, 85-100.

[3] PK Hansma, B Drake, O Marti, SA Gould, CB Prater (1989). The scanning ion-conductance microscope, Science, 3 February, Vol. 243 no. 4891, 641-643.

[4] Korchev YE, Bashford CL, Milovanovic M, Vodyanoy I, and Lab MJ (1997). Scanning Ion Conductance Microscopy of Living Cells, Biophysical Journal, 653-658.

[5] Rebecca Howland, Lisa Benatar (2000). A Pratical Guide to Scanning Probe, ThermoMicroscopes.

[6] W. J. Kaiser and L. D. Bell (1988). Direct investigation of subsurface interface electronic structure by ballistic-electron-emission microscopy, Phys. Rev. Lett. 60, 1406.

[7] Franklin Anariba, Joon Hyung Anh, Goo-Eun Jung, Nam-Joon Cho, and Sang-Joon Cho (2012). Biophysical applications of scanning ion conductance microscopy (SICM), Modern Physics Letters B, 2605.

[8] Happel, P.; Thatenhorst, D.; Dietzel (2012). Scanning Ion Conductance Microscopy for Studying Biological Samples. Sensors, 14983-15008.

[9] A. I. Shevchuk, J. Gorelik, S. E. Harding, M. J. Lab, D. Klenerman and Y. E. Korchev (2001). Simultaneous measurement of Ca2+ and cellular dynamics: combined scanning ion conductance and optical microscopy to study contracting cardiac myocytes, Elsevier, Biophys. J. 81, 1759.

[10] Pastré, D.; Iwamoto, H.; Liu, J.; Szabo, G.; Shao, Z. (2001). Characterization of AC mode scanning ion-conductance microscopy. Ultramicroscopy, 90, 13–19.

[11]S. A. Mann, G. Hoffmann, A. Hengstenberg, W. Schuhmann and I. D. Dietzel (2002), Pulse-mode scanning ion conductance microscopy—a method to investigate cultured hippocampal cells, ELSEVIER, J. Neurosci. Methods 116, 113.

[12] Happel, P.; Hoffmann, G.; Mann, S.A.; Dietzel (2003). Monitoring cell movements and volume changes with pulse-mode scanning ion conductance microscopy. J. Microsc. , 212, 144–151.

[13]J. Gorelik, N. N. Ali, S. H. Sheikh Abdul Kadir, M. Lab, P. Stojkovic, L. Armstrong, E. V. Sviderskaya, Y. A. Negulyaev, D. Klenerman, D. C. Bennett, M. Lako, S. E. Harding, M. Stojkovic and Y. E. Korchev (2008), Non-invasive imaging of stem cells by scanning ion conductance microscopy: future perspective, Tissue Eng: Part C Methods 14, 311.

[14] M. Miragoli, A. Moshkov, P. Novak, A. Shevchuk, V. O. Nikolaev, I. El-Hamamsy, C. M. Potter, P. Wright, S. H. Kadir, A. R. Lyon, J. A. Mitchell, A. H. Chester, D. Klenerman, M. J. Lab, Y. E. Korchev, S. E. Harding and J. Gorelik, (2011). Scanning ion conductance microscopy: a convergent high-resolution technology for multi-parametric analysis of living cardiovascular cells, J. R. Soc. Interface, 8, 913.

[15] P. Happel, G. Hoffmann, S. A. Mann and I. D. Dietzel (2003). Monitoring cell movements and volume changes with pulse-mode scanning ion conductance microscopy, J. Microsc. 212, 144.

[16] D. Sanchez, U. Anand, J. Gorelik, C. D. Benham, C. Bountra, M. Lab, D. Klenerman, R. Birch, P. Anand and Y. Korchev (2007). Localized and non-contact mechanical stimulation of dorsal root ganglion sensory neurons using scanning ion conductance microscopy, J. Neurosci. Methods 159, 26.

[17] A. Bruckbauer, L. Ying, A. M. Rothery, D. Zhou, A. I. Shevchuk, C. Abell, Y. E. Korchev and D. Klenerman (2002). Probing the structure of a water/nitrobenzene interface by scanning ion conductance microscopy, J. Am. Chem. Soc. 124, 8810.

[18] Retrieved from the Ionoscope website, http://www.ionscope.com/.

[19] Novak P, Li C, Shevchuk AI et al. (2009). Nanoscale live-cell imaging using hopping probe ion conductance microscopy.*Nature Methods* vol. 6, (4) 279-281.

[20] Novak P, Gorelik J, Vivekananda U et al. (2013) . Nanoscale-targeted patch-clamp recordings of functional presynaptic ion channels.*Neuron* vol. 79, (6) 1067-1077.

[21] Rheinlaender J, Schäffer TE. 2013. Mapping the mechanical stiffness of live cells with the scanning ion conductance microscope. Soft Matter, (9), 3230-3236.

[22] Bruckbauer, A., James, P., Zhou, D., Yoon, J. W., Excell, D., Korchev, Y. Klenerman, D. (2007). Nanopipette Delivery of Individual Molecules to Cellular Compartments for Single-Molecule Fluorescence Tracking. *Biophysical Journal*,*93*(9), 3120–3131.

[23] Actis, P., Tokar, S., Clausmeyer, J. et al. 2014. Electrochemical nanoprobes for single-cell analysis. ACS Nano 8:875–884.

[24] Comstock et al. 2010. Integrated Ultramicroelectrode—Nanopipet Probe for Concurrent Scanning Electrochemical Microscopy and Scanning Ion Conductance Microscopy. *Anal. Chem.* , 82 (4), 1270–1276.

[26] Ebejer et al. 2010. Localized High Resolution Electrochemistry and Multifunctional Imaging: Scanning Electrochemical Cell Microscopy. *Anal. Chem.*, 2010, *82* (22), 9141–9145.

[27] Chen et al. (2013). Alternating Current Potentiometric Scanning Ion Conductance Microscopy (AC-PSICM), *J. Phys. Chem. C*, 2015, *119* (25), 14392–14399.

[28] Graham N. George, Ingrid J. Pickering, X-RAY Absorption Absorption Spectroscopy in Biology and Chemistry, 2007 Brilliant Light in Life and Material Sciences, Page 97-119.

[29] Stewart C. Bushong (2008). Magnetic Resonance Imaging: Physical and Biological Principles. Mosby.

[30] Sibylle I. Ziegler, Positron Emission Tomography: Principles, Technology, and Recent Developments, ELSEVIER. Nuclear Physics A 752 (2005), 679–687.

[31] Marin van Heel. Principles of Phase Contrast (Electron) Microscopy. Imperial College London, Department of Biological Sciences.

[32] Thomas Veitinger (2012). The Principles of Modulation Contrast. Leica Microsystems.

[33] Ronald J Oldfield (2001). Differential Interference Contrast Light Microscopy. Encyclopedia of Life science.

[34] Nathan S. Claxton, Thomas J. Fellers, and Michael W. Davidson (2006). Laser scanning confocal microscopy. The Florida State University.

[35] Ralph Gräf, Jens Rietdorf, Timo Zimmermann (2005). Adv Biochem Engin/Biotechnol. Springer.

[36] Daniel S. Johnson, Jyoti K. Jaiswal, and Sanford Simon (2012). Total Internal Reflection Fluorescence UNIT 12.29 (TIRF) Microscopy Illuminator for Improved Imaging of Cell Surface Events, Current Protocols in Cytometry. Published online in Wiley Online Library.

[37] Hayk Harutyunyan, Stefano Palomba, Jan Renger, Romain Quidant, and Lukas Novotny, Nonlinear Dark-Field Microscopy, Nano Lett (2010), 10, 5076–5079.

[38] Rainer Heintzmann, Structured Illumination Methods, Handbook of Biological Confocal Microscopy, Third Edition (2006). Springer.

[39] Javad N. Farahani, Matthew J. Schibler and Laurent A. Bentolila,Stimulated (2010). Emission Depletion (STED) Microscopy: from Theory to Practice. Microscopy: Science, Technology, Applications and Education A. Méndez-Vilas and J. Díaz (Eds.) 201.

[40] Hari Shroff, Helen White, and Eric Betzig (2013). Photoactivated Localization Microscopy (PALM) of Adhesion Complexes, Current Protocols in Cell Biology. Published online in Wiley Online Library.

[41] Boyde A. (1985). Biomedical Research Applications of Scanning Electron Microscopy. Journal of Anatomy, 141-244.

[42] Winey M, Meehl JB, O'Toole ET, Giddings TH. (2014). Conventional transmission electron microscopy. Drubin DG, ed. Molecular Biology of the Cell.

[43] Smyth MS, Martin JHJ. (2000). X Ray crystallography. Molecular Pathology, 53(1), 8-14.

[44] Scherzinger AL, Hendee WR. (1985). Basic Principles of Magnetic Resonance Imaging—An Update. Western Journal of Medicine, 143(6), 782-792.

[45] Le Grimellec C, Lesniewska E, Giocondi MC, Finot E, Vié V, Goudonnet JP. Imaging of the surface of living cells by low-force contact-mode atomic force microscopy. Biophysical Journal (1998), 695-703.

[46] Milhiet P-E, Gubellini F, Berquand A, et al. (2006). High-Resolution AFM of Membrane Proteins Directly Incorporated at High Density in Planar Lipid Bilayer. Biophysical Journal, 91(9), 3268-3275. doi:10.1529/biophysj.106.087791.

[47] Hansma HG, Laney DE, Bezanilla M, Sinsheimer RL, Hansma PK. Applications for atomic force microscopy of DNA. Biophysical Journal. 1995, 68(5), 1672-1677.

[48] Neish CS, Martin IL, Henderson RM, Edwardson JM. (2002). Direct visualization of ligand-protein interactions using atomic force microscopy. British Journal of Pharmacology, 135(8), 1943-1950.

[49] Lyubchenko YL, Gall AA, Shlyakhtenko LS. (2014). Visualization of DNA and Protein-DNA Complexes with Atomic Force Microscopy. Methods in molecular biology, 367-384.

[50] Pierre-Henri Puech, Kate Poole, Detlef Knebel, Daniel J. Muller, (2006). A new technical approach to quantify cell–cell adhesion forces by AFM. Ultramicroscopy, Volume 106, Issues 8–9, 637-644.

[51] Park, Paul S.-H. (2015), and Daniel J. Müller. Dynamic single-molecule force spectroscopy of rhodopsin in native membranes. Methods in molecular biology, 173–185.

[52] Schneider SW, Sritharan KC, Geibel JP, Oberleithner H, Jena BP. Surface dynamics in living acinar cells imaged by atomic force microscopy: Identification of plasma membrane structures involved in exocytosis. Proceedings of the National Academy of Sciences of the United States of America. (1997), 316-321.

[53] Di Bucchianico, Sebastiano et al. (2015). Atomic Force Microscope Nanolithography on Chromosomes to Generate Single-Cell Genetic Probes. Journal of Nanobiotechnology, 9, 27.

[54] Suenne Kim, Farbod Shafiei, Daniel Ratchford and Xiaoqin Li (2011). Controlled AFM manipulation of small nanoparticles and assembly of hybrid nanostructures, Nanotechnology, 22(11), 115301.

[55] Retrieved from the Park Systems website, http://www.parkafm.com/.

[56] Korchev, Y.E. et al. (1997), Scanning ion conductance microscopy of living cel. Biophysical Journal , Volume 73 , Issue 2 , 653 – 658.

[57] James E. Hall (1975). Access Resistance of a small circular pore, Journal of general Physiology, 66(4), 531–532.

[58] Sutter Instruments p2000 laser-based micropipette pull system, operational manual.

[59] C. D. Frisbie, L. F. Rozsnyai, A. Noy, M. S. Wrighton and C. M. Lieber, Functional group imaging by chemical force microscopy, Science 265 (1994), 2071.

[60] Chiao-Chen Chen and Lane A. Baker, Effects of pipette modulation and imaging distances on ion currents measured with Scanning Ion Conductance Microscopy (SICM). Analyst (2011), 136, 90-97.